International Journal of

Thermodynamics

International Centre for Applied Thermodynamics

Research Article

The Study of Sound Speed as a Function of Pressure at Different Temperatures in Biofuel Component Liquids

*P. Kuchhal [iD]

Department of Applied Sciences, University of Petroleum and Energy Studies, Dehradun, India
E-mail: pkuchhal@ddn.upes.ac.in

Abstract

In the present study, an approximation is applied to study the sound speed in liquids as a function of pressure at different temperatures. The relation obtained is applied in the case of biofuel component liquids. The calculated results for each liquid were found to be in good agreement with the experimental results throughout the range of pressure and temperature. The maximum percentage error and average percentage error are not more than 5.2 and 1.9, respectively, in the entire range of pressure and temperature for all liquids. Furthermore, the internal pressure and nonlinear Bayer's parameters are also computed as a function of temperature at one atmosphere from sound speed for the first time in biofuel component liquids.

Keywords: Sound speed; pressure; temperature; biofuel component liquids; internal pressure; nonlinear Bayer's parameter.

1. Introduction

The exhaustive use of fossil fuels to sustain and develop the economy not only puts pressure on fossil fuel reservoirs but also abuses our environment due to the ejection of greenhouse gases (CO_2, NO_x, etc.). As a result, a large community of scientists and engineers are engaging themselves and coming up with alternatives to fossil fuels to reduce their dependency and minimize greenhouse gas emissions [1] – [2]. Different sources of renewable energy have been presented so far, such as biofuel, wind energy, solar photovoltaic solar thermal, and geothermal energy. Biofuels have attracted attention as an alternative, at least in the transport sector [3]. Transesterification reactions occur when biofuels are derived from vegetable oils or animal fats, where fats/oils are blended with alcohol (methanol or ethanol) to form fatty acid alkyl esters. Broadly, alcohol alongside biodiesel is the most suitable type of biofuel [4]. However, conventional diesel fuel can be blended in optimized proportions with biodiesel to decrease toxic gas emissions in existing diesel engines or be used without any adulteration as renewable energy for diesel engines. However, the major challenge with biofuels is that they are derived from various sources, and consequently, fatty acids have different chain lengths and may differ in the degree of undersaturation. The chain lengths of fatty acids derived from different sources (palm, soybean, rapeseed, and sunflower) have a chain of 16 and 18 carbons, whereas chains of 20 and 22 carbon atoms may not be ruled out (rape species and animal fats). However, a chain of 10 to 14 carbons was also observed, particularly in the fatty acids derived from palm kernel and coconut oils [5] – [7]. The varying nature of chain length and degree of unsaturation affect the thermo-physical properties of biofuels obtained from different sources and, consequently, influence the engine's overall performance. In addition, optimization of the fraction of biodiesel and diesel fusion requires accurate familiarity of thermal-physical physiognomies in biodiesel based on pressure and temperature. The density, bulk modulus, thermal expansion coefficient, internal pressure, and nonlinear Bayer's parameters play an essential role in designing the engine and injection process [8] – [10].

The thermo-physical properties of biofuels can be estimated from the properties of biofuel components using mixing rules if these properties of the components are available. The study of thermos-physical properties as function pressure and temperature of liquids from sound speed measurement is comparatively more accurate as the measurement of sound speed as a function of pressure and temperature is more precise than the equation of state.

Therefore, this study aims to develop a model that can describe the sound speed as a function of pressure at different temperatures from which other thermophysical properties can be derived. To the best of our knowledge, the internal pressure [11] – [14] and nonlinear Bayer's parameter, which are strongly correlated with the structural properties of biofuels, are rarely studied in the case of biofuels. Generally, the value of (B/A) lies in the range of 5–13. A lower value was observed in water, while the highest value was observed for fluorocarbons [13] – [15]. Therefore, both parameters are also computed as function temperatures in biofuel component liquids, where the experimental data are available in a wide range of pressures and temperatures. Methyl caprate, ethyl caprate, methyl oleate, methyl linoleate, methyl myristate, ethyl myristate, and methyl palmitate were considered for this study. The experimental data for these liquids were obtained from [4], [7], [16].

2. Methodology

The investigation of the sound speed $u(p, T_R)$ as a function of pressure (p) at the reference temperature (T_R) in the biofuel component liquids, the ratio of the second pressure derivative of sound speed to the first pressure derivative of sound speed, is independent of pressure is used and given by Eq. (1)

$$\frac{\left(\partial^2 u / \partial p^2\right)_{T_R}}{\left(\partial u / \partial p\right)_{T_R}} = -z \tag{1}$$

This approximation was successfully applied to describe the sound speed as a function of pressure and temperature in liquid metals [17]. Moreover, this approximation also explains the anomalous behavior of sound speed in water [18]. Integrating the Eq. (1) successively in the pressure limit of p_0 to p yields the following equations [17]:

$$u'(p, T_R) = u'(p_0, T_R)\exp(-z(p - p_0)) \tag{2}$$

$$u(p, T_R) = u(p_0, T_R) + \left(u'(p_0, T_R)/z\right)[1 - \exp(-z(p - p_0))] \tag{3}$$

where, $u'(p_0, T_r)$ is the first pressure derivative of sound speed, $u(p, T_r)$ at pressure, p_0 and temperature, T_R.

Eq. (3) reveals that the sound speed increases as a function of pressure and converges to $u(p_0, T_R) + \left(u'(p_0, T_R)/z\right)$ as the pressure approaches infinity.

The following relation between $u'(p_0, T)$ and $u(p_0, T)$ is proposed to include the temperature effect.

$$u'(p_0, T) = a \exp\{-bu(p_0, T)\} \tag{4}$$

The pressure in the liquids is the sum of the external and internal pressures [13]. Since Eq. (4) is applied at a constant external pressure, and it may be written as

$$\left(\frac{du(p,T)}{dp_i}\right)_{p_0} = a \exp\{-bu(p_0, T)\} \tag{5}$$

The integration of Eq. (5) under the limit of temperature T_r to T gives

$$p_i(T) - p_i(T_R) = \frac{1}{ab}\left[e^{bu(p_0, T_R)} - e^{bu(p_0, T)}\right] \tag{6}$$

Eq. (6) suggests that

$$p_i(T) = \frac{e^{bu(p_0, T)}}{ab} \tag{7}$$

The thermal pressure coefficient, ξ given by Eq. (8) is computed by linear fitting between p_i and T, which is used to introduce the temperature effect into Eq. (3).

$$p_i = \xi T + C \tag{8}$$

To study the sound speed as a function of pressure at different temperatures, Eq. (2) and Eq. (3) can be written as [15]:

$$u'(p, T) = u'(p_0, T_R)ex p[-z(p - p_0) + \xi(T - T_R)] \tag{9}$$

$$u(p, T) = u(p_0, T_R) + \left(u'(p_0, T_R)/z\right)[1 - \exp\{-z(p - p_0) + \xi(T - T_R)\}] \tag{10}$$

The sound speed as a function of pressure at different temperatures can be computed using Eq. (10) indicates that $u(p_0, T_r)$, $u'(p_0, T_r)$, z, and ξ are known as the liquids of interest.

Moreover, the internal pressure as a function of temperature at atmospheric pressure can also be computed from its thermodynamic definition [11], as given by Eq. (11)

$$p_i(T) = \frac{\alpha}{k_T}T \tag{11}$$

where α and k_T are the isobaric thermal expansion coefficient and isothermal compressibility, respectively.

This study is further extended to determine nonlinear Bayer parameters as a function of pressure and temperature. The nonlinear Bayer parameter is well understood to understand the molecular dynamics of the liquid along with the distortion of a finite amplitude of the wave due to nonlinearity associated with the medium. Moreover, the estimation of the Bayer parameter may be considered as a corresponding parameter to understand biofuels.

The Bayer Parameter can be expressed as [15]

$$\frac{B}{A} = 2\rho u\left(\frac{\partial u}{\partial p}\right)_s$$
$$= 2\rho u\left(\frac{\partial u}{\partial p}\right)_T + \frac{2uT\alpha}{C_p}\left(\frac{\partial u}{\partial p}\right)_p \tag{12}$$
$$\frac{B}{A} = \left(\frac{B}{A}\right)' + \left(\frac{B}{A}\right)''$$

The first pressure derivative of the sound speed as a function of the pressure and temperature is given by Eq. (9), while the first temperature derivative of the sound speed as a function of pressure and temperature can be determined by differentiating Eq. (10) for temperature and is given by Eq. (13).

$$\left(\partial u(P, T)/\partial T\right)_p = \xi u'(p_0, T_R) \exp[-z(p - p_0) + +\xi(T - T_R)] \tag{13}$$

3. Results

The proposed Eq. (3) was used to study the sound speed as a function of pressure at different temperatures for all liquids. As a first step, the adjustable parameters $u(p_0, T_R)$, $u'(p_0, T_R)$ and z in Eq. (3) were determined using a nonlinear fitting toolbox in MATLAB. The values of these parameters are reported in Table-1, along with R^2 for all liquids. The value of R^2 indicate the applicability of Eq. (3) to describe the sound speed as a function of the pressure and temperature for all liquids of concerned.

In the second step, nonlinear fitting is used to determine the values of constants a and b in Eq. (4) at ambient pressure, p_0. The values of $u'(p_0, T)$ and $u(p_0, T)$ are listed in Table-1. The values of a and b obtained are reported in Table-2, along with R^2.

The values of R^2 give us the confidence to use it to calculate the internal pressure. However, fitting in all Biofuel components is relatively poor, particularly in ethyl myristate, but Eq. (7), we can calculate the internal pressure directly from the sound speed. The internal pressure calculated from Eq. (7) are plotted in Figure 1 at different temperatures for all Biofuel components.

In the third step, the value of the thermal pressure coefficient ξ in Eq. (8) is computed by a linear fitting between the internal pressure and temperature. Figure1 shows that there is an almost linear relationship between the internal pressure and temperature. The values of the adjustable parameters ξ and C are reported in Table-2 along with the values of R^2. It should be noted that the second-order polynomial gives a better fit between the internal pressure and temperature.

Table 1. The fitting parameters of Eq. (3) along with R^2 at different temperatures in all biofuel component liquids of study.

Liquid	T(K)	$u(p_0, T_R)$ (m s^{-1}))	$u'(p_0, T_R)$ (m s^{-1} MPa^{-1})	Z(x10^{-3}) (MPa^{-1})	R^2	Pressure Range (MPa)	Reference
Methyl Caprate	283.15	1365	4.505	4.472	0.9999	0.1013-140	[7]
	303.15	1295	4.678	4.109	0.9998	0.1013-210	
	323.15	1222	4.980	4.396	0.9997		
	343.15	1152	5.330	4.723	0.9996		
	363.15	1093	5.462	4.711	0.9997		
	383.15	1030	5.826	5.029	0.9997		
	403.15	969	6.128	5.258	0.9996		
Ethyl Caprate	283.15	1357	4.403	3.769	0.9999	0.1013-210	
	303.15	1281	4.731	4.184	0.9998		
	323.15	1212	4.989	4.278	0.9997		
	343.15	1142	5.374	4.707	0.9996		
	363.15	1077	5.722	5.057	0.9995		
	383.15	1044	6.060	5.358	0.9994		
	403.15	953.45	6.447	5.737	0.9991		
Methyl Oleate	283.15	1447	4.089	3.478	0.9999	0.1013-200	[16]
	303.15	1375	4.406	3.869	0.9999		
	323.15	1307	4.684	4.135	0.9998		
	343.15	1242	4.951	4.372	0.9998		
	363.15	1178	5.270	4.716	0.9998		
	383.15	1119	4.473	4.784	0.9996		
	393.15	1090	5.623	4.936	0.9996		
Methyl Linoleate	283.15	1457	4.214	3.988	0.9999	0.1013-150	
	303.15	1388	4.323	3.701	0.9998	0.1013-210	
	323.15	1318	4.619	4.033	0.9998		
	343.15	1252	4.891	4.278	0.9997		
	363.15	1188	5.185	4.566	0.9997		
	383.15	1127	5.441	4.760	0.9997		
	393.15	1098	5.564	4.841	0.9997		
Ethyl Myristate	293.15	1360	5.034	7.805	1	0.1 – 50	[4]
	303.15	1322	5.072	6.191	1	0.1-100	
	323.15	1253	5.264	5.659	1		
	343.15	1186	5.658	6.193	0.9999		
	363.15	1123	6.010	6.565	0.9999		
	383.15	1059	6.495	7.339	0.9999		
	403.15	999.7	6.901	7.718	0.9998		
Methyl Myristate	303.15	1336	4.793	5.5556	1	0.1 – 70	
	323.15	1265	5.280	5.9440	1	0.1 – 80	
	343.15	1196	5.674	6.4670	1		
	363.15	1132	6.0660	7.1190	1		
	383.15	1068	6.559	7.8690	1		
	403.15	1038	6.767	8.141	0.9999		
Methyl Palmitate	313.15	1317	5.041	6.357	1	0.1 – 40	
	323.15	1284	5.202	6.201	1	0.1-50	
	343.15	1216	5.661	7.604	1		
	363.15	1151	6.022	7.768	0.9999		
	383.15	1088	6.400	6.942	0.9999		
	403.15	1057	6.608	7.390	0.9999		

Table 2. Fitted parameters of Eq. (4) and Eq. (8) along with values of R^2.

| Liquid	Equation (4) coefficients				Equation (8) coefficients		
	T_R	A	b (x 10^{-04})	R^2	ξ	C	R^2
Methyl Caprate	283.15	13.14	7.916	0.9944	-0.6325	459.3	0.9931
Ethyl Caprate	283.15	16.39	9.722	0.9934	-0.6134	404.4	0.9867
Methyl Oleate	283.15	14.66	8.762	0.9972	-0.6681	462.6	0.9939
Methyl Linoleate	283.15	13.68	8.196	0.9941	-0.6791	484.1	0.9951
Ethyl Myristate	293.15	17.32	9.317	0.9812	-0.5695	384.6	0.9941
Methyl Myristate	303.15	22.03	1.136	0.9985	-0.5782	355.7	0.9947
Methyl Palmitate	313.15	19.85	1.039	0.9981	-0.5640	366.2	0.9975
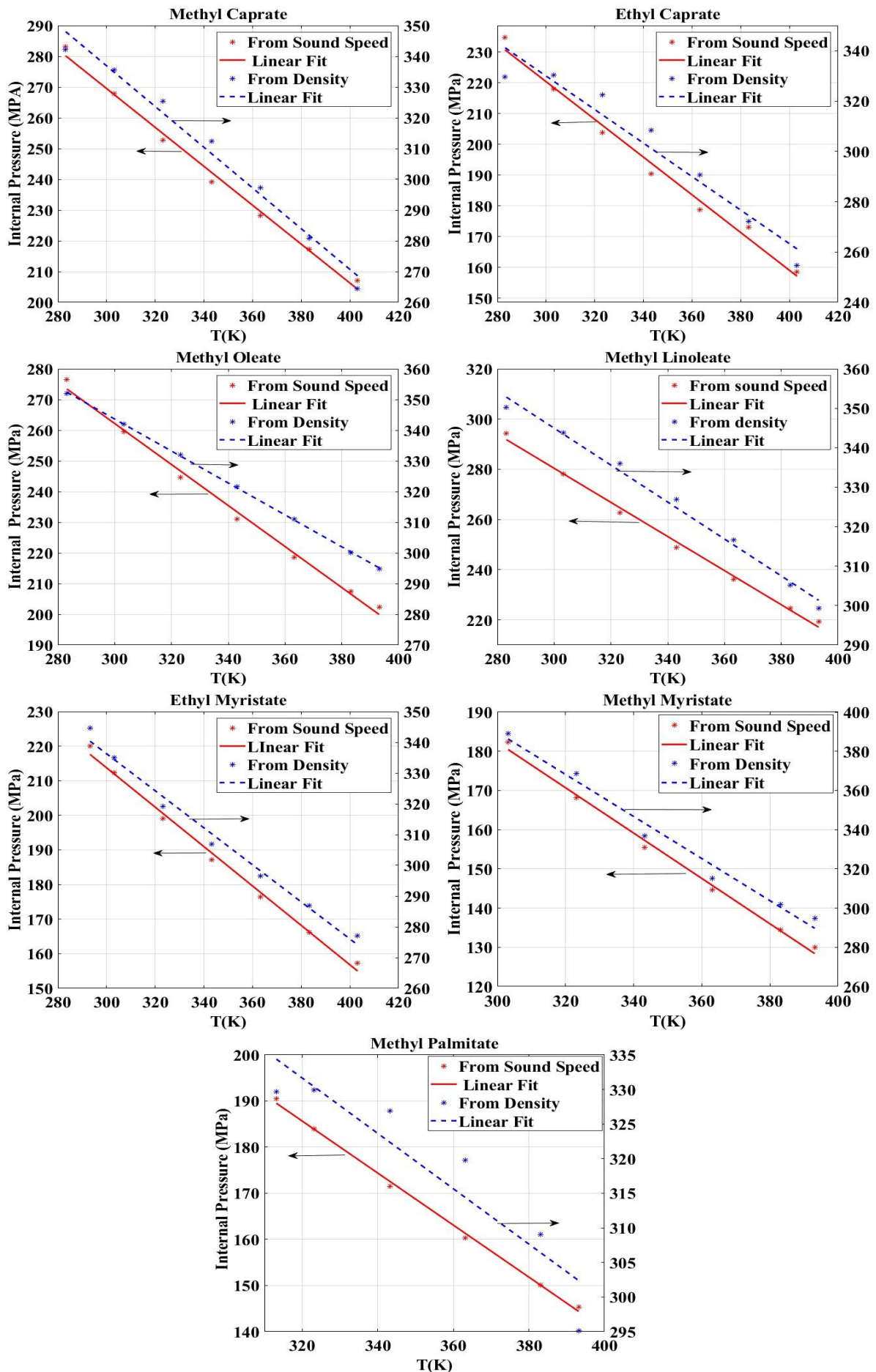
Figure 1. The variation of internal pressure as a function of temperature at atmospheric pressure as calculated from Eq, (7) and Eq. (11) for all biofuel component liquids of interest.

In the final step, Eq. (10) was applied successfully in all liquids to study the sound speed as a function of pressure at different temperatures. Moreover, the internal pressure is also calculated by calculating the thermal pressure coefficient, $\xi = \frac{\partial p_{th}}{\partial T} = \frac{\alpha}{k_T}$, from the density data given in reference papers and compared with the internal pressure calculated from the sound speed in Figure 1. Moreover, Eq. (12) is used to compute the nonlinear Bayer's parameter [20] as a function of temperature for all biofuel components. The computed values of the nonlinear Bayer's parameters are listed in Table-3. The variations in density ρ, α and C_p as a function of pressure-temperature were taken from the source papers [4], [7], [16].

4. Discussion

The computed speed as a function of pressure at different temperatures was compared with the experimental data for all liquids, and the maximum percentage error (MPE) is plotted in Figure 2.

Figure 2 shows that the MPE is not more than 5.2, over the entire range of pressure and temperature for all biofuel components of the study.

This error may be due to multiple reasons, such as the slight deviation of Eq. (8) from the linear fit as depicted in R^2 value in Table-2 or experimental error at high pressure and high-temperature regions or the approximation given by Eq. (1) may become temperature-dependent at high temperatures. However, the second-order polynomial fits the internal pressure vs. temperature curve more accurately, and the values of R^2 were found to be very close to unity in all cases. The thermal effect through a second-order polynomial is also included in Eq. (3) by adding $p_{th} = (T - T_A)[a(T + T_A)+b]$ in the pressure term. In that case, the MPE is not more than 4.9, in the entire pressure and temperature range. Moreover, the average errors in both approaches were found to be 1.9% and 1.0%, respectively. Because the error obtained from second-order polynomial fitting is not far better than linear fitting, a linear approximation was used for this study.

The internal pressure is also computed as a function of the temperature for each liquid from Eq. (7) and plotted in Figure 1, and the internal pressure computed from Eq. (11).

The ratio of the isobaric thermal expansion coefficient and isothermal compressibility required in Eq. (11) are computed from the density measurements [4,7,16]. Figure 1 shows that the internal pressure decreases as the temperature increases and possesses a negative thermal pressure coefficient, which is consistent with the results reported for ethyl caprate [12] and methyl linoleate [18]. To the best of our knowledge, the study of internal pressure as a function of temperature in biofuels has hardly been investigated. However, the internal pressure, computed from Eq. (7) is smaller than that computed using Eq. (11), but the values of ξ are found to close from both equations, except in methyl myristate, where the difference is quite significant. However, the difference between the internal pressures calculated from Eq. (7) and Eq. (11) does not introduce much error on the inclusion of the temperature effect in Eq. (3) as the internal pressure from Eq. (7), is negatively biased.

At atmospheric pressure, internal pressure varies from 0.2 to 0.8 GPa for non-associated and associated liquids over the temperature range below their boiling points [14]. Based on the discussion given in [14], liquids are characterized into two classes based on the temperature dependence of the internal pressure. Liquids with a positive thermal pressure coefficient include n-alkanes, carbon tetrachloride, and benzene with comparatively weak intermolecular interactions. On the other hand, liquids with a negative coefficient of thermal expansion coefficient include the spatial networks of H-bonds such as water, ethylene glycol, 1,2-, and 1,3-propanediol. In the present study, the observed internal pressure was near the lower limit for the non-associated liquids.

Moreover, to the best of our knowledge, the calculations of nonlinear Bayer's parameters as a function of temperature for all biofuel component liquids. Table-3 shows the fragile dependence of $\left(\frac{B}{A}\right)$ on temperature. However, the values of $\left(\frac{B}{A}\right)''$ is negative but small compared to the $\left(\frac{B}{A}\right)'$ increase with an increase in temperature for all liquids of concern. The $\left(\frac{B}{A}\right)$ values obtained here are consistent with the results reported for various classes of molecular green liquids at room temperature and atmospheric pressure [19].

Table 3. Variation of Bayer's parameters as a function temperature in biofuel component liquids of study.

Liquids		283.15K	303.15K	323.15K	343.15K	363.15K	383.15K	403.15K
Methyl Carpet	$(B/A)'$	10.82	10.76	10.64	10.46	10.20	9.87	9.46
	$(B/A)''$	-1.01	-1.11	-1.20	-1.29	-1.36	-1.41	-1.44
	B/A	9.81	9.65	9.44	9.17	8.85	8.46	8.01
Ethyl Carpet	$(B/A)'$	10.41	10.27	10.09	9.85	9.56	9.22	8.83
	$(B/A)''$	-1.04	-1.18	-1.30	-1.39	-1.46	-1.50	-1.51
	B/A	9.37	9.10	8.79	8.46	8.10	7.72	7.32
Methyl Oleate	$(B/A)'$	10.42	10.33	10.19	10.01	9.78	9.50	9.34
	$(B/A)''$	-0.93	-0.99	-1.05	-1.11	-1.17	-1.22	-1.25
	B/A	9.49	9.34	9.14	8.90	8.62	8.28	8.09
Methyl Linoleate	$(B/A)'$	10.63	10.44	10.22	9.99	9.76	9.53	9.41
	$(B/A)''$	-1.01	-1.08	-1.15	-1.22	-1.30	-1.37	-1.41
	B/A	9.62	9.36	9.07	8.77	8.47	8.16	8.00
Ethyl Myristate	$(B/A)'$	11.61	11.95	12.23	12.42	12.49	12.41	12.15
	$(B/A)''$	-0.65	-0.70	-0.77	-0.85	-0.93	-1.03	-1.12
	B/A	10.97	11.25	11.46	11.57	11.55	11.38	11.03
Methyl Myristate	$(B/A)'$	10.97	11.01	11.02	10.99	10.89	10.70	10.40
	$(B/A)''$	-1.13	-1.09	-1.09	-1.12	-1.20	-1.33	-1.48
	B/A	9.83	9.92	9.94	9.86	9.68	9.37	8.92
Methyl Palmitate	$(B/A)'$	11.02	11.21	11.34	11.40	11.38	11.27	11.05
	$(B/A)''$	-0.70	-0.8057	-0.9052	-0.9981	-1.081	-1.1503	-1.2019
	B/A	10.32	10.4044	10.4363	10.4047	10.3019	10.1189	9.84501
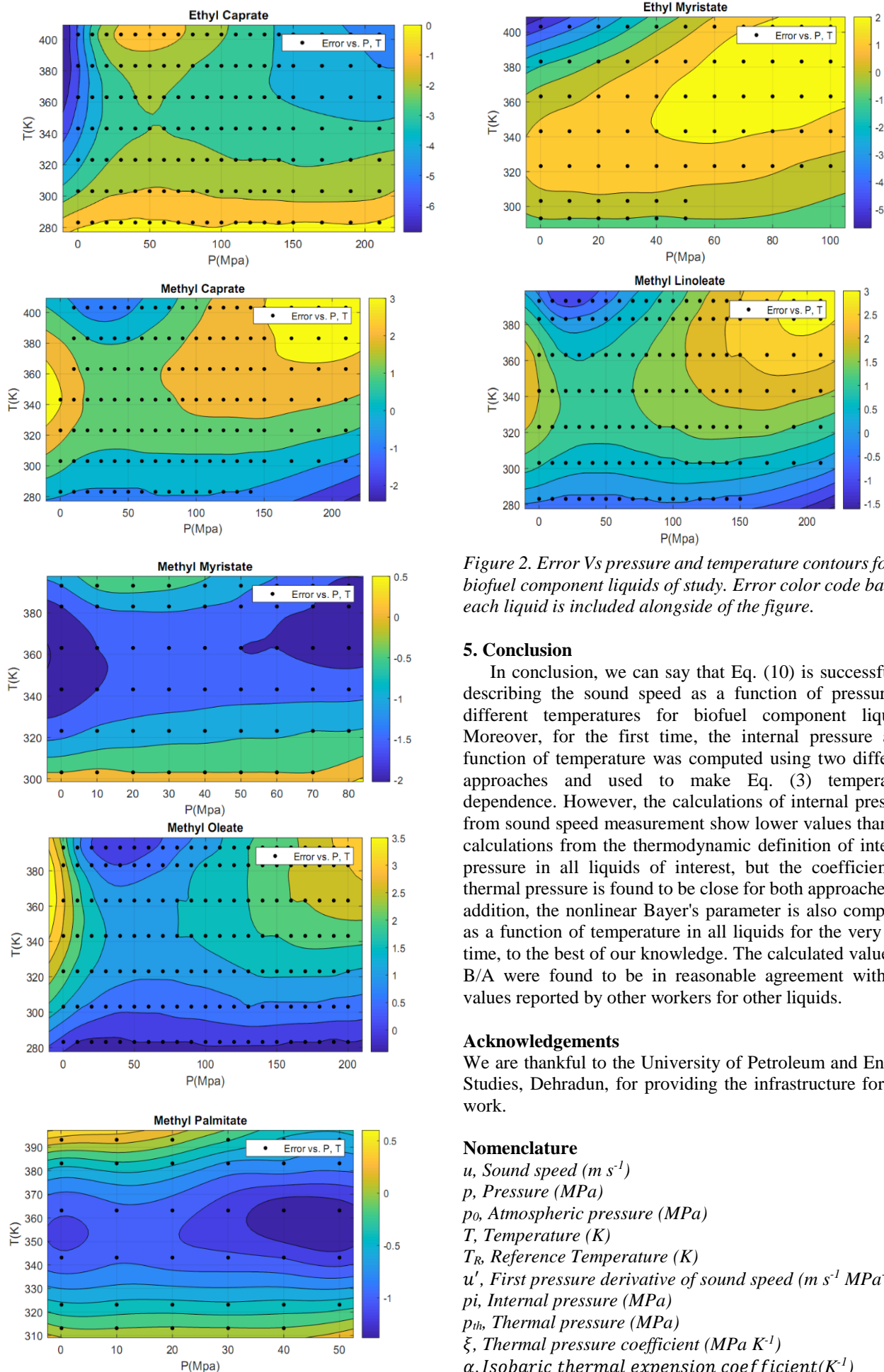
Figure 2. Error Vs pressure and temperature contours for all biofuel component liquids of study. Error color code bar for each liquid is included alongside of the figure.

5. Conclusion

In conclusion, we can say that Eq. (10) is successful in describing the sound speed as a function of pressure at different temperatures for biofuel component liquids. Moreover, for the first time, the internal pressure as a function of temperature was computed using two different approaches and used to make Eq. (3) temperature dependence. However, the calculations of internal pressure from sound speed measurement show lower values than the calculations from the thermodynamic definition of internal pressure in all liquids of interest, but the coefficient of thermal pressure is found to be close for both approaches. In addition, the nonlinear Bayer's parameter is also computed as a function of temperature in all liquids for the very first time, to the best of our knowledge. The calculated values of B/A were found to be in reasonable agreement with the values reported by other workers for other liquids.

Acknowledgements

Nomenclature

u, Sound speed (m s^{-1})
p, Pressure (MPa)
p_0, Atmospheric pressure (MPa)
T, Temperature (K)
T_R, Reference Temperature (K)
u', First pressure derivative of sound speed (m s^{-1} MPa^{-1})
pi, Internal pressure (MPa)
p_{th}, Thermal pressure (MPa)
ξ, Thermal pressure coefficient (MPa K^{-1})
α, Isobaric thermal expension coefficient(K^{-1})
k_T, Isothermal compressibility (MPa^{-1})

Cp, Heat capacity at constant pressure (Joule mole^{-1} K^{-1})
B/A, Bayer's parameter
ρ, Density (kg m^{-3})

References:

[1] K Hanaki, J. Portugal-Pereira. *The Effect of Biofuel Production on Greenhouse Gas Emission Reductions.* In: Takeuchi K., Shiroyama H., Saito O., Matsuura M, editors. Biofuels and Sustainability. Tokyo: Science for Sustainable Societies. Springer, 53-71, 2018.

[2] H. K. Jeswani, A. Chilvers, and A. Azapagic, "Environmental sustainability of biofuels: a review," *Proc. R. Soc. A.*, 476(2243), 20200351, 2020.

[3] A. E. Atabani, A. S. Silitonga, I. A., Badruddin, et al., "A comprehensive review on biodiesel as an alternative energy resource and its characteristics," *Renewable and Sustainable Energy Reviews.*, 6(4), 2070-2093, 2012.

[4] El Hadji I. Ndiaye, M. Habrioux, João A. P. Coutinho, et al., "Sound speed, Density, and Derivative Properties of Ethyl Myristate, Methyl Myristate, and Methyl Palmitate under High Pressure," *Journal of Chemical & Engineering Data,* 58 (5), 1371-1377, 2013.

[5] K. Yamane, A. Ueta, Y. Shimamoto, "Influence of Physical and Chemical Properties of Biodiesel Fuels on Injection, Combustion and Exhaust Emission Characteristics in A Direct Injection Compression Ignition Engine," *International Journal of Engine Research*, 2(4), 249-261, 2001.

[6] M. Habrioux, Samuel V. D. Freitas, João A. P. Coutinho, et al., "High Pressure Density and Sound speed in Two Fuels," *Journal of Chemical & Engineering Data*, 58 (12), 3392-3398, 2013.

[7] El Hadji I. Ndiaye, D. Nasri, Jean Luc Daridon, "Sound speed, Density, and Derivative Properties of Fatty Acid Methyl and Ethyl Esters under High Pressure: Methyl Caprate and Ethyl Caprate," *Journal of Chemical & Engineering Data*, 57(10), 2667-2676, 2012.

[8] U. Yang, X. Wang, H.Tan, et al., "Experimental investigations on the thermophysical properties of methyl myristate in alcoholic solutions," *Fuel*, 215, 187-195, 2017.

[9] André F.G. Lopes, Maria del Carmen Talavera-Prieto, Abel G.M. Ferreira, et al., "Sound speed in pure fatty acid methyl esters and biodiesel fuels," *Fuel*, 116, 242-254,2014.

[10] J. Safarov, U. Ashurova, B. Ahmadov, et al., "Thermophysical properties of Diesel fuel over a wide range of temperatures and pressures," *Fuel*, 216, 870-889, 2018.

[11] E. Zorębski, "Internal pressure in liquids and binary liquid mixtures," *Journal of Molecular Liquids*, 149(1-2), 52-54, 2009.

[12] M. Dzida, S. Jężak, J. Sumara, et al., "High-Pressure Physicochemical Properties of Ethyl Caprylate and Ethyl Caprate," *J. Chem. Eng. Data*. 58(7), 1955–1962, 2013.

[13] C. M. Sehgal, "Nonlinear ultrasonics to determine molecular properties of pure liquids," *Ultrasonics*, 33(2), 155-161, 1995.

[14] E. V. Ivanov, V. K. Abrosimov, "Relationship between the internal pressure and cohesive energy density of a liquid nonelectrolyte. Consequences of application of Dack's concept," *J Struct. Chem.* 46, 856–861, 2005.

[15] J. M. Khadar, "Acoustic nonlinearity parameter B/A and related molecular properties of binary organic liquid mixtures," *Journal of Molecular Liquids.* 100(3), 217-227, 2002.

[16] El Hadji I. Ndiaye, M. Habrioux, João A. P. Coutinho, et al., "Sound speed, Density, and Derivative Properties of Methyl Oleate and Methyl Linoleate under High Pressure," *Journal of Chemical & Engineering Data*, 58(8), 2345-2354, 2013.

[17] P. Kumar, P. Kuchhal and N. Dass, "The pressure and temperature dependence of the velocity of sound in liquid metals," *J. Phys.: Condensed Matter,* 8, 10891, 1996.

[18] A. Kumar, P. Kuchhal, N. Dass, et al., "Anomalous behavior in sound velocity of water," *Physics and Chemistry of Liquids,* 49(4), 453-458, 2011.

[19] A. Schedemann, T. Wallek, M. Zeymer, et al., "Measurement and correlation of biodiesel densities at pressures up to 130MPa," *Fuel*, 107, 483-492, 2013.

[20] P. Kielczyński, M. Szalewski, A. Balcerzak, et al., "Thermodynamic method for measuring the B/A nonlinear parameter under high pressure," *IEEE International Ultrasonics Symposium (IUS)*, Prague, Czech Republic, 1665-1667, 2013.

Research Article

Thermodynamic Properties of Binary Liquid Mixtures Containing Furfural with Chlorobenzene, Nitromethane, Diethylmalonate and 1-Butanol at 308.15K and 318.15K Supported by FTIR Spectral Studies

[1]R. Uthirapathi[ID], [2]U.S. Kishnamoorthy[ID], [3*]R.V. Ambrose[ID]

[1,3]Department of Chemistry, St. Joseph's College (Autonomous),
Affiliated to Bharathidasan University, Tiruchirappalli, India.
[2]Department of Chemistry, Cauvery College for Women,
Affiliated to Bharathidasan University, Tiruchirappalli, India.
E-mails: [1]revathiuthirapathi.22@gmail.com, [3*]rosevenis@gmail.com

Abstract

A study on thermodynamic properties of the liquid mixture is used in the industrial process, which often extends to solution chemistry. Density(ρ)**,** Viscosity(η), and Ultrasonic velocity(**U**) were determined for binary liquid mixtures of furfural with chlorobenzene, nitromethane, diethyl malonate and 1- butanol at temperature of 308.15K and 318.15K at atmospheric pressure over the whole range of mole fractions. The calculated thermodynamic properties and some excess parameters such as Excess Volume($\mathbf{V^E}$), Deviation in Isentropic Compressibility($\mathbf{\Delta K_S}$)**,** Deviation in Viscosity($\mathbf{\Delta\eta}$)**,** Deviation in Intermolecular Free Length($\mathbf{\Delta L_F}$), Deviation in Intermolecular Free Volume($\mathbf{\Delta V_F}$), Deviation in Internal Pressure($\mathbf{\Delta\pi}$) and Deviation in Acoustic Impedance($\mathbf{\Delta Z}$) were calculated and applied to the Redlich-Kister type polynomial equation to determine the appropriate coefficients. The effects of composition and temperature on thermodynamic parameters have been studied in terms of molecule interaction in these liquid mixtures. Further, IR spectra of these liquid mixtures were recorded and the data were utilized to examine the mixing behavior of the components.

Keywords: *Furfural; molecular interaction; Redlich-Kister equation; thermodynamic parameters.*

1. Introduction

Furfural is the only unsaturated large-volume organic chemical created from carbohydrate resources and is a critical derivative for producing essential chemicals that cannot be acquired from petroleum, it is an important substance accessible from biomass [1]. The petrochemical, agricultural and polymer industries all employ it as a solvent [2]. The aprotic solvent nitromethane [3] has a strong polarity and is employed in a range of applications. Adhesives, paints, paint removers, polishes, dyes and medications are all made with chlorobenzene as a high boiling solvent. Diethyl malonate is a chemical that is utilized in the production of vitamins B1 and B6, as well as medicines, agrochemicals, flavor, and aroma compounds [4]. 1-Butanol is a useful solvent that is affordable and readily accessible in high purity. It's utilized in chemical and technical operations [5].

We investigated the molecular interaction between binary liquid mixtures of furfural with chlorobenzene, nitromethane, diethyl malonate and 1-butanol. Thermodynamic properties of Density (ρ), Viscosity (η), and Ultrasonic velocity (**U**) were measured over the entire composition range at temperature of 308.15K 318.15K. Excess Volume (**V^E**), Deviation in Isentropic Compressibility (**ΔK_S**), Deviation in Viscosity (**$\Delta\eta$**), Deviation in Intermolecular Free Length (**ΔL_F**), Deviation in Intermolecular Free Volume (**ΔV_F**), Deviation in Internal Pressure (**$\Delta\pi$**) and Deviation in Acoustic Impedance (**ΔZ**) have all been calculated based on the above measured data. The thermodynamic properties of liquid mixtures are needed in many industries, such as medicine, petroleum and chemical engineering [6]. These chemicals prompted the current thermodynamic analysis. Thermodynamic and transport properties of liquid and liquid mixtures are utilized to understand engineering applications such as heat transmission, mass transfer and fluid movement[7-8].Using the data from the aforementioned measurements, to investigate the nature of molecular interactions in liquid mixtures between unlike molecules.

2. Experimental
2.1. Material

Chlorobenzene (Merck, Mumbai, purity > 99%) was dried over anhydrous calcium chloride and distilled. Nitromethane (SRL, Mumbai, purity >99%), 1-butanol (Thermo fisher scientific, Mumbai, Purity >99%), were purified by distillation, and furfural (SRL, Mumbai, Purity >99%), and diethylmalonate (SRL, Mumbai, Purity >99%) were used without further purification. The purity of the pure compounds was also confirmed by comparing the measured density, viscosity, and ultrasonic velocity of the pure compounds at various temperatures with those described in the literature, which showed a fair agreement and is listed in Table 1 [9-15].

2.2. Measurement

For each mixture, a series of nine compositions were prepared, and their physical properties were measured at the relevant compositions on a mole fraction scale ranging from 0.1 to 0.9 in 0.1 increments [16]. Binary liquid mixtures of various compositions were made by combining a predetermined amount of pure liquids in 50ml airtight stopper bottles using an analytical balance with 0.0001g accuracy.

2.2.1. Density(ρ)

Densities of pure liquids and liquid mixtures were measured by specific gravity method [17] with 10 mL relative density bottle and weighed with an exactness of ± 0.001 kg m^{-3}.

$$\rho = \left[\frac{W \times d_0}{W_0} \right] \qquad (1)$$

Where 'w' is the mass of the liquid or liquid mixtures, 'w$_0$' is the mass of the water, and 'd$_0$' is the density of the water.

2.2.2. Viscosity (η)

Viscosities were determined by Oswald viscometer 10 mL capability with an accurateness of ± 0.001 cP [18]. From the measured values of density and flow time 't', viscosity 'η' was calculated. The values of constants were occurred by measuring the flow time with distilled water and pure nitrobenzene as standard liquids. The flow time were measured with electronic stop clock.

$$\eta = \left(At - \frac{B}{t} \right) \rho \qquad (2)$$

Where, 'ρ' is the density of a pure liquid or a combination of liquids, 't' is the time flow in seconds, and A and B characteristic constants at the specified temperature.

2.2.3. Ultrasonic Velocity

The ultrasonic velocity pure liquid and liquid mixtures values were measured using an ultrasonic interferometer (Pico, Chennai, India) with a frequency of 2MHz was calibrated [19] using water and nitrobenzene. The overall accuracy in the measurement is ±0.2%. All the measurements were taken using a digital thermostat with a temperature precision of 0.01K at 308.15K and 318.15K. The details of the methods and techniques of the measurements have been described earlier.

2.3. FTIR Study

The FTIR (Fourier transform infrared spectroscopy) spectra were recorded using a Perkin Elmer spectrum RX1 (PerkinElmer, inc., Waltham, MA, USA). FTIR properties have been used to study a specific interaction, such as the formation of a hydrogen bond between molecules that are dissimilar in liquid mixtures.

3. Theoretical approach
3.1. Excess Molar Volume (V^E)

The difference between the volume before and after mixing is called excess volume.

$$V^E = \left[\frac{(X_1 M_1) + (X_2 M_2)}{\rho} \right] - \left[\left(\frac{X_1 M_1}{\rho_1} \right) + \left(\frac{X_2 M_2}{\rho_2} \right) \right] \qquad (3)$$

X_1, M_1 and ρ_1, X_2, M_2 and ρ_2 are mole fraction, molar mass, and density of pure components 1 and 2 respectively [20].

3.2. Isentropic Compressibility (K$_S$)

Densities and ultrasonic velocities of liquids and liquid mixtures are used to indirectly and directly calculate isentropic compressibility.

$$K_S = \frac{1}{U^2 \rho} \qquad (4)$$

Where, 'U' is the speed of sound and 'ρ' is the density of the liquid mixtures.

3.3. Deviation of Isentropic Compressibility (ΔK$_S$)

$$\Delta K_S = K_S - (\Phi_1 K_{S1} + \Phi_2 K_{S2}) \qquad (5)$$

Where, 'ΔK$_S$' denotes the mixtures isentropic compressibility, Φ_1, K_1, S_1 and $\Phi_2, K_2 S_2$ denote the volume fraction and isentropic compressibility of pure components 1 and 2, respectively [21].

3.4. Excess viscosity (Δη)

$$\Delta \eta = \eta (X_1 \eta_1 + X_2 \eta_2^{'}) \qquad (6)$$

Where, η_1 and η_2 are the viscosity values of pure component 1 and 2 respectively.

3.5. Free Length

Values of ultrasonic velocity u and density of mixture ρ_{AB} were used to calculate inter molecular Free Length (L_f), Acoustic Impedance (Z) and intermolecular Free Volume (V_f) using the following relation [22] by

$$L_F = \frac{K}{U \rho^{1/2}} \qquad (7)$$

Where, U is ultrasonic velocity of pure liquid and liquid mixtures, and ρ is the density of pure and mixture, where K is Jacobson's constant which is temperature-dependant constant but independent of the nature of the liquid.

3.6. Acoustic Impedance

$$Z = U \rho \qquad (8)$$

Where, U is ultrasonic velocity of pure liquid and liquid mixtures, and ρ is the density of pure and mixture.

3.7. Free Volume

Intermolecular free volume has been calculated using the following relation [23].

$$V_F = \left[\frac{M_{eff} U}{(K \eta)} \right]^{3/2} \qquad (9)$$

Where, K is a temperature independent constant that is equal to 4.28 × 10^9 for all the liquids and M_{eff} is the effective molecular weight of the mixture.

3.8. Presentation of the research findings

The excess properties of Excess Volume (V^E), deviation in Isentropic Compressibility (ΔK_S), deviation in Viscosity ($\Delta\eta$), deviation in intermolecular Free Length (ΔL_F), deviation in intermolecular Free Volume (ΔV_F), deviation in Internal Pressure ($\Delta\pi$) and deviation in Acoustic Impedance (ΔZ) were fitted to Redlich–Kister type [23] polynomial equation.

$$\Delta A = X_1 X_2 \left[a + b(X_1 - X_2) c(X_1 - X_2) \right] \qquad (10)$$

The least-squares method was used to derive the adjustable parameters a, b and c.

The standard deviations (σ) presented in this work were computed using

$$\sigma = \left(\Sigma (X_{\exp} - X_{cal})^2 \mid N - n \right)^{1/2} \qquad (11)$$

Where, N is the number of data points, and n is the number of co-efficient. Coefficient values of the Redlich-Kister type polynomial equation (Eq.10) and standard deviation (Eq.11) at different temperatures are presented in Table 4.

4. Results and discussion
4.1. Excess thermodynamic parameters

Tables 2 and 3 signify the investigational values of density (ρ), viscosity (η), and ultrasonic velocity (U) and calculated values of excess volume (V^E), deviation in isentropic compressibility (ΔK_S) and deviation in viscosity ($\Delta\eta$) of all the four binary liquid mixtures at 308.15K and 318.15K.

In the pure state, furfural molecules are known to exist as associated molecules [25]. Over the entire range of composition, Excess Volume (V^E) and deviation in Isentropic Compressibility (ΔK_S) values of furfural with nitromethane are low negative (Figure 1 and Figure 2). The oxygen atom of furfural attracts the nitrogen atom of the nitro group, resulting in dipole-dipole interaction. However, there will be less nitro group interaction between the unlike molecules. Over the entire range of composition, Excess Volume (V^E) and deviation in Isentropic Compressibility (ΔK_S) values of furfural + chlorobenzene are negative (Figure 1 and Figure 2). The furfural carbonyl group has a polarity, which allows it to interact with the chlorine atom in chlorobenzene. As a result, it involves a dipole-dipole interaction.

Over the entire range of composition, Excess Volume (V^E) and deviation in isentropic compressibility (ΔK_S) values of furfural + 1-butanol are large negative (Fig. 1 and 2) values. The presence of substantial interactions between dissimilar molecules is demonstrated by the large negative V^E values of (furfural + 1-butanol) binary liquid mixtures. These findings suggest that furfural has a stronger interaction with 1-butanol, but alcohols are strongly self-associated by H-bonding, with degrees of association varying depending on chain length and temperature [26]. The presence of a significant dipole-dipole interaction between furfural and 1-butanol is shown by the negative V^E values.

Over the entire range of composition, Excess Volume (V^E) and deviation in Isentropic Compressibility (ΔK_S) values of furfural + diethyl malonate are negative (Figure1 and Figure 2). Because both esters and aldehydes have a carbonyl group, they become somewhat dipole due to the inductive action. The –O atom of the furfural can attract the –C atom of the ester group, resulting in dipole-dipole interaction [27]. An alkyl group is an electron-donating group, and its ability

to do so increases with the length of the ester molecules chain. Furthermore, the negative values found in this study indicate the effective packing effect generated by interstitial accommodation as the chain length of ester molecules rises, increasing intermolecular contact.

Over the entire composition range, the viscosity deviations of all four liquid mixtures are positive show figure 3. Figure 3 depicts the decline in positive values as temperature rises. Furfural + nitromethane have the lowest positive values, indicating that the intermolecular forces are greater than in other mixtures. This backs with the earlier theory that nitromethane interacts with furfural dispersion forces between furfural and 1-butanol and that the deviation from ideality is greater. Because the positive values of deviation in viscosity ($\Delta\eta$) for nitromethane, chlorobenzene, diethylmalonate, and 1-butanol are all greater than nitrobenzene and lower than 1-butanol, the interaction is less than nitromethane and higher than 1-butanol. Deviation in viscosity ($\Delta\eta$) graph's values are in the same order as excess volume (V^E) and deviation in isentropic compressibility (ΔK_S) values[27].

The observed values of intermolecular free length (ΔL_F), intermolecular free volume (ΔV_F) and intermolecular internal pressure ($\Delta\pi$) (Figures 4, 6 and 7) reflect the same idea as obtained above. For the four liquid mixtures, when the temperature rises, the intermolecular internal pressure ($\Delta\pi$) values of the liquid mixtures decrease and the intermolecular free volume (ΔV_F) values rise. Due to an increase in the thermal motion of interacting molecules, the nature of interaction for the four liquid mixtures reduces when the temperature is increased. Dispersion forces between mixing liquids cause negative values, while attractive forces like dipole-dipole interaction cause positive values.

Positive and negative deviation of the mixtures shows the level of association or dissociation between the mixing components [28-29], whereas deviation in acoustic impedance (ΔZ) acts in the opposite direction to intermolecular free length (ΔL_F). The observed values of deviation in viscosity ($\Delta\eta$) and deviation in acoustic impedance (ΔZ) are positive throughout the range (Figures 3 and Figures 5), confirming the stated hypothesis. Furfural + nitro methane < furfural + chlorobenzene < furfural + diethylmalonate < furfural + 1-butanol is the order of the interactions between the systems.

4.2. FTIR Results

Figures 8 to 11 show FTIR results for nitromethane, chlorobenzene, diethyl malonate, and 1-butanol in the binary liquid mixtures with furfural in a molar fraction of 0.5.

According to FTIR analysis, a pure furfural molecule shows a peak at 1686.93 cm⁻¹ which is due to the C=O bond, while an equimolar mixture of nitromethane, and chlorobenzene (Figure 8, 9) exhibits a peak at 1689.80 cm⁻¹, 1678.78 cm⁻¹ and 1679.30 cm⁻¹. Pure nitromethane liquid molecule shows a peak at 1576.88 cm⁻¹ which is due to the N=O bond, while an equimolar mixture of furfural + nitro methane (Figure 8) exhibits a peak at 1566.42 cm⁻¹. The change in the frequency and intensity confirms the existence of intermolecular interaction between –C=O and –N=O. Hence, it involves weak dipole-dipole interaction. Pure chlorobenzene liquid molecule shows a peak at 743.20 cm⁻¹ which is due to the -C-Cl bond, while an equimolar mixture of furfural + chlorobenzene (Figure 9) exhibits a peak at 751.30 cm⁻¹. The changes in the frequency and intensity confirm the existence of intermolecular interaction between –C=O and –C-Cl, hence, it involves dipole-dipole interaction.

A pure diethyl malonate molecule shows a peak at 1745.13 cm^{-1} which is due to the C=O bond. The equimolar mixture of furfural + diethyl malonate (Figure 10) shows a peak at 1691.24 cm^{-1} and 1740.38 cm^{-1} which is due to the C=O bond. The changes in the frequency and intensity confirm the existence of intermolecular interaction between carbon atom of the ester group and the oxygen atom of furfural, hence it involves dipole-dipole interaction.

A pure 1-butanol molecule has a peak at 3343.65 cm^{-1} which is characteristic of the –OH group. The equimolar mixture of furfural + 1-butanol (Figure 11) shows broad band at 3417.52 cm^{-1}. The change in frequency from 3343.65 to 3417.52 cm^{-1} and changes in intensity confirms the existence of an intermolecular hydrogen bond form between the –OH and –CHO group. These findings suggest that furfural has a stronger interaction with 1-butanol, but alcohols are strongly self-associated by H-bonding, with degrees of association varying depending on chain length and temperature. Hence it involves dipole-dipole interaction.

5. Conclusion

In this study Excess Volume (**V^E**), Deviation in Isentropic Compressibility (**ΔK$_S$**) and Deviation in Viscosity (**Δη**) for liquid mixtures of furfural with aromatic and aliphatic compounds are studied. The magnitude of Excess Volume (**V^E**), Deviation in Isentropic Compressibility (**ΔK$_S$**), Deviation in Viscosity **(Δη),** Deviation in Intermolecular Free Length (**ΔL$_F$**), Deviation in Intermolecular Free Volume (**ΔV$_F$**), Deviation in Internal Pressure **(Δπ)** and Deviation in Acoustic Impedance **(ΔZ)** has been interpreted in terms of molecular interactions between these molecules. Both **V^E**

and **ΔK$_S$** values are negative and the high positive value of Δη for furfural + 1-butanol shows more interaction between furfural and 1-butanol. For furfural + nitrometane mixtures the **V^E** and **ΔK$_S$** values are negative and Δη values are less positive due to less interaction between the mixing liquids. The existence of strong dipole-dipole interaction between furfural + chloro benzene, furfural + diethyl malonate, and furfural + 1-butanol, as well as less dipole-dipole interaction between furfural + nitromethane is proved by the values of excess properties. Because of thermal motion, the intermolecular interaction reduces as the temperature rises. To determine the variable coefficients, the corresponding thermodynamic excess parameters were calculated with the formulas reported earlier and fitted to a Redlich-Kister type polynomial equation. Based on the experimental and calculated results, the behavior of the liquid mixtures and deviation from ideality has been examined. An analysis of FTIR spectroscopy showed the establishment of hydrogen bonds between unlike molecules.

Nomenclature

V^E	Excess volume
K$_S$	Adiabatic compressibility
K	Jacobson's constant
X$_i$	Mole fraction of the ith component
A$_i$	Parameters of the ith component (Redlich–Kister equation Coefficients)
ρ$_{mix}$	Density of liquid mixture
n	Number of measurements
m	Number of adjustable parameters
t	Flow time

Appendix

Table 1. Comparison of Experimental Density (ρ), Viscosity (η), Ultrasonic Velocity (U) of Pure Liquids with literature Value at 308.15K and 318.15 K.

Liquids	T(K)	ρ(g cm^{-3})		η(mPa s^{-1})		U(ms^{-1})	
		Exp.	Lit.	Exp.	Lit.	Exp.	Lit.
Furfural [9,10]	308.15	1.1447	1.1440	1.2716	1.2600	1406.5	1403.77
	318.15	1.1324	1.1330	1.0921	1.0900	1370.5	1367.81
Chlorobenzene[11,12]	308.15	1.0892	1.0894	0.7002	0.7009	1221.5	1228
	318.15	1.0768	1.0794	0.5630	0.5629	1201.5	1208.5
Nitromethane[13]	308.15	1.1172	1.1176	0.5637	0.5640	1285	1277.1
	318.15	1.1038	1.1042	0.5171	0.5100	1278	-
1-Butanol[14]	308.15	0.7981	0.7979	2.0021	2.0080	1218	1209
	318.15	0.7935	0.7901	1.9022	1.5800	1207	-
Diethylmalonate[15]	308.15	1.0440	1.0418	1.6019	1 .6003	1245	1277.0
	318.15	1.0254	1.0283	1.4200	1.4235	1223	1235.5

Table 2. Physical and Thermodynamic Parameters for Binary liquid Mixtures of Furfural + Chlorobenzene, Furfural + Nitromethane, Furfural + 1-Butanol, and Furfural + Diethylmalonate at 308.15 and 318.15 K.

	308.15K						318.15K				
X_1	ρ (g cm^{-3})	η (mPa s^{-1})	U (ms^{-1})	ΔV^E (cm^{3}mol^{-1})	ΔKs (Tpa^{-1})	X_1	ρ (g cm^{-3})	η (mPa s^{-1})	U (ms^{-1})	ΔV^E (cm^{3}mol^{-1})	ΔKs (Tpa^{-1})
Furfural+ Chlorobenzene						**Furfural+ Chlorobenzene**					
0.0000	1.0892	0.7002	1221	0.0000	0.0000	0.0000	1.0768	0.5630	1201	0.0000	0.0000
0.1236	1.0958	0.7786	1259	-0.0866	-22.2245	0.1236	1.0833	0.6342	1235	-0.0742	-20.2950
0.1755	1.0987	0.8119	1274	-0.1219	-28.9691	0.1755	1.0860	0.6653	1248	-0.0997	-27.1024
0.2884	1.1049	0.8840	1300	-0.1803	-36.8044	0.2884	1.0923	0.7326	1273	-0.1574	-35.5091
0.4132	1.1121	0.9610	1325	-0.2380	-40.3508	0.4132	1.0995	0.8046	1296	-0.2142	-39.2356
0.5509	1.1200	1.0412	1351	-0.2631	-39.8437	0.5509	1.1072	0.8787	1320	-0.2288	-38.5934
0.6416	1.1252	1.0905	1366	-0.2528	-36.4652	0.6416	1.1124	0.9240	1333	-0.2169	-35.1921
0.7380	1.1305	1.1403	1381	-0.2149	-30.9757	0.7380	1.1177	0.9694	1346	-0.1767	-29.3556
0.8042	1.1341	1.1736	1390	-0.1737	-25.3147	0.8042	1.1213	1.0000	1354	-0.1336	-24.0008
0.9147	1.1401	1.2294	1400	-0.0837	-11.9791	0.9147	1.1275	1.0510	1363	-0.0635	-10.5845
1.0000	1.1447	1.2685	1406	0.0000	0.0000	1.0000	1.1324	1.0921	1375	0.0000	0.0000
Furfural+ Nitromethane						**Furfural+ Nitromethane**					
0.0000	1.1169	0.5635	1266	0.0000	0.0000	0.0000	1.1073	0.5145	1257	0.0000	0.0000
0.0955	1.1216	0.6352	1285	-0.0418	-2.6842	0.0955	1.1114	0.5725	1273	-0.0307	-2.1122
0.1822	1.1254	0.7006	1301	-0.0753	-4.4546	0.1822	1.1148	0.6271	1288	-0.0582	-4.0730
0.2729	1.1289	0.7691	1317	-0.1015	-5.6512	0.2729	1.1180	0.6842	1301	-0.0830	-5.1218
0.3996	1.1333	0.8624	1336	-0.1380	-6.0063	0.3996	1.1220	0.7620	1318	-0.1166	-5.4251
0.4968	1.1362	0.9316	1349	-0.1544	-5.9680	0.4968	1.1247	0.8190	1329	-0.1355	-5.2815
0.5907	1.1382	0.9960	1361	-0.1383	-5.4164	0.5907	1.1265	0.8722	1340	-0.1197	-4.8871
0.6954	1.1403	1.0655	1374	-0.1164	-4.6632	0.6954	1.1283	0.9281	1350	-0.0987	-4.0243
0.7999	1.1420	1.1342	1385	-0.0848	-3.6761	0.7999	1.1299	0.9838	1360	-0.0667	-2.8708
0.8929	1.1434	1.1948	1394	-0.0493	-2.3409	0.8929	1.1311	1.0332	1367	-0.0355	-1.5479
1.0000	1.1447	1.2685	1406	0.0000	0.0000	1.0000	1.1324	1.0921	1375	0.0000	0.0000
Furfural + 1-Butanol						**Furfural + 1-Butanol**					
0.0000	0.7985	1.9466	1201	0.0000	0.0000	0.0000	0.7909	1.8234	1183	0.0000	0.0000
0.0912	0.8292	1.9065	1255	-0.2284	-66.4956	0.0912	0.8210	1.7743	1226	-0.1899	-57.5297
0.1863	0.8621	1.8635	1298	-0.4670	-106.0557	0.1863	0.8534	1.7224	1268	-0.4144	-99.8946
0.2536	0.8857	1.8319	1322	-0.6250	-121.4938	0.2536	0.8768	1.6867	1291	-0.5833	-116.773
0.3530	0.9208	1.7811	1350	-0.7981	-130.9608	0.3530	0.9114	1.6326	1317	-0.7557	-127.415
0.4675	0.9609	1.7113	1374	-0.8883	-127.8928	0.4675	0.9512	1.5584	1340	-0.8489	-125.136
0.5561	0.9920	1.6478	1386	-0.8929	-116.6501	0.5561	0.9820	1.4880	1351	-0.8674	-114.568
0.6619	1.0291	1.5656	1395	-0.8483	-96.2282	0.6619	1.0188	1.3988	1358	-0.8220	-93.2678
0.7833	1.0716	1.4652	1401	-0.7007	-66.5358	0.7833	1.0605	1.2933	1364	-0.6599	-63.5723
0.9015	1.1119	1.3630	1406	-0.4166	-33.2236	0.9015	1.1005	1.1843	1369	-0.3762	-30.4705
1.0000	1.1447	1.2685	1406	0.0000	0.0000	1.0000	1.1324	1.0921	1375	0.0000	0.0000
Furfural + Diethylmalonte						**Furfural + Diethylmalonte**					
0.0000	1.0440	1.6019	1245	0.0000	0.0000	0.0000	1.0254	1.4200	1223	0.0000	0.0000
0.1678	1.0556	1.5726	1303	-0.2250	-43.0370	0.1678	1.0374	1.3865	1273	-0.1977	-39.6491
0.2467	1.0619	1.5554	1327	-0.3393	-56.5555	0.2467	1.0439	1.3692	1296	-0.3021	-54.1231
0.3357	1.0696	1.5329	1350	-0.4662	-66.9954	0.3357	1.0518	1.3475	1317	-0.4240	-65.0450
0.4376	1.0792	1.5027	1372	-0.5845	-73.3277	0.4376	1.0619	1.3175	1338	-0.5491	-71.8324
0.5016	1.0853	1.4827	1382	-0.6116	-73.6144	0.5016	1.0684	1.2973	1348	-0.5845	-72.5150
0.5836	1.0932	1.4535	1393	-0.5740	-70.4455	0.5836	1.0768	1.2683	1357	-0.5481	-68.9323
0.6801	1.1031	1.4157	1401	-0.4792	-62.1206	0.6801	1.0873	1.2303	1364	-0.4462	-60.3671
0.7553	1.1114	1.3849	1404	-0.3812	-51.6762	0.7553	1.0961	1.1992	1367	-0.3389	-49.6422
0.8499	1.1228	1.3425	1405	-0.2291	-34.8472	0.8499	1.1086	1.1582	1370	-0.2077	-34.2550
1.0000	1.1447	1.2685	1406	0.0000	0.0000	1.0000	1.1324	1.0921	1375	0.0000	0.0000

Table 3. Thermodynamic Parameters for binary liquid mixtures of Furfural + Chlorobenzene, Furfural + Nitromethane, Furfural + 1-Butanol and Furfural + Diethylmalonate at 308.15 and 318.15 K.

308.15K					318.15K				
$\Delta\eta$ (mPa.s)	ΔL_F (10^{-10} m)	ΔV_F (10^{-14} m^3mol^{-1})	ΔZ (kg m^{-3} s^{-1})	$\Delta\pi$(Pa)	$\Delta\eta$ (mPa.s)	ΔL_F (10^{-10} m)	ΔV_F(10^{-14} m^3mol^{-1})	ΔZ (kgm^{-3} s^{-1})	$\Delta\pi$(Pa)
Furfural+Chlorobenzene					Furfural+Chlorobenzene				
0.0000	0.0000	0.0000	0.0000	0.0000	0.0000	0.0000	0.0000	0.0000	0.0000
0.0079	-44.0821	-0.6831	15.2021	-18.5088	0.0059	-39.2563	-1.5300	12.1844	-16.97
0.0115	-57.5586	-0.8664	20.2562	-25.2567	0.0095	-52.7518	-1.9272	16.8683	-23.12
0.0191	-71.6937	-1.1163	25.3895	-37.3985	0.0170	-68.3330	-2.4204	22.2611	-34.22
0.0247	-77.7808	-1.1711	28.1975	-46.6535	0.0230	-74.8265	-2.4944	24.9890	-42.61
0.0263	-76.9120	-1.0451	29.3235	-51.1063	0.0243	-73.3177	-2.1913	25.5580	-46.72
0.0238	-70.4550	-0.8909	27.7817	-50.1193	0.0215	-66.6731	-1.8525	23.9089	-45.90
0.0184	-60.4403	-0.6824	25.0664	-45.0989	0.0158	-55.5401	-1.4112	20.6267	-41.40
0.0140	-49.5817	-0.5236	21.1800	-38.5872	0.0115	-45.4179	-1.0781	17.3416	-35.57
0.0065	-23.0278	-0.2395	9.9586	-20.5165	0.0040	-18.8559	-0.4877	6.8425	-19.07
0.0000	0.0000	0.0000	0.0000	0.0000	0.0000	0.0000	0.0000	0.0000	0.00
Furfural+ Nitromethane					Furfural+Nitromethane				
0.0000	0.0000	0.0000	0.0000	0.0000	0.0000	0.0000	0.0000	0.0000	0.0000
0.0046	-21.3651	-0.1520	8.9699	-5.4167	0.0029	-18.9283	-0.1479	7.6592	-5.37
0.0092	-35.5900	-0.2339	15.2748	-8.4448	0.0074	-33.0545	-0.2426	13.7694	-8.26
0.0141	-45.5582	-0.2808	19.9551	-10.1756	0.0121	-42.2654	-0.3016	17.9214	-9.87
0.0184	-51.4519	-0.2947	23.0342	-10.8150	0.0167	-47.7103	-0.3270	20.6227	-10.40
0.0193	-51.7365	-0.2756	23.6062	-10.2863	0.0175	-47.7379	-0.3088	20.9569	-9.85
0.0179	-47.7381	-0.2397	22.0683	-9.1640	0.0165	-44.2652	-0.2702	19.6811	-8.75
0.0139	-40.5031	-0.1857	19.0770	-7.3646	0.0119	-36.9853	-0.2060	16.6496	-7.02
0.0092	-30.2718	-0.1247	14.5941	-5.1267	0.0072	-26.6581	-0.1366	12.1316	-4.88
0.0046	-18.1270	-0.0668	8.9392	-2.8594	0.0030	-15.0560	-0.0719	6.8818	-2.72
0.0000	0.0000	0.0000	0.0000	0.0000	0.0000	0.0000	0.0000	0.0000	0.0000
Furfural+ 1-Butanol					Furfural+ 1-Butanol				
0.0000	0.0000	0.0000	0.0000	0.0000	0.0000	0.0000	0.0000	0.0000	0.0000
0.0215	-173.3999	-0.0393	22.1752	-157.5226	0.0176	-151.1061	-0.0741	14.8381	-149.49
0.0429	-282.9059	-0.0896	38.7503	-253.0650	0.0353	-267.5252	-0.1456	30.9964	-247.79
0.0568	-328.3991	-0.1189	46.9876	-290.6030	0.0488	-317.0196	-0.1935	39.1950	-285.10
0.0732	-359.2705	-0.1581	54.4988	-314.6294	0.0674	-350.9433	-0.2592	46.3873	-307.85
0.0808	-354.9281	-0.1931	57.4490	-310.0351	0.0769	-348.5912	-0.3202	49.1777	-302.94
0.0772	-325.8910	-0.2098	54.4753	-287.3289	0.0712	-321.4549	-0.3497	46.8838	-282.17
0.0665	-270.8575	-0.2143	46.6146	-241.3832	0.0594	-263.6740	-0.3616	38.1562	-237.57
0.0483	-188.8896	-0.1895	33.9520	-168.7042	0.0427	-181.0233	-0.3263	26.0477	-166.35
0.0260	-95.2550	-0.1175	19.3192	-81.7851	0.0201	-87.4339	-0.2043	12.7601	-81.34
0.0000	0.0000	0.0000	0.0000	0.0000	0.0000	0.0000	0.0000	0.0000	0.0000
Furfural+ Diethylmalonate					Furfural+ Diethylmalonate				
0.0000	0.0000	0.0000	0.0000	0.0000	0.0000	0.0000	0.0000	0.0000	0.0000
0.0261	-71.9542	0.0598	24.5378	-48.8113	0.0215	-60.4147	0.0674	16.9742	-43.32
0.0350	-93.8008	0.0764	33.3132	-70.3294	0.0301	-83.5236	0.0897	25.1250	-62.42
0.0419	-109.7558	0.0877	40.6589	-92.9290	0.0375	-99.6305	0.1012	31.5104	-82.44
0.0453	-118.1871	0.0938	45.8595	-115.6474	0.0410	-108.4466	0.1093	36.0901	-102.55
0.0465	-116.1241	0.0889	45.9599	-127.4323	0.0417	-107.1919	0.1057	36.4373	-112.99
0.0444	-106.8960	0.0810	43.0712	-138.6472	0.0397	-96.5939	0.0950	32.9721	-122.86
0.0385	-89.1171	0.0679	36.4185	-143.6568	0.0333	-78.2090	0.0818	26.5077	-127.27
0.0325	-69.4722	0.0514	28.2102	-138.2061	0.0268	-58.1819	0.0640	18.8192	-122.47
0.0213	-42.2410	0.0320	16.7363	-113.5611	0.0168	-36.5278	0.0457	11.5587	-100.79
0.0000	0.0000	0.0000	0.0000	0.0000	0.0000	0.0000	0.0000	0.0000	0.0000

Table 4. Coefficient values of Redlich-kister type polynomial equation and standard deviation at different temperatures.

T/K	a	b	c	σ
Furfural+ Chlorobenzene				
V^E(cm^{3}mol^{-1})				
308.15	-1.0337	-0.0300	0.0214	0.0018
318.15	-0.8987	-0.8987	0.0329	0.0031
η (mPa.s)				
308.15	4.0455	0.2869	0.9811	0.1026
318.15	3.4041	0.2654	0.8203	0.0856
ΔK_S(Tpa^{-1})				
308.15	-160.6080	8.0902	-4.5168	0.6174
318.15	-155.6480	7.9220	-2.5607	0.4235
$\Delta\eta$(mPa.s)				
308.15	4.0455	0.2869	0.9811	0.0005
318.15	3.4041	0.2654	0.8203	0.0007
ΔZ (kg m^{-3} s^{-1})				
308.15	120.4250	-0.5614	3.5045	0.3478
318.15	105.3910	-1.0116	0.5962	0.0483
ΔL_F (10^{-12} m)				
308.15	-3.1776	0.0860	-0.0914	0.0082
318.15	0.0989	0.1264	-0.2291	0.0217
ΔV_F (10^{-14} m^{3}mol^{-1})				
308.15	-4.3863	0.2856	-0.0995	0.0053
318.15	-9.2586	0.6909	-0.2810	0.6780
$\Delta\pi$(10^{-05} Nm^{-2})				
308.15	-204.4740	-7.4226	-0.9531	0.1846
318.15	-186.9700	-6.9596	-1.1874	0.2027
Furfural+ Nitromethane				
V^E(cm^{3}mol^{-1})				
308.15	-0.5755	-0.0023	0.0160	0.0016
318.15	-0.4946	-0.4946	0.0255	0.0025
η (mPa.s)				
308.15	3.7323	0.3501	0.9192	0.0863
318.15	3.2806	0.2880	0.7972	0.0757
ΔK_S(Tpa^{-1})				
308.15	-24.3693	-0.5687	-0.3952	0.0428
318.15	-22.2040	-0.4114	0.3189	0.0375
$\Delta\eta$(mPa.s)				
308.15	3.7323	0.3501	0.9102	0.0004
318.15	3.2807	0.2880	0.7972	0.0006
ΔZ (kg m^{-3} s^{-1})				
308.15	94.0036	-1.1537	0.7473	0.0801
318.15	83.9778	-1.6584	-0.4472	0.0328
ΔL_F (10^{-10} m)				
308.15	-2.0647	0.0517	-0.0179	0.0021
318.15	0.0692	0.0564	-0.1191	0.0119
ΔV_F (10^{-14} m^{3}mol^{-1})				
308.15	-1.1049	0.0841	-0.0151	0.0016
318.15	-1.2319	0.0822	0.0046	0.0912
$\Delta\pi$(10^{-04} Nm^{-2})				
308.15	-414.0070	25.8787	-6.7420	0.8219
318.15	-396.8830	26.2209	-7.7625	0.9232

Table 4. Coefficient values of Redlich-kister type polynomial equation and standard deviation at different temperatures (Continued).

Furfural+1-Butanol			
$V^E (cm^3 mol^{-1})$			
308.15	-3.5997	-0.1167	-0.0219	0.0001
318.15	-3.4603	-3.4603	0.0256	0.0048
$\eta (mPa.s)$			
308.15	6.7471	-0.3380	1.6016	0.1633
318.15	6.1194	-0.3654	1.4453	0.1498
$\Delta K_S (Tpa^{-1})$			
308.15	-495.3510	38.1970	-112.4146	0.8741
318.15	-485.6340	35.4538	-114.8937	0.1754
$\Delta \eta (mPa.s)$			
308.15	6.7471	-0.3380	1.6016	0.0007
318.15	6.1195	-0.3654	1.4454	0.0012
$\Delta Z (kg\ m^{-3}\ s^{-1})$			
308.15	225.1470	-5.1840	1.8690	0.2817
318.15	192.2600	-4.9386	-4.6036	0.3568
$\Delta L_F (10^{-10}\ m)$			
308.15	-13.9677	0.7926	-0.2574	0.0403
318.15	0.6291	0.4396	-0.9361	0.1000
$\Delta V_F (10^{-14}\ m^3 mol^{-1})$			
308.15	-0.9385	-0.0608	0.0257	0.0082
318.15	-1.4682	-0.1074	0.0008	0.1082
$\Delta \pi (10^{-05}\ Nm^{-2})$			
308.15	-122.9580	7.1849	-2.6324	0.3945
318.15	-120.7240	6.8046	-2.3832	0.3629

Furfural+ Diethylmalonate			
$V^E (cm^3 mol^{-1})$			
308.15	-2.3454	-0.0364	0.2180	0.0141
318.15	-2.2077	-2.2077	0.2422	0.0157
$\eta (mPa.s)$			
308.15	5.9313	-0.1673	s1.4348	0.0934
318.15	5.1895	-0.1665	1.2493	0.0812
$\Delta K_S (Tpa^{-1})$			
308.15	-274.3760	33.9457	-67.8867	0.6873
318.15	-268.7230	33.5111	-66.2114	0.5818
$\Delta \eta (mPa.s)$			
308.15	5.9313	-0.1673	1.4349	0.0001
318.15	5.1896	-0.1665	1.2493	0.0004
$\Delta Z (kg\ m^{-3}\ s^{-1})$			
308.15	181.6370	-4.2740	-8.5935	0.5842
318.15	140.8350	-4.0531	-11.2746	0.7592
$\Delta L_F (10^{-10}\ m)$			
308.15	-4.6094	0.2074	0.1029	0.0077
318.15	0.1865	0.2522	-0.5622	0.0357
$\Delta V_F (10^{-14}\ m^3 mol^{-1})$			
308.15	0.3389	-0.0214	0.0081	0.0008
318.15	0.4023	-0.0189	0.0121	0.0333
$\Delta \pi (10^{-03}\ Nm^{-2})$			
308.15	5.1216	-0.6018	-0.2647	0.8672
318.15	-4.5666	-0.5331	-0.2364	0.0180
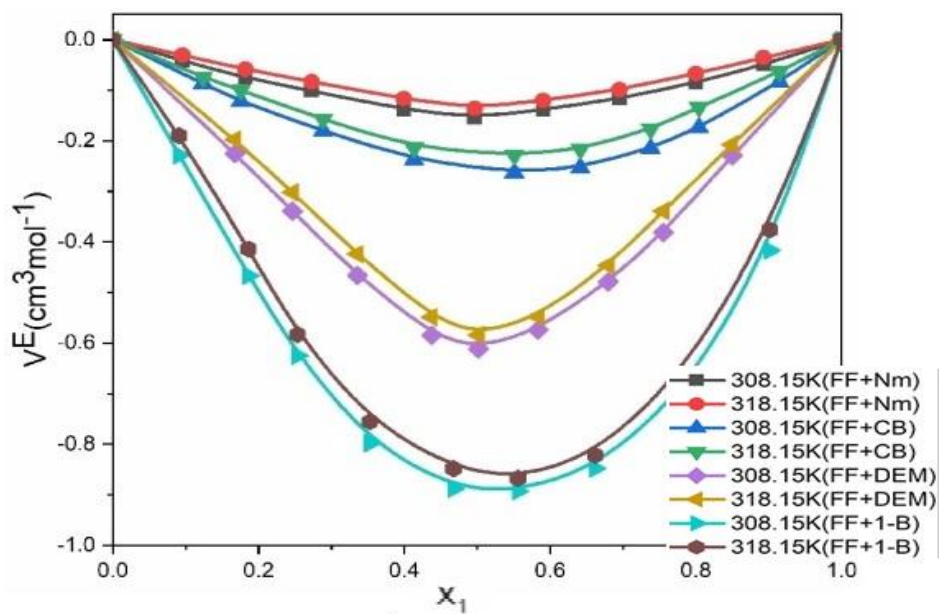
Figure 1. Excess volume (V^E) against the mole fraction (X_1) of Furfural at 308.15K and 318.15 K for the binary liquid mixtures of Furfural with Nitromethane, Cholobenzene, Diethylmalonate and 1-Butanol.
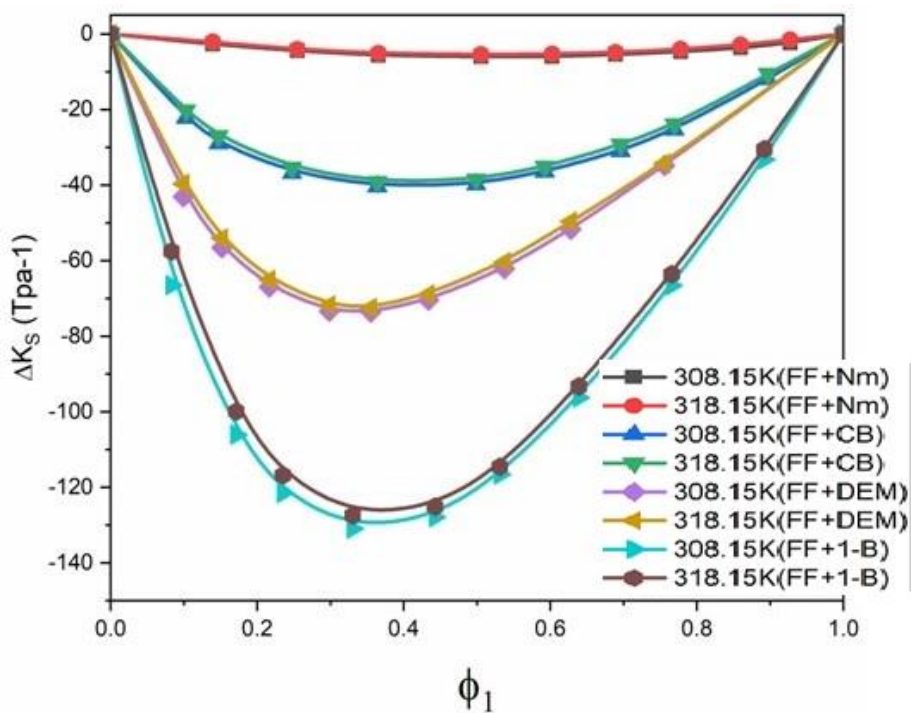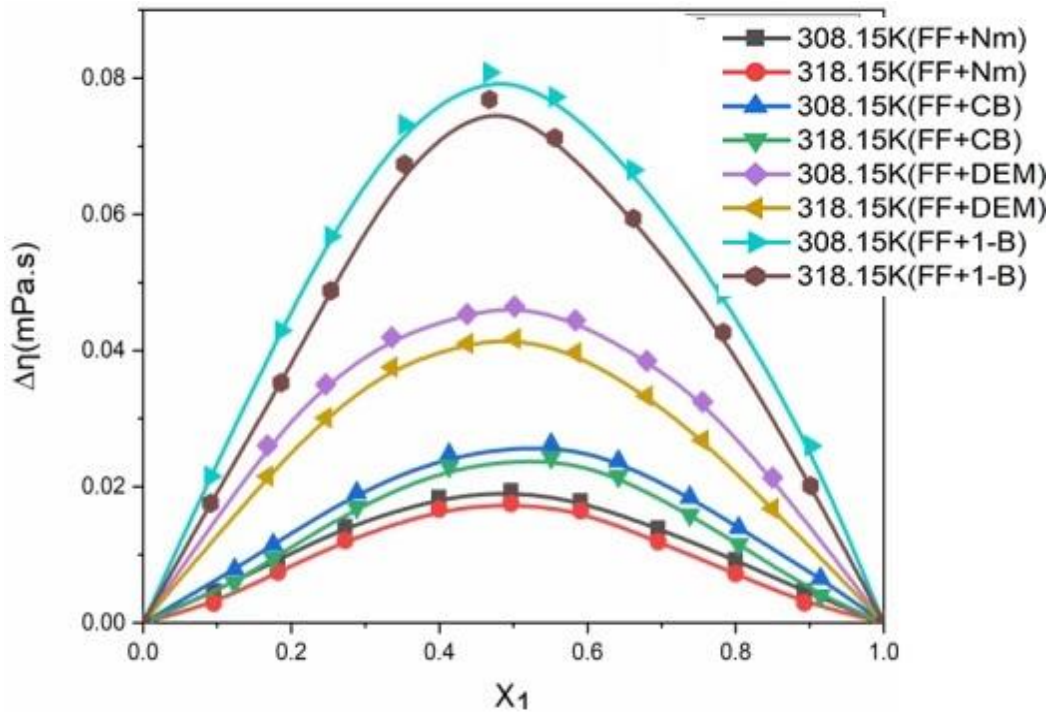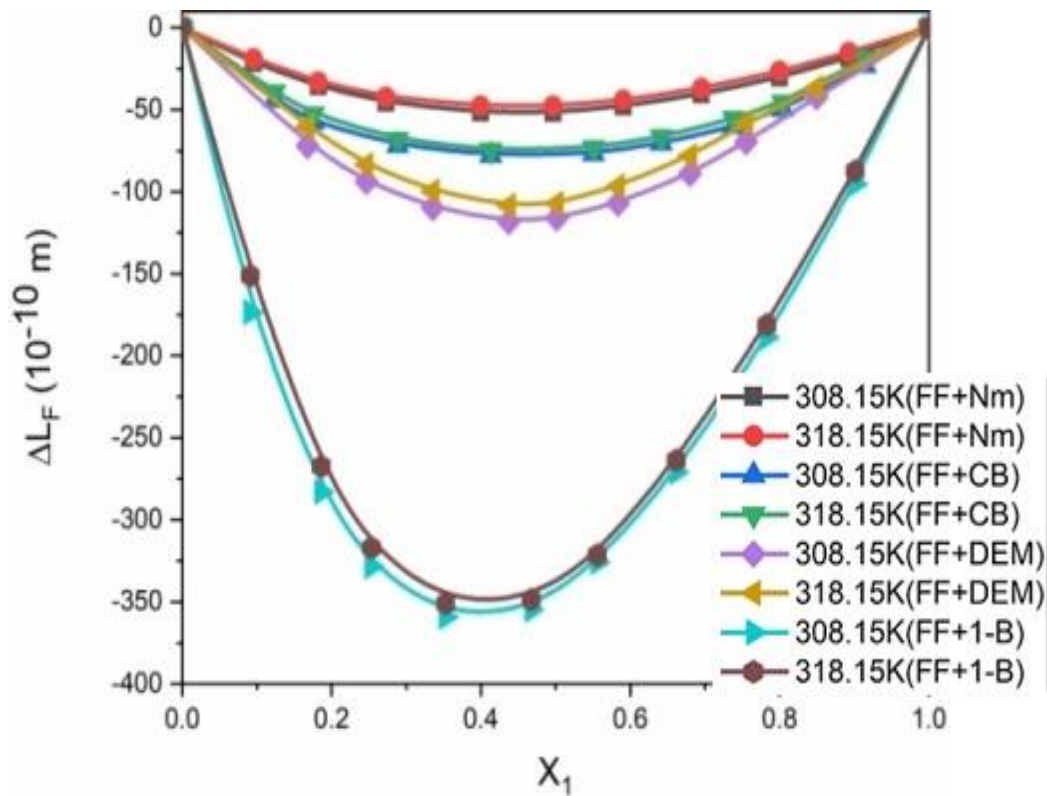

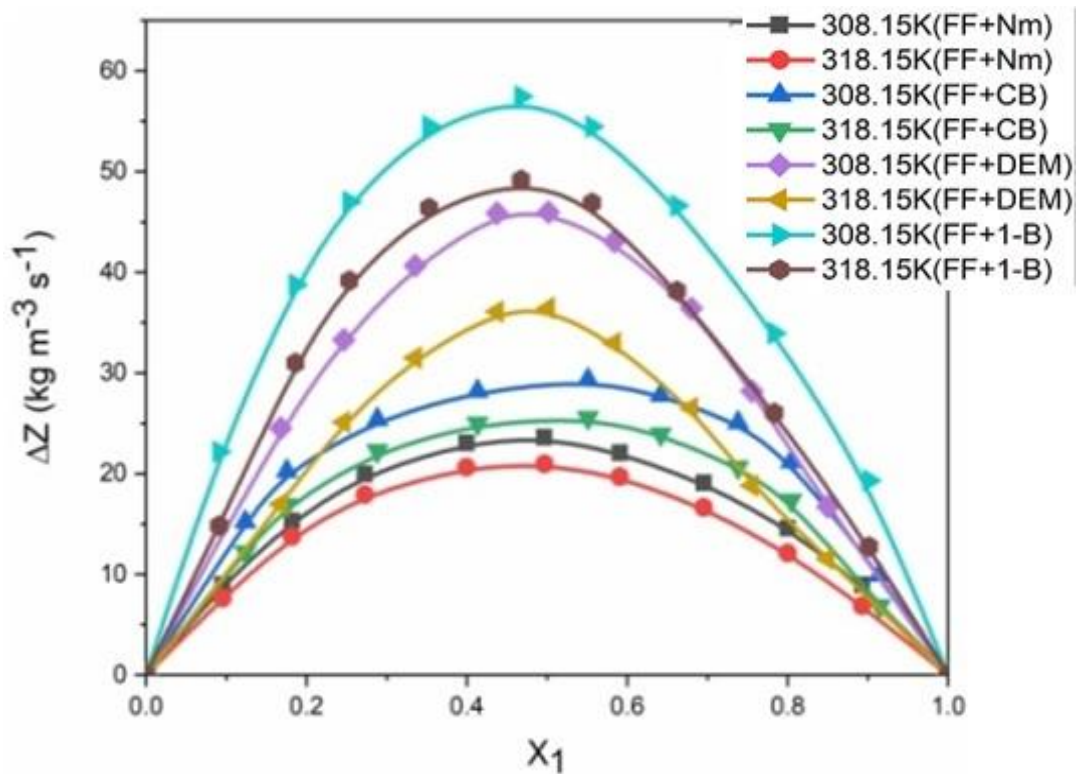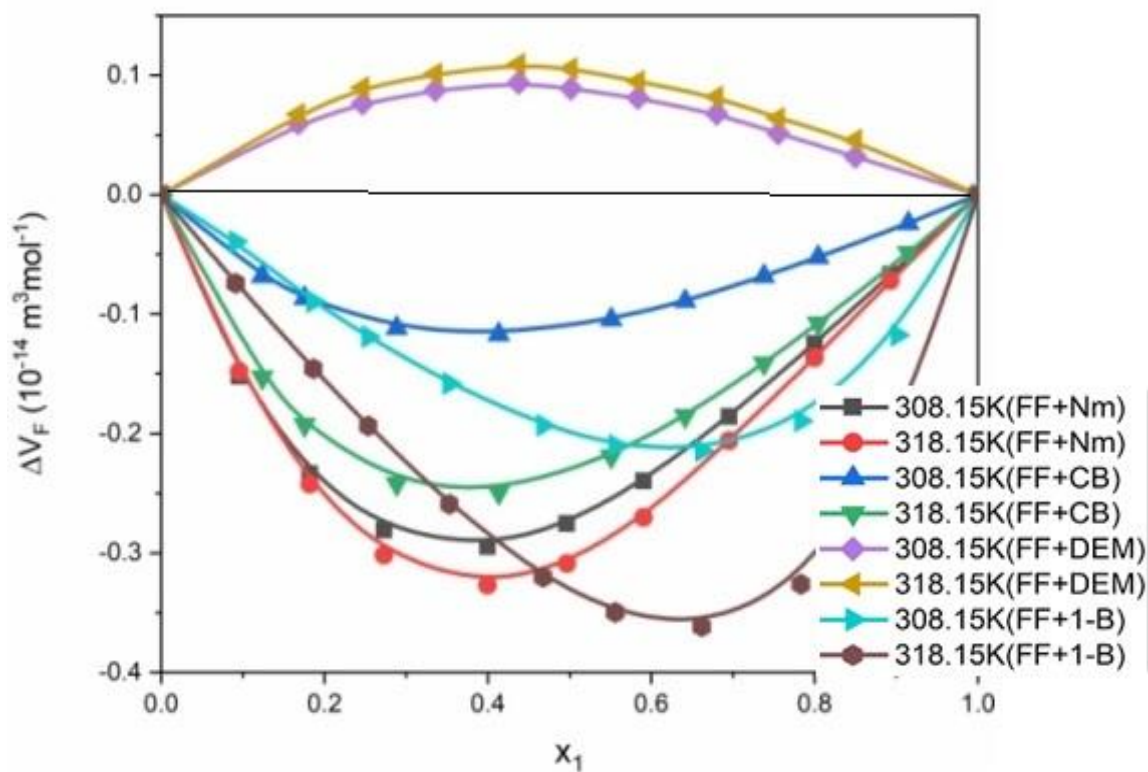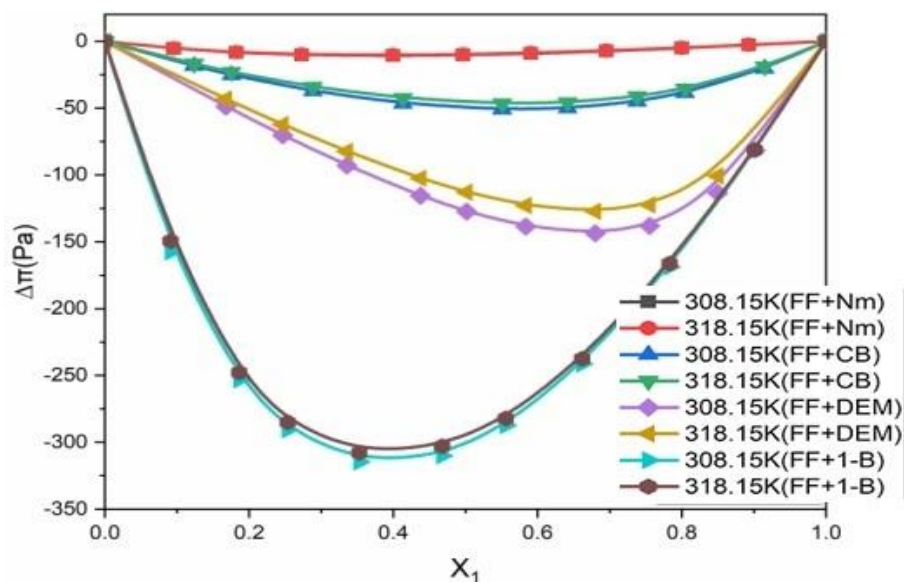*Figure 2. Deviation in isentropic compressibility (ΔK_S) against the Volume fraction (Φ_1) of Furfural at 308.15K and 318.15 K for the binary liquid mixtures of Furfural with Nitromethane, Cholobenzene, Diethyl malonate and 1-Butanol.*

Figure 3. Deviation in viscosity (Δη) against the mole fraction (X₁) of Furfural at 308.15K and 318.15 K for the binary liquid mixtures of Furfural with Nitromethane, Cholobenzene, Diethyl malonate and 1-Butanol.

Figure 4. Intermolecular free length (ΔL_F) against the mole fraction of Furfural at 308.15K and 318.15 K for the binary liquid mixtures of Furfural with Nitromethane, Cholobenzene, Diethyl malonate and 1-Butanol.

Figure 5. Deviation of acoustic impedance (ΔZ) against the mole fraction (X₁) of Furfural at 308.15K and 318.15 K for the binary liquid mixtures of Furfural with Nitromethane, Cholobenzene, Diethyl malonate and 1-Butanol.

Figure 6. ΔV_F against the mole fraction of Furfural at 308.15K and 318.15 K for the binary liquid mixtures of Furfural with Nitromethane, Cholobenzene, Diethyl malonate and 1-Butanol

Figure 7. Intermolecular internal pressure (Δπ) against the mole fraction (X₁) of Furfural at 308.15K and 318.15 K for the binary liquid mixtures of Furfural with Nitromethane, Cholobenzene, Diethyl malonate and 1-Butanol.
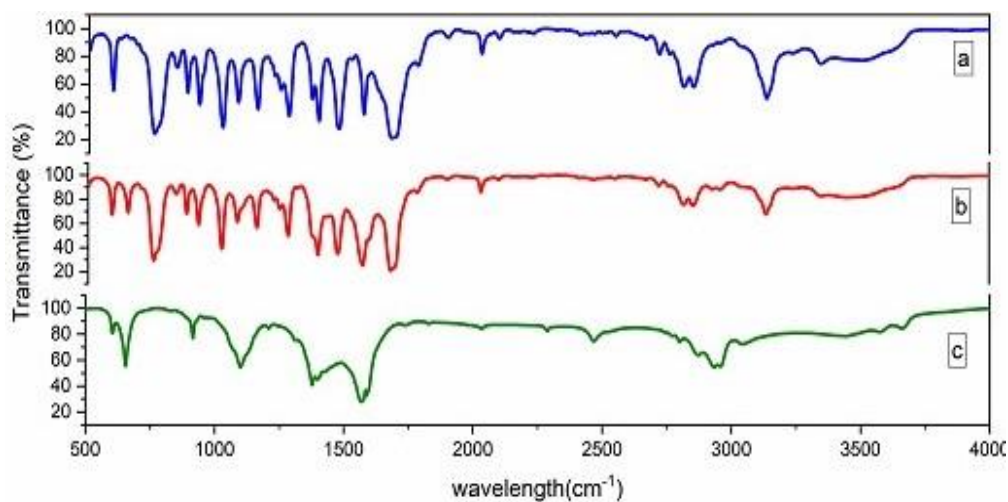
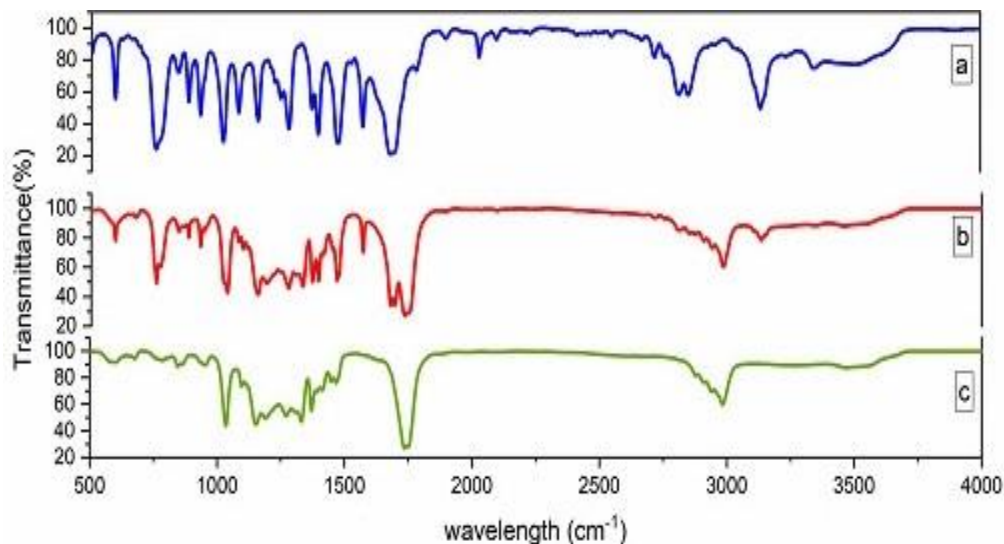*Figure 8. FTIR spectrum. (a) Pure furfural liquid, (b) equimolar mixture of furfural + nitromethane, (c) Pure nitromethane liquid.*
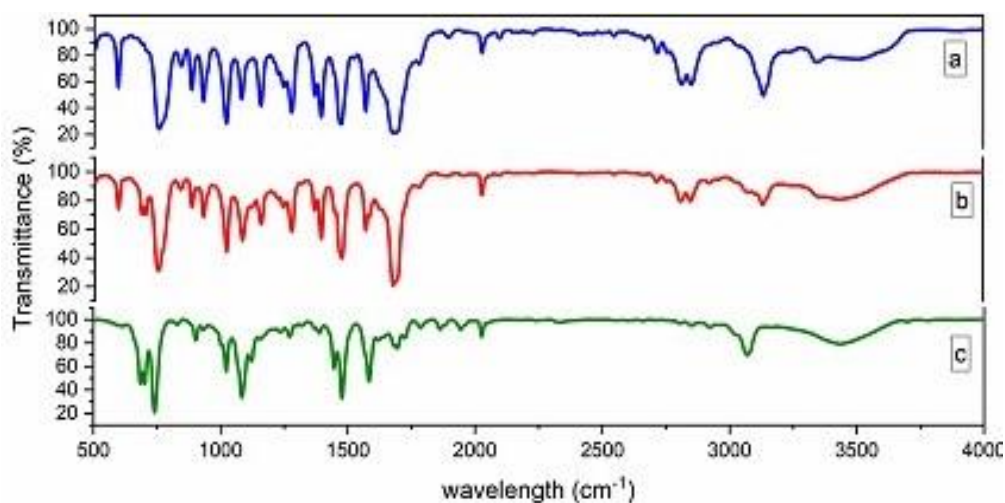
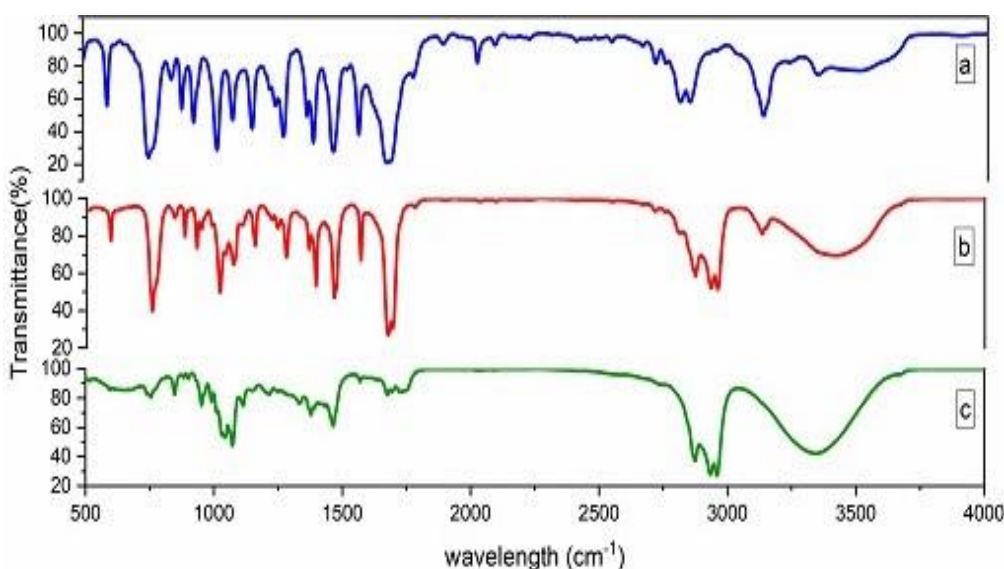*Figure 9. FTIR spectrum. (a) Pure furfural liquid, (b) equimolar mixture of furfural + chlorobenzene, (c) Pure chlorobenzene liquid.*

Figure 10. FTIR spectrum. (a) Pure furfural liquid, (b) equimolar mixture of furfural + diethylmalonate, (c) Pure diethylmalonate liquid.

Figure 11. FTIR spectrum. (a) Pure furfural liquid, (b) equimolar mixture of furfural + 1-butanol, (c) Pure 1-butanol liquid.

References

[1] L. Lomba, B. Giner, M. C. Lopez, "Thermophysical properties of furfural compounds", *J. Chem. Eng. Data., 59(2),* 329-338, 2014.

[2] M. Saad Qureshi, P. Vrbka, V. Dohnal, "Thermodynamic properties of five biofuel-relevant compounds at infinite dilution in water", *Fuel., 191,* 518-527, 2017.

[3] M. Almasi, L. Mousavi, "Excess molar volumes of binary mixtures of aliphatic alcohols (C1–C5) with Nitromethane over the temperature range 293.15 to 308.15 K: Application of the ERAS model and cubic EOS", *J. Mol. Liq., 163*, 46-52, 2011.

[4] K. Uma Sivakami, S. Vaideeswaran and A. Rosevenis, "Thermodynamic properties and interaction abilities of ternary liquid mixtures at 308.15K and 318.15K", *J. Environ. Nanotechnol., 7(3),*22, 2018.

[5] B. Satheesh, J. K. Ega, K. Siddoju, S. Marupati, Tangeda *Savitha* Jyostna, "Thermodynamic properties of binary liquid mixtures of isoamyl alcohol with heterocyclic compounds at varying temperatures", C*hem. Data Coll., 37*, 100812, 2022.

[6] A.Sharma, M.Rani, S.Maken, "Thermodynamics of haloarenes with n-hexane at 298.15–318.15 K: Density, Ultrasonic Speed and Viscosity", *J. Mol. Liq., 321,* 14366, 2021.

[7] S. Karlapudi, R.L. Gardas, P. Venkateswarlu, K. Sivakumar, "FT-IR studies on excess thermodynamic properties of binary liquid mixtures o-chlorotoluene with 1-propanol, 1-butanol, 1-pentanol, 1-hexanol and 1-heptanol at different temperatures", *J. Chem. Thermodyn., 67,* 203-209, 2013.

[8] K. Uma Sivakami, S. Vaideeswaran, A. Rose Venis, K. Shenbagam, "Study on Interaction Capabilities of Ternary Liquid Mixtures by Thermodynamic Parameters at 308.15 K", *Int. J. Thermodyn., 25(2),* 040-048, 2022.

[9] R. Umapathi, C.Narasimha Rao, P. Naidoo, "Effect of temperature on molecular interactions betweentri(butyl) methylphosphonium methylsulfate and furfural", *J. Chem. Thermodyn., 149,* 106150, 2020.

[10] L. Lomba, B. Giner, I. Bandres, "physicochemical properties of green solvent derived from biomass", *Green Chem., 13,* 2062-2070, 2011.

[11] P. Prabhu, A. Rose Venis, "Molecular interaction of hexylene glycol with toluene, aniline, chlorobenzene, nitrobenzene, benzaldehyde and N,N-dimethylaniline at 308.15 and 318.15 K", *Phys. Chem. liq., 58,* 529-544, 2020.

[12] K. Narendra, B. Sudhamsa, M. Sarath Babu, "Study of molecular interactions in binary mixtures of diethyl carbonate + benzene derivatives at different temperatures", *J. Appl. Sol. Chem. Mod., 4,*119-127, 2015.

[13] M. S. Rahman, A.M. Saleh, F. Islam Chowdhury, "Density and viscosity for the solutions of 1-butanol with nitromethane and acetonitrile at 303.15 to 323.15 K", *J. Mol. Liq., 190,* 208-214, 2014.

[14] H.E. Hoga, RB. Torres, "Volumetric and viscometric properties of binary liquid mixtires of {methyl tert butyl ether(MTBE)+alcohol} at several temperatures and p=0.1

[19] U. Revathi, K. Uma Sivakami, P. Prabhu, "A study on thermodynamic properties of binary liquid mixtures of diethylmalonate with toluene and chlorobenzene at 308.15K and 318.15K", *World J. Pharm. Pharm. Sci., 6,* 857, 2017.

[20] D. K. Sharma, S. Agarwal, "Free Volume and Internal Pressure of Binary Liquid Mixtures from Ultrasonic Velocity at 303.15 K", Int. J. Thermodyn.*, 25(2)*, 016-022, 2022.

[21] C.V. Suryanarayana and J. Kuppusamy, "Free volume and internal pressure of liquids from ultrasonic velocity, *J. Acoust. Soc. India, 4,* 75, 1976.

[22] P. Prabhu and A. Rose Venis, "Thermodynmic properties of binary liquid mixtures of methyl benzoate with chlorobenzene and benzaldehyde at 308.15 and 318.15K", *Asian J. Chem., 30(8)*, 1759-1764, 2018.

[23] K. Uma Sivakami, S. Vaideeswaran and A. Rosevenis, "Density, viscosity, ultrasonic velocity and excess thermodynamic parameters of ternary liquid mixtures of morpholine + 1,4-dioxane + toluene or nitrobenzene at 308.15 K", *J. Serb. Chem. Soc., 83(10),* 1131–1142, 2018.

[24] M. Zaoui-Djelloul-Daouadji, L. Bendiaf, I. Bahadur, "Volumetric and acoustic properties of binary systems

MPa: Experimental results and application of the ERAS mode", *J. Chem. Thermodyn., 43,* 1104-1134, 2011.

[15] P. Prabhu, U. Revathy, A. Rose Venis, "Transport properties of diethyl malonate with aniline and benzaldehyde at 308.15 and 318.15 K", *Asian J. Chem., 6,* 1325-1330, 2018.

[16] S. Felixa, U. Sivakami and R. Venis, "Molecular interaction in ternary liquid mixtures of 1,2-dichlorobenzene with cyclohexane and toluene at 318K", *World J. Pharm. Pharm. Sci., 5,*1602, 2016.

[17] U. Revathi, A. Rose Venis, "Thermodynamic parameters of a ternary liquid mixture at 308.15K and 318.15K", *J. Emerg. Technol. Innov. Res., 4,* 6, 2019.

[18] D. Ubagaramary, M. Enoch and Kesavaswamy, "comparative study of molecular interactions in binary liquid mixtures of 4-methyl-2-pentanonewith butan-2-one, furfuraldehyde, cyclohexanone at 308 K", *Orient. J. Chem., 32(1),* 321-330, 2016.

(furfural or furfuryl alcohol + toluene) and (furfuryl alcohol + ethanol) at different temperatures", *Thermochim Acta., 611,* 47-55. 2015.

[25] L..M. Follegatti-Romero, F.H.B. Sosa, M.C. Costa, "Excess volumes and partial molar volumes of binary liquid mixtures of furfural or 2-methylfuran with alcohols at 298.15 K", *J. Chem. Thermodyn., 134,* 20-30, 2019.

[26] L. Bendiaf, I. Bahadur, A. Negadi, "Effects of alkyl group and temperature on the interactions between furfural and alcohol: Insight from density and sound velocity studies", *Thermochim Acta., 599,* 13-22, 2015.

[27] O. Redlich and A. T. Kister, "Algebraic Representation of Thermodynamic Properties and the Classification of Solutions", *Ind. Eng. Chem., 40*, 345, 1948.

[28] R. Rajalakshmia, S. Ravikumara, K. Sivakumarb, "Excess thermodynamic properties of intermolecular interactions in binary liquid mixtures of furfural with alkyl acetates (C1-C5) at different temperatures", *J. chem. data coll., 24,* 100299, 2019.

[29] S. Kumar, P. Jeevanandham, "Densities, viscosities, refractive indices and excess properties of aniline and o-anisidine with 1-alkoxyethanols at 303.15K", *J. Mol. Liq., 174*, 34-41, 2012.

Research Article

Emissivity Prediction for an IR Camera During Laser Welding of Aluminum

*A. Metallo ⓘD

Industrial Engineering Department, University of Salerno, Italy
E-mail: antonio.metallo@libero.it

Abstract

Laser processing is becoming increasingly important in industrial applications. The success of the process relies on two fundamental parameters: the surface temperature of the medium and the thickness of the hardened layer. One of the most important factors during a laser process is certainly the temperature, which presents high temperature gradients. The speed at which a material undergoes a phase transition, the chemical reactions that take place during processing and the properties of the material are all dependent on temperature changes. Consequently, the measure of temperature is a demanding undertaking. This study proposes to measure temperature for the duration of laser welding with the infrared camera (IR) Optris PI. To restore the real temperature based on the brightness temperature values measured by the IR camera is needed to evaluate the emissivity to be attributed to the IR camera. For this purpose, firstly, the isotherms consistent with the melting point of aluminum (785 K) were assessed and then compared with the temperature distribution gauged in the zone of irradiation of the laser. Such data were then compared with the thickness of the melted zone. The use of the melting point isotherm allowed the calculation of the value of emissivity and the restoration of the temperature. Thermography software data acquisition wrongly presupposes the emissivity value does not change. This generates incorrect thermographic data. The surface emissivity normally hinges on temperature. Therefore, the values on which the literature relies may not work for materials of interest in the conditions of the process. This is particularly the case, where welding is carried out in keyhole mode ($T_{max} = T_{vap}$). However, the physical phenomena involved, including evaporation and plasma plume formation, high spatial and temporal temperature gradients, and non-equilibrium phase transformations, influence the optical conditions of the brightness of the emission of light from the molten pool, making, De Facto, the emissivity value not constant. Thus, what we propose here is a methodological procedure that allows the measurement of the effective emissivity of the surface, at the same time taking into consideration the consequence of physical phenomena and the conditions of the surface. Two procedures (Standard and Simplified) capable of providing the correct emissivity value in relation to the working parameters have been proposed. The results showed that the procedures are correct, fast, and easy to use.

Keywords: Laser welding; emissivity; thermography; IR camera calibration.

1. Introduction

Typically, the temperature of the object is one of the fundamental parameters of thermal processes [1,3,10], such as example, melting. As a consequence, it must be evaluated accurately. But this is not an easy task for several reasons. Primarily under laser processing, the temperatures reach high values with high-temperature gradients. A few metrological points are evident here. These include: a range of temperature that goes up to 2000 K and remarkable temperature gradients ($\sim 105 - 107$ K/m) both in the pool where melting is performed and the zone affected by heat; elevated rates of heating and cooling ($\sim 103 - 106$ K/s); flexible laser beam diameter in the plane of focus (ranging from 50 μm to 500 μm), a reflection of the laser beam, phenomena of the plume where the laser works, and emissivity of temperature dependence [4]. Compare to photoelectric detectors, thermal detectors such as thermocouples or semiconduction bolometers, which are much more susceptible to change in temperature on the sensor, possess a lower sensitivity and their reaction time is much slower. Photoelectric detectors can instead register

infinitesimal changes in the flow of thermal radiation. In this case, only a minimal part of the full flow of the heat released by the surface of a heated body could be recorded. Laser metalworking temperature measurements are typically executed with thermocouples, infrared cameras, and pyrometers [7]. In any case, the need to obtain temperature data that are extremely precise and with a high resolution in space and time is a remarkable task for experimenters, where temperatures, gradients, and rates of heating and cooling are severely extreme [8]. There are other crucial problems for the infrared camera in such an environment. The problem here is that the emissivity of the hot metal is both low and inconsistent in this environment, where the temperatures are deducted, and therefore apparent (or better relative), and thus not true (or better absolute). Infrared (IR) thermography is the use of an IR camera to measure the apparent temperature of an object derived from its emissivity [9]. Therefore, the measurement of temperature through infrared radiation necessitates knowing the value of the emissivity of the heated surface both in the whole spectrum of range

sensitivity and in the full space of the temperature used in the process. The surface emissivity usually depends on the:

- Material
- Surface quality (geometry, roughness, oxidation, etc.)
- IR Camera (wavelength and the direction of observation)
- Temperature
- physical phenomena : phase change, evaporation, plasma plume formation, etc.

Most of the existing literature, that employs thermography in the evaluation of the welding process, is grounded on unchanging values of emissivity. This is the consequence of insufficient knowledge of the modification of the emissivity in the material through the process of welding. Examples of this literature, that gauge thermal signature in the processes of welding through a method of thermography grounded in an unchanging value of emissivity, are Boillot et al., Chen and Feng and Woo et al. Others [11,12,13] have evaluated the emissivity as a function of temperature, not going beyond the melting temperature, thus neglecting the effects due to the phase change. Thus, most of the available data did not consider the effects of the physical phenomena on the emissivity value. For this purpose, some authors [3,7] have proposed an alternative method for the evaluation of emissivity during laser welding. The isotherms consistent with the melting point of aluminum (785 K) were assessed and then compared with the temperature distribution gauged in the zone of irradiation of the laser. Such data were then compared with the thickness of the melted zone. The use of the melting point isotherm allowed the calculation of the value of emissivity and the restoration of the temperature [4]. In this way, the emissivity is evaluated by considering the effects due to phase change and evaporation. However, the authors hypothesize that the value obtained is constant. The physical phenomena involved, including evaporation and plasma plume formation and in general, all those physical phenomena that influence the emissivity, mostly depend on the working parameters chosen as they determine the energy supplied during laser processing which in turn determines the temperature gradient. The temperature gradient determines the speed of phase transitions, evaporation rate, chemical reactions, microstructure and properties of the material, [2-3]. As is evident, that whenever the parameter values change, supply energy and the width of the melted zone change, and consequently the emissivity value changes [3,6]. This requires the need to carry out preliminary tests. The purpose of this work is to create a methodology that allows one to obtain an emissivity as a function of a w_{mz} and evaluate it without carrying out tests on the laser machine.

Once the material for a process by laser is chosen, the tests are made with the identical quality of the surface, and the IR camera is selected and placed, the emissivity will be the outcome of temperature and other associated physical phenomena. Furthermore, if the welding takes place in key-hole mode, and then in conditions where the maximum temperature reached is always the same ($T_{max} = T_{vap}$), the functional dependence of the emissivity can be reduced exclusively to the development of the physical phenomena involved. The evolution of the physical phenomena described largely depends on the working parameters (P - laser supplied power, v - welding speed, d - defocus), consequently, the emissivity was evaluated as a function of

these ε = f (d, P, v). It has also been noted that if the defocus value is fixed, the width of the melted zone depends on the working parameters P and v, thus obtaining the relation: $w_{mz}=f_d(P,v)$. In this way, it was possible to obtain a relationship between the emissivity (ε) and the width of the melted zone (w_{mz}) for a fixed defocus value.

$$\varepsilon_0 = f_0(w_{mz}) \tag{1}$$

$$\varepsilon_{-6} = f_{-6}(w_{mz}) \tag{2}$$

With this methodology it is possible to evaluate the emissivity as a function of width of the melted zone. The emissivity was then obtained by carrying out two types of tests by setting the defocus to two different values (d_0, d_{-6}) and varying the other two parameters P and v. After the tests, the experimental sets of (w_{mz}, ε) were fitted by the empirical model. Through interpolating procedure, the functions relating to the other defocus values have been obtained. The emissivity map (Figure 1), which establishes the relationship between the emissivity and the width of the melted zone is then obtained. Then, a FEM model, using COMSOL Multiphysics software, was created. The FEM model was validated by comparing the isotherm corresponding to the melting point ρ_y to the width of the melted zone (w_{mz}) derived from experimental tests.
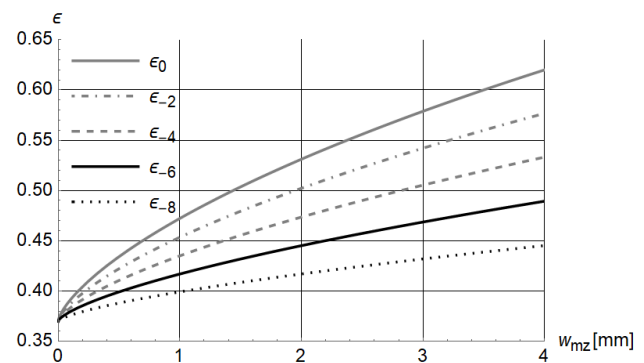

Figure 1. The emissivity map.

So, it is possible to evaluate the emissivity for different working parameters by first evaluating the isotherm corresponding to the melting point ρ_y, obtained through the FEM model. (Standard procedure).

To reduce times, and to obtain a faster and more practical procedure, the parameter map was obtained. The knowledge of the parameter map allowed a relationship between specific energy and the width of the melted zone, corresponding to a preselected value for the defocus. It was able to value the width of the melted zone $w_{mz} = w_{mz,i}(e_{LB})$ after fixed parameters and calculated the specific energy. From the emissivity map, the emissivity value is then obtained. (Simplified procedure).

2. Materials and Method

It was considered a base metal corresponding to the standard EN 45100 (AlSi5Cu3Mg – UNI EN 1676) aluminum with a thickness of 6 mm (Table 1). The rectangular section plates have been obtained from a single slab with surface roughness Ra = 1.4 μm.

Table 1. Nominal Chemical Composition (wt %) of Base Metals.

chemical components	%
Si	4.5÷6
Fe	0.5
Cu	2.6÷3.6
Mn	0.55
Mg	0.20÷0.45
Cr	/
Ni	0.1
Zn	0.1
Sn	0.05
Ti	0.2

For the purposes of this work, a Yb: YAG disk laser source supplied in fiber, operating in continuous wave emission, was considered (Table 2).

Table 2. Laser Welding System Technical Data.

Chemical Components	%
Maximum output power [kW]	4.0
Laser light wavelength λ [nm]	1030
Beam Parameter Product [nm x mrad]	8.0
Focal beam waist d [mm]	0.3
Rayleigh range [mm]	2.81
Focal length f [mm]	200
Maximum power density [kW/mm²]	56.6
Laser beam diameter at defocus 0 [mm]	0.3
Laser beam diameter at defocus -2 [mm]	0.44
Laser beam diameter at defocus -4 [mm]	0.71
Laser beam diameter at defocus -6 [mm]	1.01
Laser beam diameter at defocus -8 [mm]	1.32

An integrated 3-way power nozzle was attached to the laser head, which was moved by a 6-axis industrial robot with a dedicated controller. Argon was injected as a carrier gas at a flow rate of 30 L/min, and helium was coaxially blown to the laser beam at a flow rate of 10 L/min as a shielding gas on the melting bath (Figure 2).
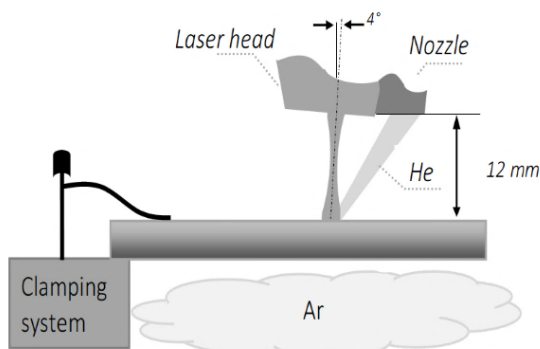

Figure 2. Schematic of the laser head with three-way feed nozzle; components not to scale.

A tilt angle of 4∘ was set for the laser head, in accordance with common practice for processing highly reflective metals [8] to prevent rear reflections from entering the optical train. The infrared (IR) camera (Optris PI 400, spectral wavelength λ=8 μm) was positioned at 0.5 m with a zenith angle of 90° and an azimuth angle of 90°, with respect to the work area, to detect the surface temperature range. An inclination of 45° has been assigned to the IR camera [9].

Therefore, the thermo-chamber mainly acquires emissions from the weld seam visible through the vapor plume. (Figure 3).
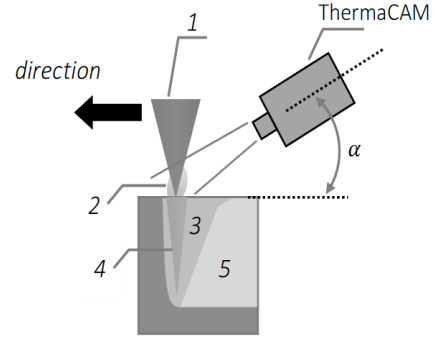

Figure 3. Configuration used for observation with a Optris PI 400 thermal camera. keyhole mode laser welding (1. laser beam, 2. plasma/vapor cloud, 3. molten metal. 4. keyhole. 5. solidified melt).

The calibration of the IR camera was performed by an M390S black body. Emissivity values are defined by Planck's law [24]

$$\frac{1}{T_v} = \frac{1}{T_b} + \frac{\lambda}{c_2} Log(\varepsilon) \tag{3}$$

with T_v - real temperature (K), T_b − brightness temperature (K), c_2 - constant = 14390 (μm K). To measure the geometric characteristics of laser welding, in particular the dimensions of the weld bead, it was using an optical microscope. The experimental sets of (w_{mz}, ε) were fitted, for a fixed defocus value, by the empirical model:

$$\varepsilon_{def,i}(w_{mz}) = 0.37 + Log\left(\frac{x^{0.7}}{C_{def,i}} + 1\right) \tag{4}$$

where $C_{def,i}$ are the best fit parameters (Table 3).

Table 3. Best Fit Parameters.

Emissivity Map		Parameter Map	
$C_{def,0}$	19.307	$C'_{def,0}$	11.107
$C_{def,-2}$	10.586	$C'_{def,-2}$	3.915
$C_{def,-4}$	13.755	$C'_{def,-4}$	1.477
$C_{def,-6}$	8.540	$C'_{def,-6}$	0.572
$C_{def,-8}$	31.534	$C'_{def,-8}$	0.285

For each test the specific energy supplied is evaluated as shown:

$$e_{LB} = \frac{P}{A} \cdot \frac{s}{v} \tag{5}$$

where P is a laser supplied power, v is a welding speed, s is the length of the weld (10 cm for all tests) and A=π·(d/2)² is a beam spot area. The experimental sets of (e_{LB}, w_{mz}) were fitted, for a fixed defocus value, by the empirical model:

$$w_{mz,i}(e_{LB}) = Log\left(\frac{x^{1.1}}{C'_{def,i}} + 1\right) \tag{6}$$

where $C'_{def,i}$ are the best fit parameters (Table 3).

3. Mathematical Formulation

For heat transfer and fluid flow modeling, conservation of energy Eq. (7) and mass Eq. (14), and momentum balance Eq. (13) are solved. The following assumptions are made in the model.

o Liquid metal is incompressible Newtonian under flow
o Gaussian heat source
o Boussinesq approximation is valid

$$\rho \cdot c_p^{eq} \frac{\partial T}{\partial t} + \rho \cdot c_p^{eq} u \cdot \nabla T = \nabla \cdot (k \nabla T) \qquad (7)$$

with ρ - local density (kg·m^{-3}), c_p^{eq} – local equivalent heat capacity (J·kg^{-1}K^{-1})), k – local thermal conductivity (W·m^{-1}K^{-1}), T – solved temperature (K) and t – time (s). Latent heat of fusion and evaporation are taken in account by means of equivalent enthalpy approach [14].

$$c_p^{eq} = c_p + D_m L_m + D_v L_v \qquad (8)$$

where c_p is heat capacity as function of temperature, L_m and L_v – latent heat of fusion and evaporation, and D_m and D_v are Gauss function normalized around melting and evaporation temperature T_m and T_v respectively:

$$D_i = \frac{e^{-\left(\frac{T - T_i}{\Delta T}\right)^2}}{\sqrt{\pi}\Delta T} \qquad (9)$$

where ΔT is smoothing interval of 50 K. The initial condition is given by Eq. (10),

$$T(x, y, z, t) = T_0 \qquad (10)$$

where the initial temperature T_0 is maintained at 293 K. The convective cooling and surface to ambient radiation boundary conditions were applied to the whole geometry. A heat source was introduced as a top surface Gaussian thermal source. Heat loss due to evaporation was modeled using a top surface vaporization heat flux [15]:

$$\dot{q}_{vap} = -\beta_r\, L_v \sqrt{\frac{M}{2\pi RT}} P_{sat} \qquad (11)$$

where β_r – the specific energy coefficient, L_v – local latent heat of vaporization (J·kg^{-1}), M – molar mass (kg·mol^{-1}), R – ideal gas constant (J·mol^{-1} K^{-1}), P_{sat} – saturated vapor pressure (Pa). The boundary conditions, heat flux and heat of vaporization, applied on the top, is expressed in Eq. (12)

$$k\frac{\partial T}{\partial z}\bigg|_{z=6} = -\dot{q}_{gauss} + \square \cdot (T(x, y, 0, t) - T_\infty) + \varepsilon \cdot \sigma \cdot (T^4(x, y, 0, t) - T_\infty^4) + \dot{q}_{vap} \qquad (12)$$

where $\dot{q}_{gauss}$ is the specific energy of the beam with a power P with a Gaussian function.

The heat transfer model was incorporated with the fluid flow Multiphysics to determine the deformation of the molten weld pool under various boundary conditions such as Marangoni convection, Buoyancy Darcy damping force and recoil pressure to predict the weld bead morphology. The equations of mass conservation Eq. (13) and momentum balance (Navier-Stokes, Eq. (14)) were used to govern the fluid flow in weld.

$$(\nabla \cdot u) = 0 \qquad (13)$$

$$\rho \frac{\partial u}{\partial t} + \rho(u \cdot \nabla)u = \nabla \cdot \left(-pI + \mu(\nabla u + (\nabla u)^T)\right) - \rho\left(1 - \beta(T - T_m)\right)g + F_D \qquad (14)$$

where, F_D is the Darcy force (N),

$$F_D = \rho \cdot g \cdot \alpha(T - T_m) \qquad (15)$$

g is the acceleration due gravity, α is the coefficient of thermal expansion (K^{-1}) and T_m is the melting temperature. It is found through Rayleigh's analysis that buoyancy force can make a big difference to the temperature profile of the pool via natural convection only when Rayleigh number exceeds 1100 in the pool. In a typical laser welding process, it is far less than 1100 due to small thickness of workpiece and thermal expansion coefficient [16]. Marangoni convection is a fluid flow due to the surface tension in the molten weld pool. It's assigned to the boundary on the top surface

$$-\mu\frac{\partial \mu}{\partial x} = \frac{\partial T}{\partial y} \cdot \frac{\partial \gamma}{\partial T} \qquad (16)$$

where μ is the dynamic viscosity (Pa·s) and γ is the temperature derivative of surface tension. At the top surface of the domain, the recoil pressure [17] was applied:

$$P_r = \left(\frac{1 + 0.02}{2}\right) P_{sat} \qquad (17)$$

with pressure of saturated vapor given as:

$$P_{sat} = P_0 \cdot exp\left(\frac{L_{vap} \cdot M}{R}\left(\frac{1}{T_{vap}} - \frac{1}{T}\right)\right) \qquad (18)$$

3.1 Numerical Modeling: Finite Element Method

The FEM model was built using COMSOL Multiphysics software. The model is created using heat transfer in fluids and laminar flow under phase change conditions. Multiphysics coupling is achieved by interrelating the equations that describe heat transfer and flow: the velocity field in the equation describing convection (heat flow) is obtained by solving the Navier-Stokes equations, which provide temperature as a function of position; in turn, temperature defines thermophysical properties. To build FEM model correctly, the following have been defined:

Model parameters: needed to build the numerical model such as the type of materials, sample size, wavelength, and work parameters: power, scan speed and spot radius (Table 2).

Materials' Properties: Since the proposed model considers the solid-liquid phase change, the properties at ambient temperature for the solid phase and at melting temperature for the liquid phase were used. Specific heat, thermal conductivity coefficient [18,22], and density [11,19] were then defined (Table 4). The absorption value was chosen for aluminum 0.16 [20,21]. The liquid-vapor phase transition was not considered.

Geometry and mesh modeling: One of the most important steps in FEM modeling is the definition of mesh geometry. The geometry of the model consists of a thin sheet. A 3-D solid block of (40 x 30 x 6) mm^3 was created. To verify that the calculated results are independent of the sample size, some simulations were carried out with the real dimensions of the specimen, and it was verified that the temperature profiles are identical. To ensure that the calculated results are grid-independent, several grid distributions have been tested.

Maximum temperature differences of the fields are less than 0.1 percent by doubling the mesh nodes. Two parts are meshed using tetrahedral geometry meshes. The minimum and maximum size of the element for the mesh is 0.1 and 0.2 mm for the block where one boundary condition has been applied and 0.2 and 0.3 mm for the other.

Table 4. Aluminum Thermophysical Properties.

	Phase State	
	Solid	Liquid
ρ [kg m^{-3}]	2600	2400
k [W m^{-1} K^{-1}]	150	90
μ [Pa s]	0.001	0.0007
L_m [J kg^{-1}]	$3.3 \cdot 10^5$	
L_v [J kg^{-1}]	$1.4 \cdot 10^7$	
c_p [J kg^{-1} K^{-1}]	Eq. (8)	
σ [N m^{-1}]	0.7	
T_m [K]	785	
T_{vap} [K]	2800	
M [kg mol^{-1}]	0.269	
R [J·mol^{-1} K^{-1}]	8.314	

Boundary conditions and initial conditions: The laser beam incident on the surface z = 6 mm was characterized by a second type boundary condition where the imposed flux is the heat source $\dot{q}_{gauss}$. In addition, the third type boundary condition on face z = 6 mm was considered. In the hypothesis of natural convection $\dot{q}_{conv}$, the model was given a constant thermal convection coefficient h = 10 [W m^{-2} K^{-1}] [21,23]. It was also considering radiative cooling $\dot{q}_{irr}$ a constant value was set $\varepsilon_{irr} = 0.15$ [12] for aluminum. Furthermore, the third type of boundary convective condition on all faces was considered (Figure 4).
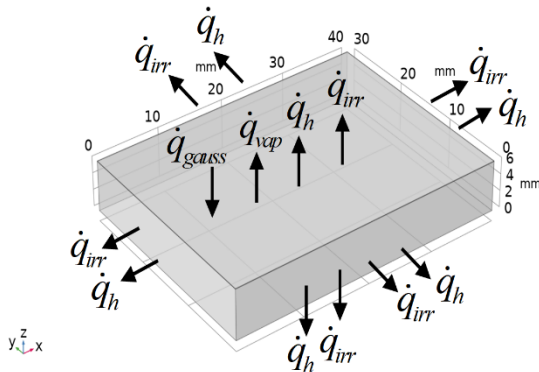

Figure 4. The schematization of the boundary conditions.

The ambient temperature and the initial temperature conditions of the plate are equal to 293 K. The liquid-vapor phase transition was not considered. On the other hand, the heat loss through evaporation was represented by top surface vaporization heat flux $\dot{q}_{vap}$ Eq. (11). The specific energy coefficient was introduced to consider the specific energy supplied during laser welding. The coefficients have been obtained considering that the specific energy supplied during laser welding depends mainly on the diameter of the laser beam. In particular, the specific energy increases as the diameter decreases. Since β_r and the supplied energy coefficients are directly proportional, because if the specific energy supplied increases, the energy lost by evaporation must increase, β_r and the diameter are inversely proportional (Table 5) At the top surface of the domain, the recoil pressure

was applied P_r Eq. (17). Finally, Marangoni effect was considered the surface tension coefficient (σ) at the melting temperature T_m was taken into consideration [19].

Table 5. The Specific Energy Coefficient.

Defocus	Diameter d [mm]	1/d	βr - min normalization
def_0	0.3	3.33	4.4
def_{-2}	0.44	2.27	3
def_{-4}	0.71	1.41	1.9
def_{-6}	1.01	0.99	1.3
def_{-8}	1.32	0.76	1

Laser beam modeling: We assume that in the z-direction the heat source is concentrated at a level immediately below the upper surface (z = 6 mm). The irradiation of the beam gradually decreases at the edges (Figure 5).
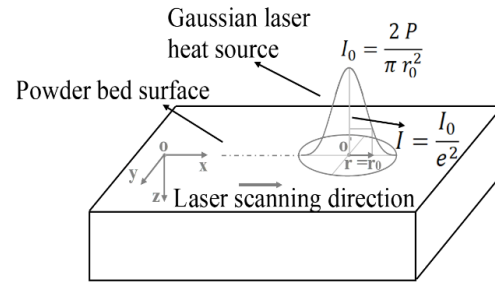

Figure 5. Sketch of the workpiece and coordinate system.

To define beam width for Gaussian beams Eq. (19) was used a $1/e^2$ method.

$$\dot{q}_{gauss}(x,y) = \frac{2 \cdot P}{\pi \cdot r_0^2} Exp\left(-\frac{2 \cdot ((x-x_0)^2 + (y-y_0)^2)}{r_0^2}\right) \qquad (19)$$

The width of the beam is calculated by measuring the distance between the two points where the intensity is $1/e^2$ of the peak value (Figure 6). So only about 86.5 % of the laser power is contained within the $1/e^2$ width (Eq. (20), Table 6).

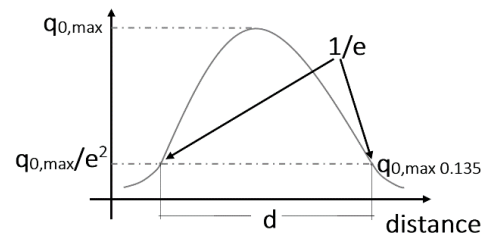$$\int_{x=-\sigma}^{\sigma} \int_{y=-\sigma}^{\sigma} \dot{q}_{gauss}(x,y) \cdot dxdy = 86.5\%P \qquad (20)$$

Figure 6. Gauss laser beam modelling.

4. Result and Discussion
4.1 Experimental Tests

Two types of tests were carried out at different defocus values as shown in Table 6. A rectangular section plate of sizes (L_x=100 x L_y=50 x L_z=6 mm) was used.

Each test was analyzed under an electron microscope which made it possible to obtain an image of the trace in TIF format (Figure 7).

The traces were divided into 17 sections at 4 mm intervals. For each section the size of the trace was evaluated (Table 7).

Table 6. Welding System Technical Data.

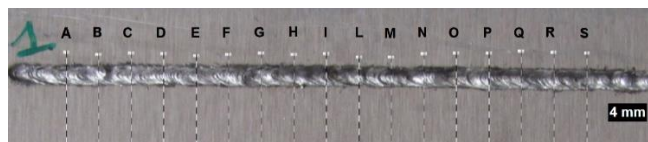|	Power P[W]	Welding speed v [mm s^{-1}]	Defocus def [mm]	Beam Diameter d [mm]
1AL	2500	50	0	0.30
2AL	3000	50	0	0.30
3AL	3000	35	0	0.30
5AL	3500	50	-6	1.01
8AL	3750	40	-6	1.01
9AL	4000	40	-6	1.01

Figure 7. Electronic microscope image: Test 1AL weld track.

Table 7. Test 1AL Width of the Melted Zone Sections.

Sez.	s[mm]	Sez.	s[mm]
a	2.26	m	2.57
b	2.34	n	2.49
c	2.34	o	2.44
d	2.16	p	2.57
e	2.34	q	2.39
f	2.55	r	2.39
g	2.34	s	2.39
h	2.49	Mean	2.40
i	2.34	Dev.St	0.11
l	2.31		

Then, mean values and standard deviations are calculated (Table 8).

Table 8. Mean Value of a Width of the Melted Zone.

Test	Width of the melted zone w_{mz}[mm]	Dev. st
1Al	2.40	0.11
2Al	2.58	0.15
3Al	2.88	0.15
5Al	2.87	0.10
8Al	3.18	0.13
9Al	3.40	0.08

These results will be used to validate the numerical model. For this purpose, the isotherms corresponding to the melting point (ρ_y) were calculated through the finite element method. The calculated ρ_y data were compared with the width of the melted zone (w_{mz}).

4.2 FEM Results
The simulation process allowed us to extrapolate the values corresponding to the fusion isotherm (785 K) on the plane at z =6 mm.
The data were fitted using an ellipsoidal model, Eq. (21)

$$\begin{cases} x(r) = X_0 + a \cdot cos\,\theta_r \\ y(r) = Y_0 + b \cdot sin\,\theta_r \\ \quad 0 \le \theta_r \le 2 \cdot \pi \end{cases} \qquad (21)$$

with a - sub axis (radius) of the X axis of the non-tilt ellipse, b - sub axis (radius) of the Y axis of the non-tilt ellipse, X_0 - center at the X axis of the non-tilt ellipse, Y_0 center at the Y axis of the non-tilt ellipse, ρ_x - size of the long axis of the

ellipse, ρ_y - size of the short axis of the ellipse, φ - orientation in radians of the ellipse (tilt). In this way, it was possible to quickly obtain the value of the diameter corresponding to the melting point (ρ_y) (Table 9, Figure 9).
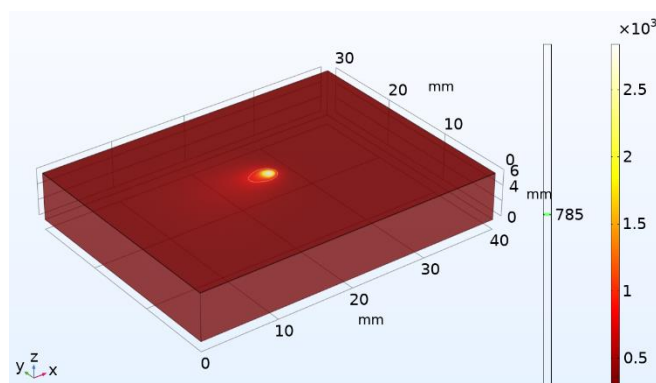

Figure 8. FEM Test 1AL, ρ_y isotherm at T=785K.

Table 9. FEM Fit Parameter.

|	1AL.	2AL	3AL	5AL	8AL	9AL	4AL	6AL
a	1.772	1.874	1.924	2.473	2.485	2.513	1.897	2.286
b	1.236	1.287	1.350	1.532	1.649	1.659	1.293	1.458
φ	-0.006	-0.007	0.025	-0.010	0.005	0.003	-0.008	-0.016
X_0	19.310	19.253	15.79	19.006	16.813	16.83	19.29	19.19
Y_0	14.855	14.845	15.387	14.779	15.074	15.03	14.81	14.67
ρ_x	3.544	3.748	3.849	4.946	4.971	5.026	3.795	4.573
ρ_y	2.473	2.574	2.719	3.045	3.299	3.318	2.586	2.917
Err %	0.225	0.26	0.268	0.402	0.684	0.109	0.211	0.107
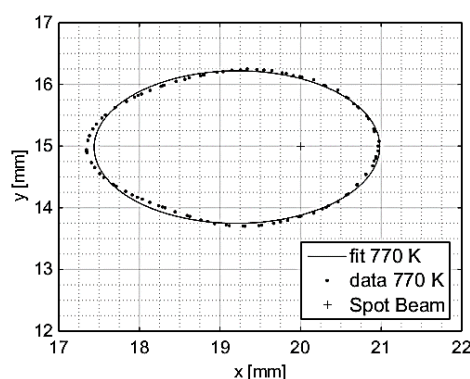
Figure 9. 1AL numerical data fit time = 0.2 s

As shown in Table 10,

Table 10. Isotherm Corresponding to the Melting Point Compared with the Width of the Melted Zone.

	P[W]	v [mm s^{-1}]	def [mm]	w_{mz}	ρ_y	err %
1AL	2500	50	0	2.40	2.477	3.02
2AL	3000	50	0	2.58	2.575	0.20
3AL	3000	35	0	2.88	2.720	5.75
5AL	3500	50	-6	2.87	3.045	5.92
8AL	3750	40	-6	3.18	3.299	3.67
9AL	4000	40	-6	3.40	3.318	2.44
4AL	3000	50	-4	2.60	2.586	0.50
6AL	2500	50	-8	2.87	2.917	1.63

fixed beam diameter and scan speed, as the power delivered by the laser increases, the extension of the diameter corresponding to the melting temperature increase (Tests 1AL and 2AL). The diameter ρ_y also increases with decreasing speed. For each test, the percentage error

between the isotherms corresponding to the melting point (ρ_y numerically evaluated) and the extension of the melted zone (w_{mz}, obtained through experimental tests) was evaluated. As shown in Table 10, the error for all types of test results is less than 6%. Thus, the constructed FEM model can provide a useful approximation to reality with a low average error. Then two further tests with defocus values def_{-4} def_{-6} were carried out, to verify the goodness of the FEM model (Table 11).

Table 11. Test Coefficients and Parameters.

P[W]	v[mm·s^{-1}]	def[mm]	d[mm]
3000	50	-4	0.71
3500	50	-8	1.32

It was compared the isotherm corresponding to the melting point to the width of the melted zone (Table 10). Also, in this case, the error is less than 6%.

4.3 Method of Brightness Temperature Definition and Emissivity Evaluation: The Emissivity Map

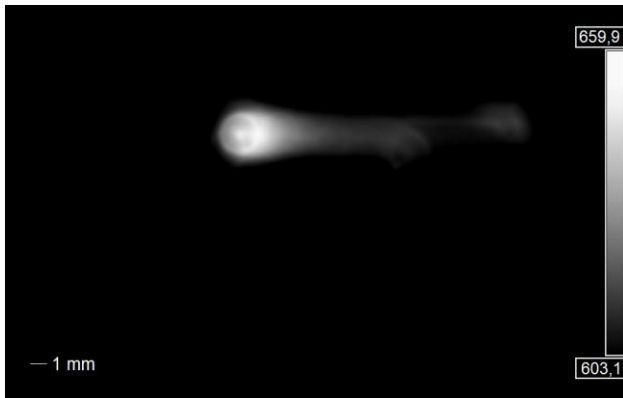The thermal image of cladding zone registered by IR camera is presented in Figure 10.

Figure 10. False-color: infrared image of melt pool registered by IR camera optris in 8 μm spectral wavelength, Test 1AL

The laser beam's maximum energy density flux has a pseudo-Gaussian form, which raises the temperature at the beam axis. The periphery portion of the molten pool, where oxides and other nonmetallic inclusions are typically concentrated   by thermocapillary convection and in the nearby solid phase sections, correlates to the ring-shaped zone with strong thermal emission. It is possible to define the emissivity value using Planck's law [24] at a spectral value λ=8 μm Eq. (3), assuming that the value of temperature stabilization at solidification corresponds to the known melting point of AL, which is equal to 785 K under equilibrium conditions. The comparison of the width of the molten zone obtained by irradiating the laser beam of the surface aluminum and the IR camera signal value is presented in Table 12.

A different type of palette (integrated in the Optris PI connect program) was used to display the images in such a way as to have well defined the different isotherms (Figure 11).

For each test 8 frames were evaluated (1 every 1 s). The obtained mean value was used to calculate the emissivity Table 13.

Table 12. Mean Brightness Temperature and Emissivity, λ=8 μm.

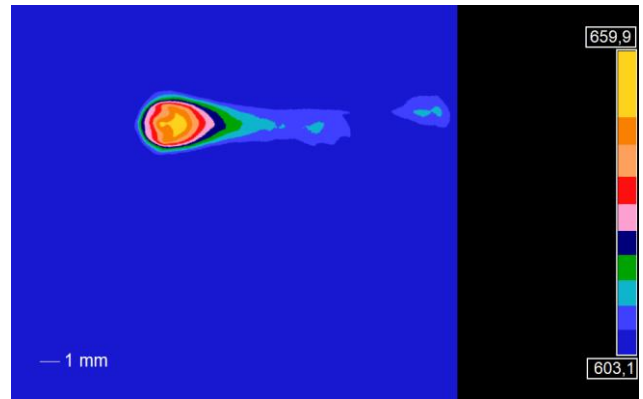|	w_{mz}[mm]	Brightness temperature T_b [K]	Empirical ε
1AL	2.40	623	0.550
2AL	2.58	635	0.581
3AL	2.88	641	0.597
5AL	2.87	587	0.461
8AL	3.18	596	0.486
9AL	3.40	600	0.493
4AL	2.60	609	0.515
6AL	2.87	577	0.437

Figure 11. Rainbow-colors: infrared image of melt pool registered by IR camera optris in 8 μm spectral wavelength, Test 1AL frame 4.

Table 13. Brightness Temperature, Frame 1-8.

Frame	1AL	5AL
1	615	579
2	630	577
3	635	594
4	620	597
5	621	598
6	617	579
7	632	581
8	614	590
$\bar{T}$ [K]	623	586.9

The experimental sets of (w_{mz}, ε) were fitted, for a fixed defocus value, by the empirical model, Eq. (4).

Coordinate (0, ε_0) has been identified as a reference. In fact, the condition $w_{mz} = 0$ represents the case in which the temperature reached is lower than the melting point so that melting does not occur. The value of $\varepsilon_0 = 0.37$ was chosen which corresponds to the emissivity at a temperature of 785 K [25]. The functions relating to the other defocus values have been obtained through interpolating procedure (Table 3, Figure 12).
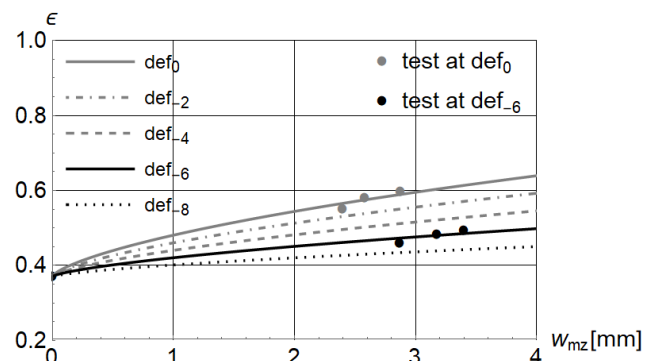

Figure 12. The emissivity map. Functions ε (w_{mz}) at different defocus values.

In this way, the emissivity map, which coupled with the FEM model allows us to obtain a procedure capable of providing the emissivity value without carrying out tests on the laser machine, was obtained. A relative error between the emissivity value evaluated experimentally and that obtained from the emissivity map using experimental w_{mz} was evaluated (Table 14).

Table 14. Experimental Emissivity vs Emissivity Obtained from the Emissivity Map - Input w_{mz} .

	w_{mz} [mm]	Empirical ε	Emissivity map $\varepsilon_{def,i}(w_{mz})$	Err %
1AL	2.40	0.550	0.551	0.2
2AL	2.58	0.581	0.560	3.7
3AL	2.88	0.597	0.574	4.0
5AL	2.87	0.461	0.465	1.0
8AL	3.18	0.486	0.472	2.8
9AL	3.40	0.493	0.478	3.2
4AL	2.60	0.515	0.503	2.3
6AL	2.87	0.437	0.434	0.7

As shown, the error is ≤ 4 %. So, through the parameter map, it is possible to evaluate the correct emissivity value, to be attributed to the IR camera in relation to the working parameters, knowing the width of the melted zone. Since, as previously seen, $w_{mz} = \rho_y$ with less than a maximum error of 6 % to the diameter corresponding to the fusion isotherm, it was possible to use the ρ_y value, obtained from the FEM model as input data for the evaluation of the emissivity with the use of the emissivity map. For 4AL and 6AL tests, respectively to defocus def$_{-4}$ and def$_{-8}$, the emissivity was evaluated starting from the value of the width of the melting zone w_{mz}, experimentally evaluated, and compared with temperature distribution measured in the laser irradiation zone (Table 14). Also, in this case, a relative error between the experimentally emissivity value and that obtained from the emissivity map using experimental w_{mz} , was evaluated . Then, through the FEM model, the width of the melted zone was evaluated. The emissivity was obtained through the emissivity map $\varepsilon (\rho_y)$, (Figure 13, Table 15).
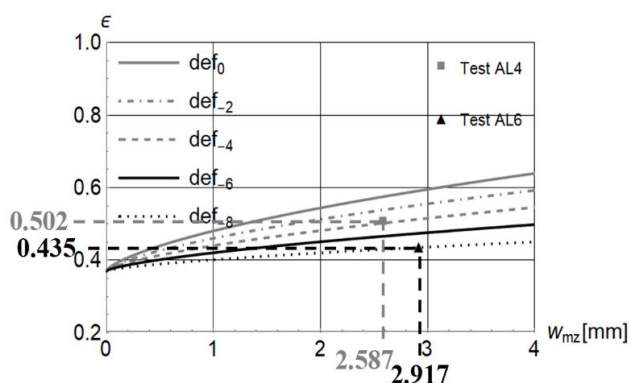

Figure 13. $\varepsilon (\rho_y)$ value obtained through the emissivity map. Tests 4AL,6AL.

It has been observed that the use of the methodology involves an error ≤ 5% .

We can sum up, what will be called the standard procedure, as follows (Figure 14):

- o *Known the working parameters, through the FEM model the value $w_{mz} = \rho_y$ was obtained.*

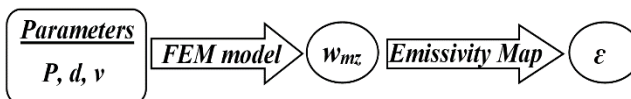- o *Using the emissivity map, the value $\varepsilon(\rho_y)$ was obtained.*

Figure 14. Standard procedure.

Table 15. Experimental Emissivity vs Emissivity Obtained from the Emissivity Map - Input ρ_y - Standard Procedure.

	ρ_y [mm]	Empirical ε	Emissivity map $\varepsilon_{def,i}(\rho_y)$	Err %
1AL	2.477	0.550	0.569	3.5
2AL	2.575	0.581	0.574	1.1
3AL	2.720	0.597	0.582	2.6
5AL	3.045	0.461	0.476	3.4
8AL	3.299	0.486	0.482	0.7
9AL	3.318	0.493	0.484	2.0
4AL	2.587	0.503	0.502	0.1
6AL	2.917	0.434	0.435	0.2

4.4 Method of Specific Energy: The Parameter Map

Through the FEM model, which allows us to evaluate the width of the melting zone for fixed working parameters, and next through the emissivity map, it was possible to obtain the emissivity value to be attributed to the IR camera for correct calibration. In this way, it is possible to predict the emissivity, for fixed working parameters, without having to carry out tests on the laser machine, but simply by obtaining the ρ_y value from the FEM model and then using the emissivity map. Since the computational times are not short (about 4 hours), a streamlined procedure has been implemented. For each test, the specific energy supplied is evaluated (Eq. (5) – Table 16):

Table 16. Specific Energy.

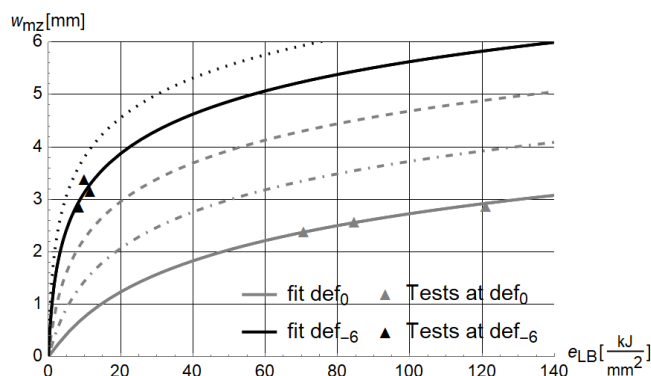|	P [W]	v [mm·s-1]	d [mm]	A [mm²]	e_{LB} [kJ mm⁻²]	w_{mz} [mm]
1AL	2500	50	0.30	0.070	70.735	2.40
2AL	3000	50	0.30	0.070	84.882	2.58
3AL	3000	35	0.30	0.070	121.261	2.88
5AL	3500	50	1.01	0.801	8.730	2.87
8AL	3750	40	1.01	0.801	11.705	3.18
9AL	4000	40	1.01	0.801	9.985	3.40
4AL	3000	50	0.71	0.395	15.154	2.60
6AL	3500	50	1.32	1.369	5.115	2.87

Figure 15. The parameter map. Functions $w_{mz}(eLB)$ at different defocus values.

The experimental sets of (e_{LB}, w_{mz}) were fitted, for a fixed defocus value, by the empirical model, (Table 3, Eq. (6)). In

this case, the point (0,0) corresponding to the condition in which $e_{LB} = 0$ consequently $w_{mz} = 0$, has been identified as a reference. The parameter map (Figure 15), which allows us to predict the width of the melted zone as a function of the working parameters, thus was obtained.

A relative error between the width of the melted zone and $w_{mz,i}(e_{LB})$ obtained from the parameter map, was evaluated (Table 17).

Table 17. Width of the Melted Zone w_{mz} vs $w_{mz,i}(e_{LB})$ Obtained from the Emissivity Map.

	w_{mz} [mm]	e_{LB} [kJ mm⁻²]	Parameter Map $w_{mz,i}(e_{LB})$ [mm]	w_{mz} Err %
1AL	2.40	70.735	2.37	1.1
2AL	2.58	84.882	2.55	0.9
3AL	2.88	121.261	2.92	1.6
5AL	2.87	8.730	2.99	4.2
8AL	3.18	11.705	3.30	3.7
9AL	3.40	9.985	3.16	7
4AL	2.60	15.154	2.67	2.6
6AL	2.87	5.115	3.02	5.1

The methodology relating to the 4AL and 6AL tests was used. After setting the parameters, the specific energy was evaluated (Table 16).

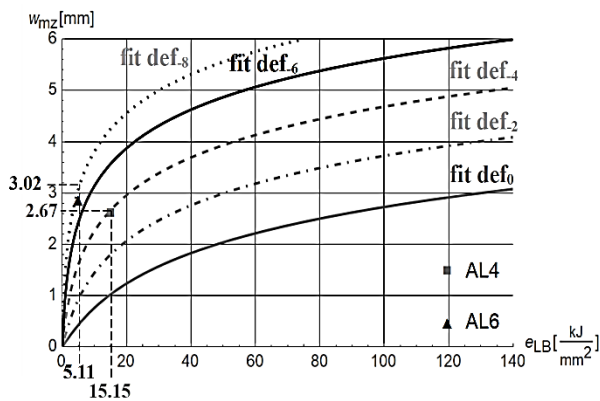The $w_{mz,i}(e_{LB})$ was evaluated using the parameter map (Figure 16),

Figure 16. Width of the melted zone obtained through the parameter map. Tests 4AL,6AL.

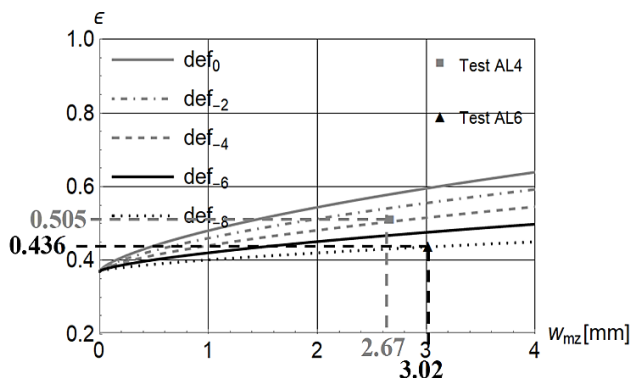through the emissivity map (Figure 17) the $\varepsilon(w_{mz,i}(e_{LB}))$ was obtained.

Figure 17. $w_{mz}(e_{LB})$ obtained through the emissivity map. Tests 4AL,6AL.

The results showed that it is possible to approximate the width of the melted zone w_{mz} with the value $w_{mz,i}(e_{LB})$

obtained from the parameter map with an average error equal to 3.3 % and a max error of 7 % (Table 17). The error between the emissivity evaluated empirically and that obtained from the emissivity map using the $w_{mz,i}(e_{LB})$ value obtained from the parameter map is small. The results showed an average error of 1.5 % with a maximum of 3.2 % (Table 18).

Table 18. Empirical Emissivity vs Emissivity Obtained from the Emissivity Map - Input $w_{mz}(e_{LB})$ - Simplified Procedure.

	Parameter Map $w_{mz,i}(e_{LB})$ [mm]	Emissivity Map $\varepsilon (w_{mz}(e_{LB}))$ [mm]	Empirical ε	ε Err %
1AL	2.37	0.564	0.550	2.6
2AL	2.55	0.574	0.581	1.2
3AL	2.92	0.592	0.597	0.9
5AL	2.99	0.475	0.461	3.2
8AL	3.30	0.482	0.486	0.6
9AL	3.16	0.480	0.493	2.7
4AL	2.67	0.505	0.503	0.4
6AL	3.02	0.436	0.434	0.5

A simplified procedure, that allows us to evaluate the emissivity value using the $w_{mz,i}(e_{LB})$ value obtained from the parameter map as input for the emissivity map, was obtained. (Figure 18). We can recap it as follows:
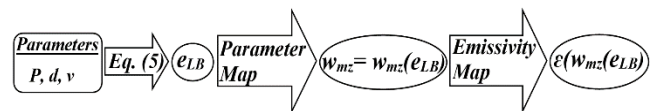

Figure 18. Simplified procedure.

o   *Known the working parameters, through the Eq. (5) the value of specific energy e_{LB} is calculated.*

o   *Using the parameter map, the value $w_{mz} = w_{mz,i}(e_{LB})$ was obtained.*

o   *Using the emissivity map, the value $\varepsilon(w_{mz}(e_{LB}))$ was obtained.*

The simplified procedure was faster and leaner than the standard one. In fact, the simplified procedure foresees to use as input for the emissivity map the value $w_{mz,i}(e_{LB})$ obtained through Eq. (5) and parameter map. This process is much simpler and faster than using the FEM model.

5. Conclusion

To use an infrared camera to measure the temperature during laser welding, it is necessary to know the emissivity. For this type of processing, the emissivity value is obtained by comparing the width of the melted zone with the temperature distribution measured in the laser irradiation zone. The apparent temperature value corresponding to the width of the molten zone is obtained. Finally, using Planck's law, the emissivity value may be calculated.

Since the emissivity is not constant, every time the working parameters are set, it will be necessary to carry out a preliminary test. This results in a waste of time and materials. The methodology is not very workable and laborious to use. In this work, two procedures, that can overcome the limits seen, have been proposed. Both procedures (Standard – Simplified) require the use of the emissivity map. The knowledge of the emissivity map allowed a relationship between the width of the melted zone

and the emissivity, corresponding to a preselected value for the defocus. This allowed it to value the emissivity after setting parameters and measuring the width of the melted zone ($w_{mz} = \rho_y$) by FEM model (Standard procedure). The time needed to obtain the emissivity value corresponds to the time needed to obtain the value ρ_y using the FEM model (about 4 hours). To reduce the time required, and thereby obtain a more practical procedure, a parameter map was calculated. The knowledge of the parameter map allowed a relationship between specific energy and the width of the melted zone, corresponding to a preselected value for the defocus. It was able to value the width of the melted zone $w_{mz} = w_{mz,i}(e_{LB})$ after fixed parameters and calculated the specific energy. The $\varepsilon(w_{mz,i}(e_{LB}))$ value is obtained through the emissivity map. In this way, a more streamlined and rapid procedure was obtained (Simplified procedure), for which calculation times are, de facto, zero. In this way, after setting the working parameters, it is possible to get an instant evaluation of the emissivity without having to perform preliminary tests. Both methods are quick and allow us to determine the emissivity value considering the physical phenomena involved and the conditions of the surface.

Nomenclature

def	Focal beam waist	mm
r_0	Radius beam	mm
v	Welding speed	mm s^{-1}
w_{mz}	Width of the melted zone	mm
ρ_y	Isotherm corresponding to the melting point	mm
P	Power	W
L_x	Slab length	mm
L_y	Slab width	mm
L_z	Slab depth	mm
C_{abs}	Absorption coefficient	/
k	Thermal conductivity	Wm^{-1}K^{-1}
h	Convective heat transfer coefficient	Wm^{-2}K^{-1}
ε_{irr}	Aluminum emissivity constant value for a FEM model	/
ρ	Mass density	Kg m^{-3}
c_p	Specific heat.	J kg^{-1} K^{-1}
μ	Dynamic Viscosity	Pa s
σ	Surface tension coefficient	N m^{-1}
L_m	Latent heat of fusion	J kg^{-1}
L_v	Latent heat of vaporization	J kg^{-1}
T_m	Melting temperature	K
T_{vap}	Evaporation temperature	K
M	Molar mass	kg mol^{-1}
R	Ideal gas constant	J·mol^{-1} K^{-1}

References:

[1] A. Mosavia, F. Salehib, L. Nadaie, S. Karolyc, N. E. Gorjid, "Modeling the temperature distribution during laser hardening process", *Results in Physics Volume 16*, March 2020, 102883. https://doi.org/10.1016/j.rinp.2019.102883.

[2] H.G. Woo, H. S. Cho, "Three-dimensional temperature distribution in laser surface hardening processes", *Proceedings of the Institution of Mechanical Engineers Part B Journal of Engineering Manufacture* 213(7):695-712. DOI:10.1243/0954405991517128.

[3] I. Smurv and M. Doubenskaia, "Temperature Monitoring by Optical Methods in Laser Processing", *Chapter 9 in the Book ''Laser-Assisted Fabrication of Materials''. Springer Series in Materials Science, Vol 161*, J. Dutta Majumdar and I. Manna, Ed., Springer, Berlin, 2013, p 373-422. DOI:10.1007/978-3-642-28359-8_9.

[4] M. Doubenskaia, M. Pavlov, S. Grigoriev, I. Smurov, "Definition of brightness temperature and restoration of true temperature in laser cladding using infrared camera", April 2013, *Surface and Coatings Technology 220:244-247*. DOI: 10.1016/j.surfcoat.2012.10.044.

[5] M. Doubenskaia, I. Zhirnov, V. Teleshevskiy, Ph. Bertrand, I. Smurov, "Determination of True Temperature in Selective Laser Melting of Metal Powder Using Infrared Camera" November 2015 *Materials Science Forum 834:93-102*. DOI:10.4028/www.scientific.net/MSF.834.93.

[6] Z. Lanc, B. Strbac, M. Zeljkovic, A Zivkovic, M Hadzistevic, "Emissivity of aluminium alloy using infrared thermography technique", June 2018, *Materials and Technologies 52(3)*. DOI:10.17222/mit.2017.152.

[7] A. P Tadamalle, "Review of Real-Time Temperature Measurement for Process Monitoring of Laser Conduction Welding", *Eng. Sci. Technol. An Int. J. 2(5), 946–950 (2012)*.

[8] S. M. Thompson, L. Bian, N. Shamsaei, A. Yadollahi, "An overview of Direct Laser Deposition for additive manufacturing, Part I: Transport phenomena, modeling and diagnostics", *Addit. Manuf. 8, 36–62, Elsevier B.V. (2015).* https://doi.org/10.1016/j.addma.2015.07.001.

[9] T. Staudt, E. Eschner, M. Schmidt, "Temperature determination in laser welding based upon a hyperspectral imaging technique", *CIRP Annals Volume 68, Issue 1, 2019, Pages 225-228.* https://doi.org/10.1016/j.cirp.2019.04.117.

[10] M. Miccio, R. Pierri, G. Cuccurullo, A. Metallo, P. Brachi, "Process intensification of tomato residues drying by microwave heating: experiments and simulation", *August 2020 Chemical Engineering and Processing 156:108082. DOI: 10.1016/j.cep.2020.108082.*

[11] I. Mudawar, "Emissivity characteristics of roughened aluminum alloy surfaces and assessment of multispectral radiation thermometry (MRT) emissivity models", *International Journal of Heat and Mass Transfer · August 2004.* DOI: 10.1016/j.ijheatmasstransfer.2004.04.025.

[12] I. Mudawar, "Experimental Investigation of Emissivity of Aluminum Alloys and Temperature Determination Using Multispectral Radiation Thermometry (MRT) Algorithms", *Journal of Materials Engineering and Performance · January 2002.* DOI: 10.1361/105994902770343818.

[13] Z. Lanc, B. Strbac, M. Zeljkovic, A. Zivkovic, M. Hadzistevic, "Emissivity of aluminium alloy using infrared thermography technique", *June 2018 Materials and Technologies.* doi:10.17222/mit.2017.152.

[14] C. Bonacina, G. Comini, A. Fassano, M. Primicerio, "Numerical solutions of phase change problems", *International Journal of Heat Mass Transfer, 16, 1825-1832 (1973)]*.

[15] C. J. Knight, "Theoretical modeling of rapid surface vaporization with back pressure", *American Institute of Aeronautics and Astronautics Journal, 17:5, 19–523 (1979).*

[16] M. Edstorp, "Weld Pool Simulations", in *Department of Mathematical Sciences (2008), Chalmers University of Technology and University of Gothenburg.* ISSN 1652-9715

[17] R. Fabbro, K. Chouf," "Dynamical description of the keyhole in deep penetration laser welding*", Journal of Laser Applications,12:4,142-148- (2000).* https://doi.org/10.2351/1.521924.

[18] K. Narender, A. Sowbhagya M. Rao, K. Gopal K. Rao, N. Gopi Krishna, "Temperature Dependence of Density and Thermal Expansion of Wrought Aluminum Alloys 7041, 7075 and 7095 by Gamma Ray Attenuation Method", *Journal of Modern Physics 4(03):331-336; January 2013* DOI:10.4236/jmp.2013.43045.

[19] M. Leitner, T. Leitner, A. Schmon, K. Aziz, G. Pottlacher, "Thermophysical Properties of Liquid Aluminum *(2017)", Metallurgical and Materials Transactions A volume 48, pages3036–304.* DOI: 10.1007/s11661-017-4053-6

[20] R. Paschotta, Encyclopedia of Laser Physics and Technology, *"Wiley-VCH: Berlin, Germany, Vch Pub; 2° edition (22 October 2008)".* ISBN-10: 9783527408283.

[21] K. Suresh Kumar, T. Sparks, F. Liou, "Parameter determination and experimental validation of a wire feed Additive Manufacturing model", *In Proceedings of the 29th Annual International Solid Freeform Fabrication Symposium; An Additive Manufacturing Conference, Austin, TX,USA,pg.13–15;August-2015;URI.* https://hdl.handle.net/2152/89407.

[22] I. Bunaziv, Odd M. Akselsen, X. Ren, B. Nyhus and M. Eriksson, "Laser Beam and Laser-Arc Hybrid Welding of Aluminium Alloys", *Metals 2021, 11(8), 1150.* https://doi.org/10.3390/met11081150.

[23] J. Heigel, P. Michaleris, E. Reutzel, "Thermo-mechanical model development and validation of directed energy deposition additive manufacturing of Ti-6Al-4V", *Additive Manufacturing Volume 5, January 2015. Pages 9-19.* https://doi.org/10.1016/j.addma.2014.10.003.

[24] I. Smurov, M. Doubenskaia, "Laser-Assisted Fabrication of Materials", *in Majumdar J. D. and Manna I. (eds.), (Springer Series in Materials Science 161, Springer-Verlag Berlin Heidelberg, 2013, pp. 373-422.)* DOI:10.1007/978-3-642-28359-8.

[25] E. Filep, D. N. Kutasi, L. Kenéz, "Method for Emissivity Estimation of Metals*", Acta Materialia Transylvanica, 1/1, 2018 pg. 31-36.* https://doi.org/10.2478/amt-2018-0010.

Research Article

Thermodynamic and Thermophysical Properties of Air as a Mixture by Using Schreiber-Pitzer EoS

O. Akdemir[1*] ⬤ᴰ, M. T. Çoban[2] ⬤ᴰ,

[1,2]Ege University, Faculty of Engineering, Department of Mechanical Engineering, Bornova, Izmir, Turkey.
E-mails: [1*]ozay.akdemir@ege.edu.tr, [2]turhan_coban@yahoo.com

Abstract

Air is one of the most important substances used in industrial and technological applications. Applications of air require a consistent set of reliable data on its thermodynamic and thermophysical properties. Over the last few decades, researchers have developed a number of empirical and theoretical models for the correlation and prediction of the thermodynamic and thermophysical properties of pure fluids and mixtures. The ideal gas Equation of State (EoS) is used in gas thermodynamic property calculations extensively, but in applications with higher pressure zones, the error levels are increasing. For most applications, an equation of state with better accuracy of thermodynamic properties will be required for extreme cases. In this study, Schreiber-Pitzer EoS is considered for better accuracy of the thermodynamic properties for air mixture. A set of computer programs were developed in java language to calculate the thermodynamic and thermophysical properties of air as a mixture of Nitrogen, Oxygen and Argon. The Schreiber-Pitzer EoS results are compared with Peng-Robinson EoS, Redlich-Kwong EoS, Van der Waals EoS, and ideal gas EoS utilizing cubic spline curve fitting for c_p values. The thermodynamic and thermophysical property results and percentages of differences are calculated. The percentages of differences are increasing with increasing pressure and decreasing temperature.

Keywords: Schreiber-Pitzer EoS; thermodynamic properties of air; thermophysical properties of air; cubic spline.

1. Introduction

Accurate knowledge of the thermodynamic properties of gases and mixtures is needed for efficient design and operating processes. A variety of equations of state are available in the literature. The simplest and best known equation of state for substances in the gas phase is the ideal gas EoS, but its range of applicability is limited. The first cubic equation of state was proposed by J. D. Van der Waals in 1873 [1,2]. Van der Waals intended to improve the ideal gas EoS by including two of the effects not considered in the ideal gas model: the intermolecular attraction forces and the volume occupied by the molecules themselves. Redlich Kwong EoS, which is a considerably more accurate cubic equation than Van der Waals, was proposed in 1949 [3]. Cubic equations of state are rather simple and easy to extend to new components because only a few substance specific parameters are needed. They are accurate enough for high pressure applications. The Peng-Robinson EoS, which was suggested by Ding-Yu Peng and Donald B. Robinson in 1976, achieves simple and accurate predictions [4,5]. Peng-Robinson EoS has been widely used in thermodynamic calculations in industrial and scientific studies since 1976 [6]. Some of the researchers discussed the Peng-Robinson EoS in depth [7,8]. Zabaloy and Vera in 1998 compared Peng-Robinson EoS with other equations of state. They found, that Peng-Robinson EoS was clearly superior to the other forms considered in their study [9]. Valderrama gave

general recommendations for using the Peng-Robinson EoS for reliable application [10].

Schreiber-Pitzer EoS utilizes Pitzer's acentric factor, which is a modified form of Benedict-Webb-Rubin EoS [11]. It is basically a quadratic curve fitting equation to reference fluids by using Pitzer's acentric factor as a variable. A rich list of curve fitting reference fluids, including hydrocarbons and other gases, is used to obtain curve fitting coefficients of the EoS. In this study, specific heat values are added into the program as cubic spline curve fitting values. In order to create actual data for specific heat data, it is assumed that air is a mixture of Nitrogen, Oxygen and Argon. By getting specific heat and critical properties of these gases, pseudocritical properties of air are calculated and used as input parameters to Schreiber-Pitzer EoS. The Schreiber-Pitzer EoS results are compared with Peng-Robinson EoS, Redlich-Kwong EoS, Van der Waals EoS, and ideal gas EoS. The property results and percentages of differences are given and interpreted.

2. Theory
2.1 Formulation of EoS and Thermodynamic Properties

In this paper, the Schreiber-Pitzer equation of state was considered for air as a mixture of Nitrogen, Oxygen and Argon. The specific heat and the pseudocritical properties of air are calculated from the critical properties of the gases and used as input parameters to the Schreiber-Pitzer EoS. Details of the Schreiber-Pitzer EoS is given in Eq. (1).

$$Z = \frac{P}{\rho RT} = 1 + B(T_r,\rho_r)\rho_r + C(T_r,\rho_r)\rho_r^2 + D(T_r,\rho_r)\rho_r^3 +$$
$$E(T_r,\rho_r)\rho_r^5 + F(T_r,\rho_r)\rho_r^7 + G(T_r,\rho_r)\rho_r^8 +$$
$$H(T_r,\rho_r)\rho_r^{10} + I(T_r,\rho_r)\rho_r^{12} \tag{1}$$

$$B(T_r,\rho_r) = c_1 + \frac{c_2}{T_r} + \frac{c_3}{T_r^2} + \frac{c_4}{T_r^6} \tag{2}$$

$$C(T_r,\rho_r) = c_5 + \frac{c_6}{T_r} + \frac{c_7}{T_r^3} + \frac{c_8}{T_r^4}\exp(-\rho_r^2) \tag{3}$$

$$D(T_r,\rho_r) = c_9 + \frac{c_{10}}{T_r} + \frac{c_{11}}{T_r^2} \tag{4}$$

$$E(T_r,\rho_r) = \frac{c_{12}}{T_r^2} + \frac{c_{13}}{T_r^3} \tag{5}$$

$$F(T_r,\rho_r) = \frac{c_{14}}{T_r^2} + \frac{c_{15}}{T_r^3} \tag{6}$$

$$G(T_r,\rho_r) = \frac{c_{16}}{T_r^3} + \left(\frac{c_{17}}{T_r^3} + \frac{c_{18}}{T_r^5}\right)\exp(-\rho_r^2) \tag{7}$$

$$H(T_r,\rho_r) = \left(\frac{c_{19}}{T_r^3} + \frac{c_{20}}{T_r^4}\right)\exp(-\rho_r^2) \tag{8}$$

$$I(T_r,\rho_r) = \left(\frac{c_{21}}{T_r^3} + \frac{c_{22}}{T_r^4}\right)\exp(-\rho_r^2) \tag{9}$$

$$c_i = C_{i,0} + C_{i,1}\omega + C_{i,2}\omega^2 \tag{10}$$

"ω" coefficient is called Pitzer's acentric factor in Schreiber-Pitzer EoS. Acentric factor is given in Eq. (11).

$$\omega = -log_{10}P_{saturated\ vapor}(at\ T_r = 0.7) - 1 \tag{11}$$

The coefficients of Schreiber-Pitzer EoS in Eq. (10) are given in Table 1.

Table 1. Coefficients ($c_{i,j}$) of Schreiber-Pitzer EoS.

	j=1	j=2	j=3
$C_{1,j}$	0.4422590000	0.7256500000	0.0000000000
$C_{2,j}$	-0.9809700000	0.2187140000	0.0000000000
$C_{3,j}$	-0.6111420000	-1.2497600000	0.0000000000
$C_{4,j}$	-0.0051562400	-0.1891870000	0.0000000000
$C_{5,j}$	0.1513654000	2.3067060000	-10.4117400000
$C_{6,j}$	-0.0438262500	4.6960680000	15.1414600000
$C_{7,j}$	1.1026990000	3.1293840000	-9.5214090000
$C_{8,j}$	-0.6361056000	0.3266766000	2.9046220000
$C_{9,j}$	0.0087596260	-3.2040990000	8.0023380000
$C_{10,j}$	0.3412103000	8.8721690000	-14.4038600000
$C_{11,j}$	-0.8842722000	-6.6874710000	11.7685400000
$C_{12,j}$	0.1375109000	0.2432806000	-0.5515101000
$C_{13,j}$	-0.1443457000	1.2869320000	-2.1809880000
$C_{14,j}$	-0.0059695540	0.0454196100	0.0000000000
$C_{15,j}$	0.0245053700	-0.4158241000	0.7914067000
$C_{16,j}$	-0.0041995900	0.0910596000	-0.1786378000
$C_{17,j}$	0.0004665477	-1.2620280000	-2.8267720000
$C_{18,j}$	-0.0194510100	0.7812220000	4.1900460000
$C_{19,j}$	0.0408364300	1.3988440000	0.0000000000
$C_{20,j}$	-0.0354691700	-1.4560410000	0.0000000000
$C_{21,j}$	-0.0028779550	0.2104505000	0.0000000000
$C_{22,j}$	0.0058962650	0.2191255000	0.0000000000

Derivatives of the Eq. (1) are given in the Eqs. (12)-(26).

$$\frac{\partial B(T_r,\rho_r)}{\partial T} = \frac{1}{T_c}\left[-\frac{c_2}{T_r^2} - 2\frac{c_3}{T_r^3} - 6\frac{c_4}{T_r^7}\right] \tag{12}$$

$$\frac{\partial C(T_r,\rho_r)}{\partial T} = \frac{1}{T_c}\left[-\frac{c_6}{T_r^2} - 3\frac{c_7}{T_r^4} - 4\frac{c_8}{T_r^5}\exp(-\rho_r^2)\right] \tag{13}$$

$$\frac{\partial D(T_r,\rho_r)}{\partial T} = \frac{1}{T_c}\left[-\frac{c_{10}}{T_r^2} - 2\frac{c_{11}}{T_r^3}\right] \tag{14}$$

$$\frac{\partial E(T_r,\rho_r)}{\partial T} = \frac{1}{T_c}\left[-2\frac{c_{12}}{T_r^3} - 3\frac{c_{13}}{T_r^4}\right] \tag{15}$$

$$\frac{\partial F(T_r,\rho_r)}{\partial T} = \frac{1}{T_c}\left[-2\frac{c_{14}}{T_r^3} - 3\frac{c_{13}}{T_r^4}\right] \tag{16}$$

$$\frac{\partial G(T_r,\rho_r)}{\partial T} = \frac{1}{T_c}\left[-3\frac{c_{16}}{T_r^4} + \left(-3\frac{c_{17}}{T_r^4} - 5\frac{c_{18}}{T_r^6}\right)\exp(-\rho_r^2)\right] \tag{17}$$

$$\frac{\partial H(T_r,\rho_r)}{\partial T} = \frac{1}{T_c}\left[\left(-3\frac{c_{19}}{T_r^4} - 4\frac{c_{20}}{T_r^5}\right)\exp(-\rho_r^2)\right] \tag{18}$$

$$\frac{\partial I(T_r,\rho_r)}{\partial T} = \frac{1}{T_c}\left[\left(-3\frac{c_{21}}{T_r^4} - 4\frac{c_{22}}{T_r^5}\right)\exp(-\rho_r^2)\right] \tag{19}$$

$$\frac{\partial B(T_r,\rho_r)}{\partial\rho} = \frac{\partial D(T_r,\rho_r)}{\partial\rho} = \frac{\partial E(T_r,\rho_r)}{\partial\rho} = \frac{\partial F(T_r,\rho_r)}{\partial\rho} = 0 \tag{20}$$

$$\frac{\partial C(T_r,\rho_r)}{\partial\rho} = \frac{1}{\rho_c}\left[-2\rho_r\frac{c_8}{T_r^4}\exp(-\rho_r^2)\right] \tag{21}$$

$$\frac{\partial G(T_r,\rho_r)}{\partial\rho} = \frac{1}{\rho_c}\left[-2\rho_r\left(\frac{c_{17}}{T_r^3} + \frac{c_{18}}{T_r^5}\right)\exp(-\rho_r^2)\right] \tag{22}$$

$$\frac{\partial H(T_r,\rho_r)}{\partial\rho} = \frac{1}{\rho_c}\left[-2\rho_r\left(\frac{c_{19}}{T_r^3} + \frac{c_{20}}{T_r^4}\right)\exp(-\rho_r^2)\right] \tag{23}$$

$$\frac{\partial I(T_r,\rho_r)}{\partial\rho} = \frac{1}{\rho_c}\left[-2\rho_r\left(\frac{c_{21}}{T_r^3} + \frac{c_{22}}{T_r^4}\right)\exp(-\rho_r^2)\right] \tag{24}$$

$$\left.\frac{\partial P(T_r,\rho_r)}{\partial T}\right|_\rho = \rho RT\left[\frac{\partial B(T_r,\rho_r)}{\partial T}\rho_r + \frac{\partial C(T_r,\rho_r)}{\partial T}\rho_r^2 + \frac{\partial D(T_r,\rho_r)}{\partial T}\rho_r^3 +\right.$$
$$\frac{\partial E(T_r,\rho_r)}{\partial T}\rho_r^5 + \frac{\partial F(T_r,\rho_r)}{\partial T}\rho_r^7 + \frac{\partial G(T_r,\rho_r)}{\partial T}\rho_r^8 +$$
$$\left.\frac{\partial H(T_r,\rho_r)}{\partial T}\rho_r^{10} + \frac{\partial I(T_r,\rho_r)}{\partial T}\rho_r^{12}\right] + \rho R[1 + B(T_r,\rho_r)\rho_r +$$
$$C(T_r,\rho_r)\rho_r^2 + D(T_r,\rho_r)\rho_r^3 + E(T_r,\rho_r)\rho_r^5 +$$
$$F(T_r,\rho_r)\rho_r^7 + G(T_r,\rho_r)\rho_r^8 + H(T_r,\rho_r)\rho_r^{10} +$$
$$I(T_r,\rho_r)\rho_r^{12}] \tag{25}$$

$$\left.\frac{\partial P(T_r,\rho_r)}{\partial\rho}\right|_T = RT[1 + B(T_r,\rho_r)\rho_r + C(T_r,\rho_r)\rho_r^2 +$$
$$D(T_r,\rho_r)\rho_r^3 + E(T_r,\rho_r)\rho_r^5 + F(T_r,\rho_r)\rho_r^7 +$$
$$G(T_r,\rho_r)\rho_r^8 + H(T_r,\rho_r)\rho_r^{10} + I(T_r,\rho_r)\rho_r^{12}] +$$
$$\rho RT\left[\frac{\partial C(T_r,\rho_r)}{\partial\rho}\rho_r^2 + \frac{\partial G(T_r,\rho_r)}{\partial\rho}\rho_r^8 +\right.$$
$$\left.\frac{\partial H(T_r,\rho_r)}{\partial\rho}\rho_r^{10} + \frac{\partial I(T_r,\rho_r)}{\partial\rho}\rho_r^{12}\right] +$$
$$RT[B(T_r,\rho_r)\rho_r + 2C(T_r,\rho_r)\rho_r^2 +$$
$$3D(T_r,\rho_r)\rho_r^3 + 5E(T_r,\rho_r)\rho_r^5 +$$
$$7F(T_r,\rho_r)\rho_r^7 + 8G(T_r,\rho_r)\rho_r^8 +$$
$$10H(T_r,\rho_r)\rho_r^{10} + 12I(T_r,\rho_r)\rho_r^{12}] \tag{26}$$

The Helmholtz energy equation is given in Eq. (27).

$$dA = \left(\frac{\partial A(T,v)}{\partial T}\right)_v dT + \left(\frac{\partial A(T,v)}{\partial v}\right)_T dv \tag{27}$$

$$dA = -sdT - Pdv \tag{28}$$

$$\left.\frac{\partial A}{\partial v}\right|_T = -P \tag{29}$$

$$dA = -Pdv = \frac{P}{\rho^2}d\rho \tag{30}$$

$$A - A_0 = \int_{\rho_0}^{\rho} \frac{P}{\rho^2} d\rho = \int_0^{\rho} \frac{P}{\rho^2} d\rho + \int_{\rho_0}^{0} \frac{P}{\rho^2} d\rho$$

$$= \int_0^{\rho} \frac{P}{\rho^2} d\rho + \int_{\rho_0}^{0} \frac{\rho RT}{\rho^2} d\rho \tag{31}$$

The second term (limits between low density ρ_0 and zero density) can be defined as an ideal state case where $P=\rho RT$. After adding and subtracting the ideal gas density term, the equation can be written as Eq. (32).

$$A - A_0 = \int_0^{\rho} \frac{P}{\rho^2} d\rho + \int_{\rho_0}^{0} \frac{\rho RT}{\rho^2} d\rho$$

$$+ \int_0^{\rho} \frac{\rho RT}{\rho^2} d\rho - \int_0^{\rho} \frac{\rho RT}{\rho^2} d\rho \tag{32}$$

Considering the equation $P=Z\rho RT$ for real EoS, Eq. (33) is obtained.

$$A - A_0 = \int_0^{\rho} \frac{Z\rho RT - \rho RT}{\rho^2} d\rho + \int_{\rho_0}^{\rho} \frac{\rho RT}{\rho^2} d\rho \tag{33}$$

$$A - A_0 = \int_0^{\rho} \frac{RT(Z-1)}{\rho} d\rho + \int_{\rho_0}^{\rho} \frac{\rho RT}{\rho^2} d\rho \tag{34}$$

$$A - A_0 = \int_0^{\rho_r} \frac{1}{\rho_r} d\rho_r + \int_{\rho_{r0}}^{\rho_r} \frac{RT}{\rho_r} d\rho_r \tag{35}$$

$$A - A_0 = RT \int_0^{\rho_r} [B(T_r,\rho_r) + C(T_r,\rho_r)\rho_r + D(T_r,\rho_r)\rho_r^2 + E(T_r,\rho_r)\rho_r^4 + F(T_r,\rho_r)\rho_r^6 + G(T_r,\rho_r)\rho_r^7 + H(T_r,\rho_r)\rho_r^9 + I(T_r,\rho_r)\rho_r^{11}] d\rho_r + RT\ln\frac{\rho_r}{\rho_{r0}} \tag{36}$$

The terms in Eq. (36) include exponential and power multiplication terms. The integration can be carried out as Eq. (37).

$$K(m,\rho_r) = \int_0^{\rho_r} \rho_r^m \exp(-\rho_r^2) \, d\rho_r$$

$$= \int_0^{\rho_r} \sum_{n=0}^{\infty} (-1)^n \frac{\rho_r^{2n+m}}{n!} d\rho_r$$

$$= \sum_{n=0}^{\infty} (-1)^n \frac{\rho_r^{2n+m+1}}{(2n+m+1)n!} \tag{37}$$

It is easier to take the Taylor series than take numerical integrals. The Helmholtz energy equation can be written as Eq. (38).

$$A - A_0 = RT\left(B\rho_r + C_1 \frac{\rho_r^2}{2} + C_2 K(1,\rho_r) + D \frac{\rho_r^3}{3} + E \frac{\rho_r^5}{5} + F \frac{\rho_r^7}{7} + G_1 \frac{\rho_r^8}{8} + G_2, K(8,\rho_r) + H_2 K(10,\rho_r) + I_2 K(12,\rho_r) \right) + RT\ln\left(\frac{\rho_r}{\rho_{r0}}\right) \tag{38}$$

Entropy function is given in Eqs. (39) and (40).

$$s - s_0 = -\frac{\partial(A-A_0)}{\partial T}\bigg|_{\rho} \tag{39}$$

$$s - s_0 = R\left(B\rho_r + C_1 \frac{\rho_r^2}{2} + C_2 K(1,\rho_r) + D \frac{\rho_r^3}{3} + E \frac{\rho_r^5}{5} + F \frac{\rho_r^8}{8} + G_1 \frac{\rho_r^9}{9} + G_2, K(8,\rho_r) + H_2 K(10,\rho_r) + \right.$$

$$\left. I_2 K(12,\rho_r) \right) + RT\left(\frac{dB}{dT}\rho_r + \frac{dC_1}{dT}\frac{\rho_r^2}{2} + \frac{dC_2}{dT}K(1,\rho_r) + \frac{dD}{dT}\frac{\rho_r^3}{3} + \frac{dE}{dT}\frac{\rho_r^5}{5} + \frac{dF}{dT}\frac{\rho_r^8}{8} + \frac{dG_1}{dT}\frac{\rho_r^9}{9} + \frac{dG_2}{dT}K(8,\rho_r) + \frac{dH_2}{dT}K(10,\rho_r) + \frac{dI_2}{dT}K(12,\rho_r) \right) + R\ln\left(\frac{\rho_r}{\rho_{r0}}\right) \tag{40}$$

Internal energy function is expressed as Eq. (41).

$$u - u_0 = (A - A_0) + T(S - S_0) \tag{41}$$

Enthalpy energy function can be evaluated as Eq. (42).

$$h - h_0 = (A - A_0) + T(S - S_0) + RT(Z - 1) \tag{42}$$

Gibbs energy function is given in Eq. (43).

$$G - G_0 = (A - A_0) + RT(Z - 1) \tag{43}$$

The fugacity-pressure ratio can be evaluated as Eq. (44).

$$\ln\frac{f}{P} = \frac{(A-A_0)}{RT} + \ln\frac{v}{v_0} + (Z-1) - \ln(Z) \tag{44}$$

Thermodynamic properties of air are calculated by assuming air as a gas mixture of Nitrogen, Oxygen, and Argon. The air mixture ratios are given in Table 2.

Table 2. Air mixture ratios.

Gas	Formula	Mole (%)	Molar mass, M (kg/kmol)
Nitrogen	N_2	0.78112	28.014
Oxygen	O_2	0.20954	31.998
Argon	Ar	0.00934	39.948
Air		1	28.96029

The NIST-JANAF tables are used to solve the $c_p(T)$ for air as a mixture of Nitrogen, Oxygen, and Argon [12]. Mixing rule is applied to establish $c_p(T)$ of air which was given in Eq. (45).

$$c_{p,air}(T) = N_{N2}c_{p,N2}(T) + N_{O2}c_{p,O2}(T) + N_{Ar}c_{p,Ar}(T) \tag{45}$$

In this paper, cubic spline interpolation is used to calculate the $c_p(T)$ values. In the cubic spline interpolation, a third-degree polynomial equation is considered, which is given in Eq. (46).

$$s_k(x) = a_k(x - x_k) + b_k(x_{k+1} - x) + \frac{[(x-x_k)^3 c_{k+1} + (x_{k+1}-x)^3 c_k]}{6h_k}$$

$$1 \le k \le n \tag{46}$$

The first and second derivative of the third-degree polynomial is given in Eq. (47) and Eq. (48).

$$h_k = x_{k+1} - x_k \quad 1 \le k \le n$$

$$s'_k(x) = a_k - b_k + \frac{[(x-x_k)^2 c_{k+1} - (x_{k+1}-x)^2 c_k]}{2h_k} \tag{47}$$

$$s''_k(x) = \frac{[(x-x_k)c_{k+1} - (x_{k+1}-x)c_k]}{h_k} \tag{48}$$

The equations are evaluated through additional rules.

$$S_k(x_k) = y_k \tag{49}$$

$$S_k(x_{k+1}) = y_{k+1} \tag{50}$$

$$S_k(x_k) = y_k = b_k(x_{k+1} - x_k) + \left[\frac{(x_{k+1}-x_k)^3}{6h_k}C_k\right]$$
$$= \left[b_k h_k + \frac{h_k^3}{6h_k}C_k\right] \tag{51}$$

$$S_k(x_{k+1}) = y_{k+1} = a_k(x_{k+1} - x_k) + \left[\frac{(x_{k+1}-x_k)^3}{6h_k}C_{k+1}\right]$$
$$= a_k h_k + \left[\frac{h_k^3}{6h_k}C_{k+1}\right] \tag{52}$$

The "a_k" and "b_k" coefficients can be evaluated as Eqs. (53) and (54).

$$a_k = \frac{[6y_{k+1}-h_k^2 c_{k+1}]}{6h_k} \qquad 1 \le k \le n \tag{53}$$

$$b_k = \frac{[6y_k - h_k^2 c_k]}{6h_k} \qquad 1 \le k \le n \tag{54}$$

The equations are evaluated considering the boundary conditions.

$$S'_{k-1}(x_k) = S'_k(x_k) \tag{55}$$

$$S'_k(x_k) = a_k - b_k - \left[\frac{(x_{k+1}-x_k)^2}{2h_k}C_k\right]$$
$$= a_k - b_k \left[\frac{h_k^2}{2h_k}C_k\right] \tag{56}$$

$$S'_{k-1}(x_k) = a_{k-1} - b_{k-1} + \left[\frac{(x_k - x_{k-1})^2}{2h_{k-1}}C_k\right]$$
$$= a_{k-1} - b_{k-1} + \left[\frac{h_{k-1}^2}{2h_{k-1}}C_k\right] \tag{57}$$

$$a_k - b_k - \left[\frac{h_k}{2}C_k\right] = a_{k-1} - b_{k-1} + \left[\frac{h_{k-1}}{2}C_k\right] \tag{58}$$

$$\left[\frac{6y_{k+1}-h_k^2 C_{k+1}}{6h_k}\right] - \left[\frac{6y_k - h_k^2 C_k}{6h_k}\right] - \left[\frac{h_k}{2}C_k\right]$$
$$= \left[\frac{6y_k - h_{k-1}^2 C_k}{6h_{k-1}}\right] - \left[\frac{6y_{k-1}-h_{k-1}^2 C_{k-1}}{6h_{k-1}}\right] + \left[\frac{h_{k-1}}{2}\right]C_k \tag{59}$$

Eq. (60) is obtained by deriving from Eq. (59).

$$h_{k-1}C_{k-1} + 2C_k(h_{k-1} + h_k) + h_k C_{k+1}$$
$$= 6\left[\left[\frac{y_{k+1}-y_k}{h_k}\right] - \left[\frac{y_k - y_{k-1}}{h_{k-1}}\right]\right] \tag{60}$$

The system of equations is given in Eq. (62) with the application of Eq. (61) definition.

$$w_k = \frac{y_{k+1}-y_k}{h_k} = \frac{y_{k+1}-y_k}{x_{k+1}-x_k} \qquad 1 \le k \le n \tag{61}$$

$$\begin{bmatrix} \frac{1}{h_1} & & & & & & \\ 2(h_1+h_2) & h_2 & & & & & \\ h_2 & 2(h_2+h_3) & & & & & \\ \cdots & \cdots & \cdots & & & & \\ & & & \cdots & & \cdots & \cdots \\ & & & \cdots & 2(h_{n-3}+h_{n-2}) & h_{n-2} & \\ & & & & h_{n-2} & 2(h_{n-2}+h_{n-1}) & h_{n-1} \\ & & & & & & 1 \end{bmatrix}\begin{Bmatrix} c_0 \\ c_1 \\ c_2 \\ \cdots \\ c_{n-2} \\ c_{n-1} \\ c_n \end{Bmatrix} =$$
$$\begin{Bmatrix} A \\ 6(w_2 - w_1) \\ 6(w_3 - w_2) \\ \cdots \\ 6(w_{n-2}-w_{n-3}) \\ 6(w_{n-1}-w_{n-2}) \\ B \end{Bmatrix} \tag{62}$$

The system of equation has "n-2" terms to be solved. In the equation there are second derivative at the end conditions. "A" and "B" values should be defined by the users. The matrix which is given in Eq. (62) is a band matrix, it can be solved by using band matrix algorithms such as Thomas algorithm or another method. The cubic spline interpolation, which is given above, was used to calculate the $c_p(T)$ values of air as a mixture.

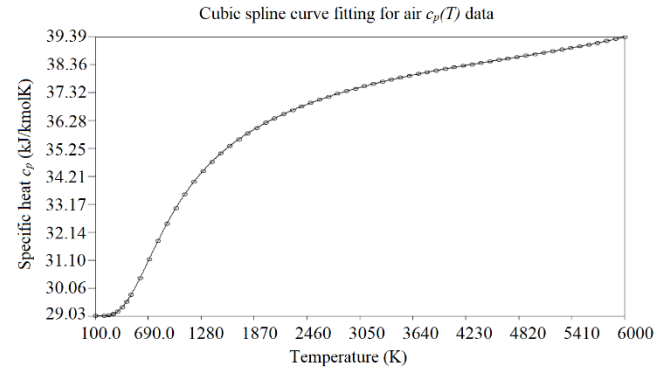The cubic spline curve fitting for air $c_p(T)$ data is given in Figure 1.

Figure 1. Specific heat of air ($c_p(T)$, kJ/kmolK).

The pseudocritical property approach is used to calculate the gas mixture properties. Mixing rules for Schreiber-Pitzer EoS are given in the equations.

$$N = \sum_i N_i \tag{63}$$

"N_i" is the mole number of each substance in the mixture.

$$y_i = \frac{N_i}{N} \tag{64}$$

"y_i" is the mole percentages of each substance.

Mixture properties can be calculated by assuming pseudocritical values from mixing equations and air is assumed as a single gas instead of gas mixtures [13].

$$T_{cm} = \sum_{i=1}^m \sum_{j=1}^m y_i y_j T_{cij} \tag{65}$$

$$V_{cm} = \sum_{i=1}^m \sum_{j=1}^m y_i y_j V_{cij} \tag{66}$$

To calculate the mixture interaction, combination rules must be devised to obtain T_{cij}, P_{cij}, and w_{ij}. Leland and Chappelear [14] and Ramaiah and Stiel [15] investigated the mixture interactions.

$$T_{cij} = \sqrt{T_{ci}T_{cj}}(1 - k_{ij}) \tag{67}$$

$$P_{cij} = \frac{Z_{cij}RT_{cij}}{V_{cij}} \tag{68}$$

$$\omega_{ij} = \frac{1}{2}[\omega_i + \omega_j] \tag{69}$$

$$V_{cij} = \frac{1}{8}\left[(V_{ci})^{\frac{1}{3}} + (V_{cj})^{\frac{1}{3}}\right]^3 \tag{70}$$

$$Z_{cij} = \frac{1}{2}[Z_{ci} + Z_{cj}] \tag{71}$$

"k_{ij}" is the binary interaction coefficient, which is given in Eq. (72). Tsonopoulos [16] investigated the prediction and correlation of interaction coefficients. The guidelines for estimating the interaction coefficients have been given by Tarakad and Danner [17].

$$k_{ij} = 1 - \frac{\left(V_{crit\,ii}V_{crit\,jj}\right)^{\frac{1}{2}}}{V_{crit\,ij}} \tag{72}$$

2.2 Formulation of Thermophysical Properties

The thermophysical properties of air, such as thermal conductivity and viscosity, are calculated with the equations suggested by Kadoya et al [18].

$$\eta(T_r, \rho_r) = H\big[\eta_0(T_r) + \Delta\eta(\rho_r)\big] \tag{73}$$

$$\eta_0(T_r) = A_0 T_r + A_1 T_r^{0.5} + A_2 + \frac{A_3}{T_r} + \frac{A_4}{T_r^2} + \frac{A_5}{T_r^3} + \frac{A_6}{T_r^4} \tag{74}$$

$$\Delta\eta(\rho_r) = \sum_{i=1}^{4} B_i \rho_r^i \tag{75}$$

$$k(T_r, \rho_r) = \Lambda\big[k_0(T_r) + \Delta k(\rho_r)\big] \tag{76}$$

$$k_0(T_r) = C_0 T_r + C_1 T_r^{0.5} + C_2 + \frac{C_3}{T_r} + \frac{C_4}{T_r^2} + \frac{C_5}{T_r^3} + \frac{C}{T_r^4} \tag{77}$$

$$\Delta k(\rho_r) = \sum_{i=1}^{4} D_i \rho_r^i \tag{78}$$

$$\rho_r = \frac{\rho}{\rho^*} \tag{79}$$

$$T_r = \frac{T}{T^*} \tag{80}$$

In Eq. (73) and Eq. (76) "H" is equal to 6.1609 (10^{-6} Pa), "Λ" is equal to 25.9778 (10^{-3} $W/(mK)$), ρ^* is equal to 314.3 kg/m^3 and T^* is equal to 132.5 K. The coefficients of Eqs. (73) and (76) are given in Table 3.

Table 3. Coefficients of Eq. (73) and Eq. (76).

i	A_i	B_i	C_i	D_i
0	0.128517	0.465601	0.239503	0.402287
1	2.60661	1.26469	0.00649768	0.356603
2	-1	-0.511425	1	-0.163159
3	-0.709661	0.2746	-1.92615	0.138059
4	0.662534		2.00383	-0.0201725
5	-0.197846		-1.07553	
6	0.00770147		0.229414	

Additional properties derived from EoS are given in Table 4.

Table 4. Additional properties derived from EoS.

Properties	Equation
Prandtl number	$Pr = \dfrac{c_p \mu}{k}$
Speed of sound	$a = \sqrt{-\left(\dfrac{v^2 c_p}{c_v M}\right)\left(\dfrac{\partial P}{\partial v}\right)_T}$
Thermal expansion coefficient	$\beta = -\dfrac{1}{\rho}\left(\dfrac{\partial \rho}{\partial T}\right)_P$
Isothermal compressibility	$\beta_T = \sqrt{\dfrac{v}{\left(\dfrac{\partial P}{\partial v}\right)_T}}$

3. Results

The Java language is used to carry out the analysis. The list of programs is given in Table 5. The programs are available on the internet web site for free utilization by researchers [19].

Table 5. Java program list.

Java program	Explanation
Interface if_x	The basic interface for the general definition of the function f(x), including derivatives, integrals, and root-finding algorithms.
air_SP_CS	The Schreiber-Pitzer EoS was considered for air, utilizing cubic spline curve fitting for c_p values.
air_PR_CS	The Peng-Robinson EoS was considered for air, utilizing cubic spline curve fitting for c_p values.
air_RK_CS	The Redlich-Kwong EoS was considered for air, utilizing cubic spline curve fitting for c_p values.
air_VDW_CS	The Van der Waals EoS was considered for air, utilizing cubic spline curve fitting for c_p values.
air_PG_CS	The ideal gas EoS was considered for air, utilizing cubic spline curve fitting for c_p values.

Comparisons of five EoS results for air as a mixture are given in Table 6 and the comparisons of additional property results derived from EoS for air are given in Table 7.

Table 6. Comparisons of different EoS results.

EoS	P kPa	T K	v m³/kg	h kJ/kg	u kJ/kg	s kJ/kgK
Schreiber-Pitzer	100	300	0.861287	200.3428	114.2382	5.842212
Peng-Robinson	100	300	0.860835	200.5240	114.4406	5.842357
Redlich-Kwong	100	300	0.860913	200.4628	114.3715	5.842153
Van der Waals	100	300	0.860681	200.3165	114.2484	5.842157
Ideal gas	100	300	0.861301	200.5688	114.4387	5.842792
Schreiber-Pitzer	500	300	0.172250	199.4418	113.4324	5.377784
Peng-Robinson	500	300	0.171796	200.3461	114.4481	5.378532
Redlich-Kwong	500	300	0.171880	200.0423	114.1022	5.377530
Van der Waals	500	300	0.171646	199.3055	113.4825	5.377539
Ideal gas	500	300	0.172260	200.5688	114.4387	5.380722
Schreiber-Pitzer	1000	300	0.086121	198.3379	112.4311	5.175817
Peng-Robinson	1000	300	0.085668	200.1259	114.4574	5.177331
Redlich-Kwong	1000	300	0.085761	199.5264	113.7659	5.175355
Van der Waals	1000	300	0.085524	198.0427	112.5191	5.175345
Ideal gas	1000	300	0.086130	200.5688	114.4387	5.181719
Schreiber-Pitzer	5000	300	0.017217	190.3800	104.6491	4.689713
Peng-Robinson	5000	300	0.016788	198.4718	114.5311	4.697481
Redlich-Kwong	5000	300	0.016944	195.8235	111.1020	4.688837
Van der Waals	5000	300	0.016695	188.0779	104.6028	4.687668
Ideal gas	5000	300	0.017226	200.5688	114.4387	4.719648

Table 7. Comparisons of additional properties derived from EoS.

EoS	P kPa	T K	Pr	a m/s	β 1/K	β_T 1/Pa
Schreiber-Pitzer	100	300	0.71203	347.2425	0.00333	1E-5
Peng-Robinson	100	300	0.71203	347.0611	0.00333	1E-5
Redlich-Kwong	100	300	0.71203	347.2382	0.00333	1E-5
Van der Waals	100	300	0.71203	347.2176	0.00333	1E-5
Ideal gas	100	300	0.71203	347.2476	0.00333	1E-5
Schreiber-Pitzer	500	300	0.71209	347.2281	0.00333	2E-6
Peng-Robinson	500	300	0.71209	346.3495	0.00333	2E-6
Redlich-Kwong	500	300	0.71209	347.2122	0.00333	2E-6
Van der Waals	500	300	0.71209	347.1212	0.00333	2E-6
Ideal gas	500	300	0.71209	347.2476	0.00333	2E-6
Schreiber-Pitzer	1000	300	0.71216	347.2103	0.00334	1E-6
Peng-Robinson	1000	300	0.71216	345.5365	0.00333	1E-6
Redlich-Kwong	1000	300	0.71216	347.2054	0.00333	1E-6
Van der Waals	1000	300	0.71216	347.0547	0.00333	1E-6
Ideal gas	1000	300	0.71216	347.2476	0.00333	1E-6
Schreiber-Pitzer	5000	300	0.71274	347.0718	0.00335	2E-7
Peng-Robinson	5000	300	0.71276	342.0295	0.00334	2E-7
Redlich-Kwong	5000	300	0.71275	348.2911	0.00334	2E-7
Van der Waals	5000	300	0.71276	349.0760	0.00334	2E-7
Ideal gas	5000	300	0.71274	347.2476	0.00333	2E-7

The Schreiber-Pitzer EoS results are compared with Peng-Robinson EoS, Redlich-Kwong EoS, Van der Waals EoS, and ideal gas EoS utilizing cubic spline curve fitting for c_p values. The enthalpy percentages of differences are given in Figure 2 to Figure 5. The enthalpy percentages of differences are increasing with increasing pressure and decreasing temperature.

The enthalpy values obtained from Schreiber-Pitzer EoS have maximum difference percentages of %-13.37 from Peng-Robinson EoS values, %-9.808 from Redlich-Kwong EoS values, %3.595 from Van der Waals EoS values and %-21.9 from ideal gas EoS respectively for investigated region. The enthalpy percentages of differences decrease when the pressures decrease or the temperatures increase.
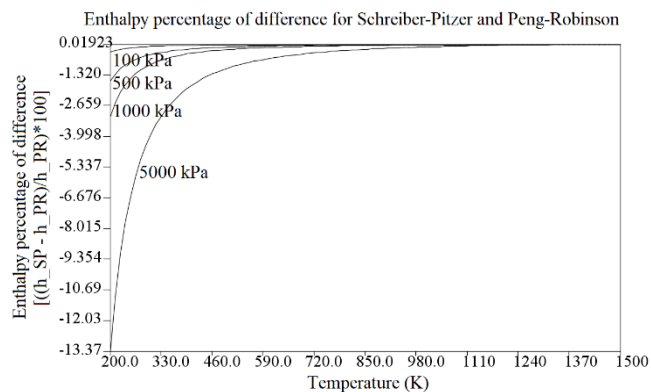
Figure 2. The enthalpy percentage of difference for Schreiber-Pitzer EoS and Peng-Robinson EoS.
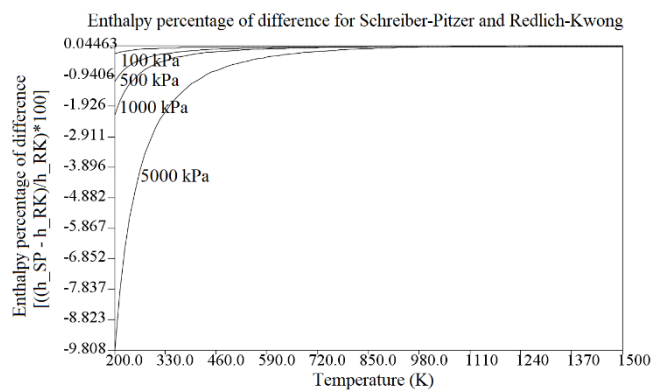
Figure 3. The enthalpy percentage of difference for Schreiber-Pitzer EoS and Redlich-Kwong EoS.
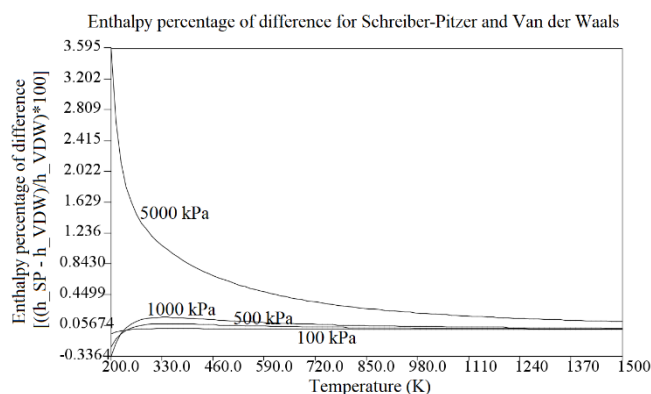

Figure 4. The enthalpy percentage of difference for Schreiber-Pitzer EoS and Van der Waals EoS.
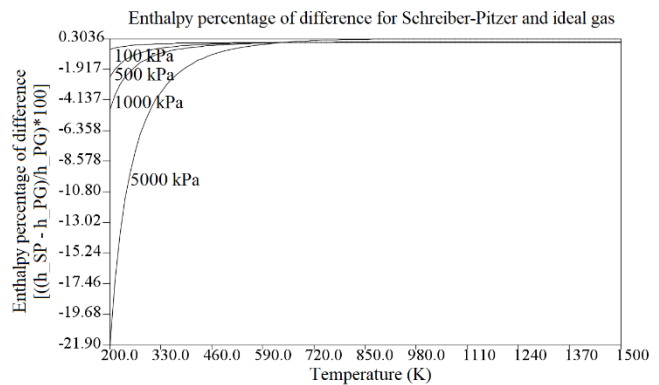

Figure 5. The enthalpy percentage of difference for Schreiber-Pitzer EoS and ideal gas EoS.

The Schreiber-Pitzer EoS entropy results are compared with Peng-Robinson EoS, Redlich-Kwong EoS, Van der Waals EoS, and ideal gas EoS results. The entropy percentages of differences are given in Figure 6 to Figure 9. The entropy percentages of differences are increasing with increasing pressure and decreasing temperature.

The entropy values obtained from Schreiber-Pitzer EoS have maximum difference percentages of %0.5828 from Peng-Robinson EoS values, %0.8808 from Redlich-Kwong EoS values, %0.6244 from Van der Waals EoS values and %1.319 from ideal gas EoS respectively for investigated region. The entropy percentages of differences decrease with increasing temperatures or decreasing pressures.
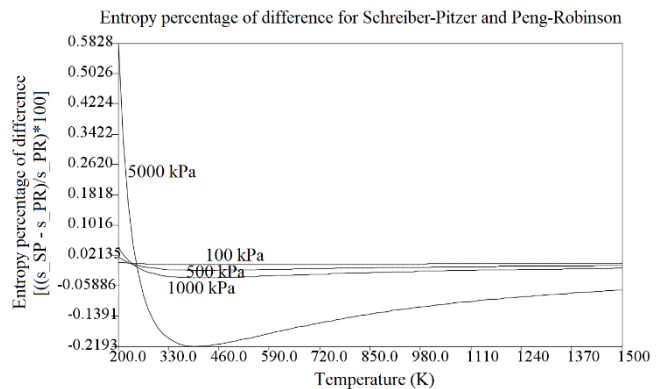

Figure 6. The entropy percentage of difference for Schreiber-Pitzer EoS and Peng-Robinson EoS.
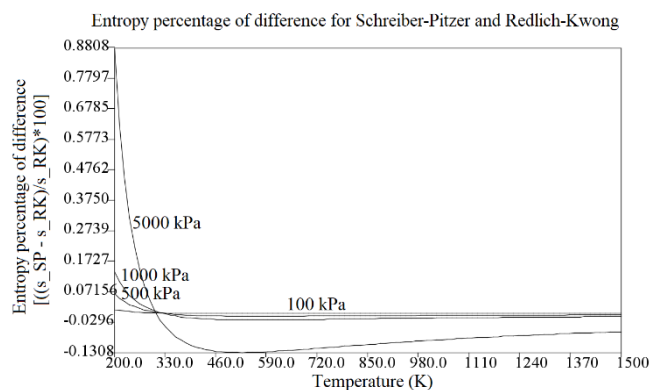

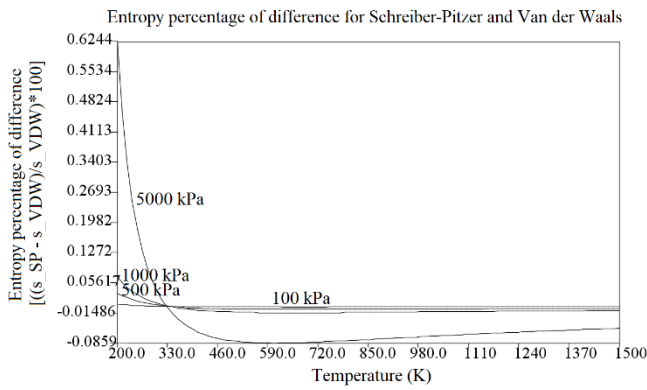*Figure 7. The entropy percentage of difference for Schreiber-Pitzer EoS and Redlich-Kwong EoS.*

Figure 8. The entropy percentage of difference for Schreiber-Pitzer EoS and Van der Waals EoS.
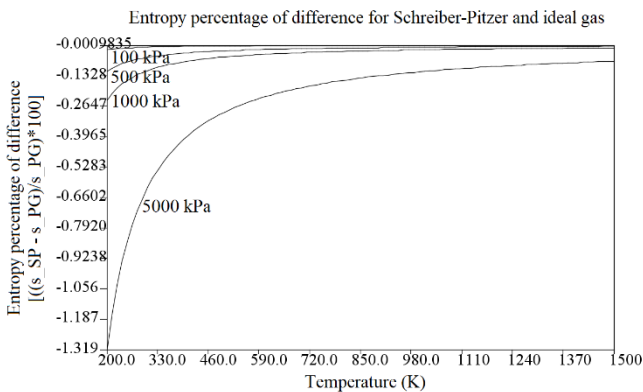

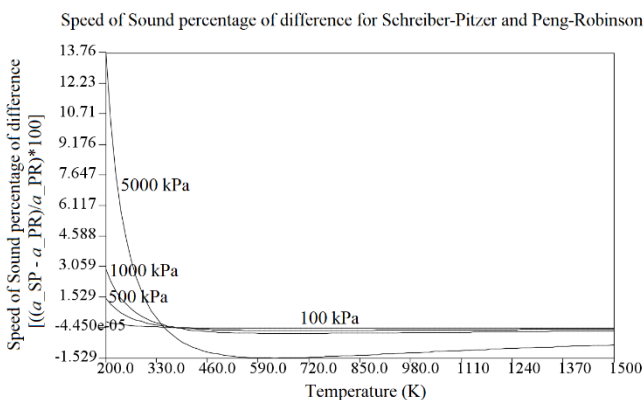Figure 9. The entropy percentage of difference for Schreiber-Pitzer EoS and ideal gas EoS.

Figure 10. The speed of sound percentage of difference for Schreiber-Pitzer EoS and Peng-Robinson EoS.
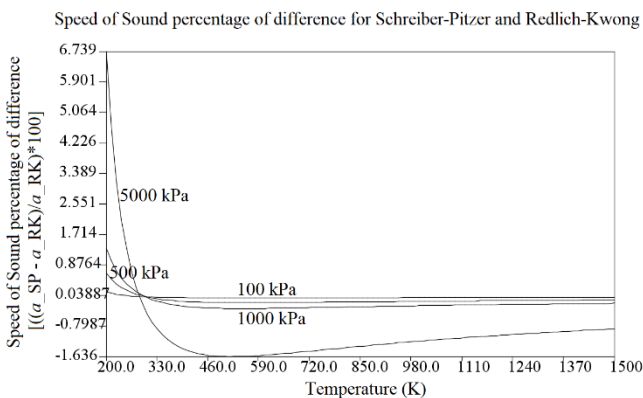

Figure 11. The speed of sound percentage of difference for Schreiber-Pitzer EoS and Redlich-Kwong EoS.
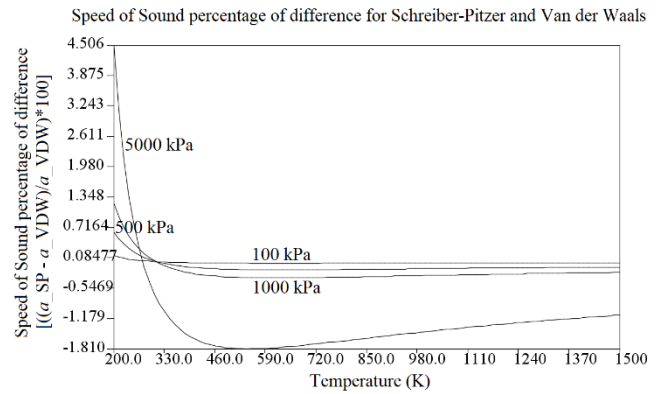

Figure 12. The speed of sound percentage of difference for Schreiber-Pitzer EoS and Van der Waals EoS.
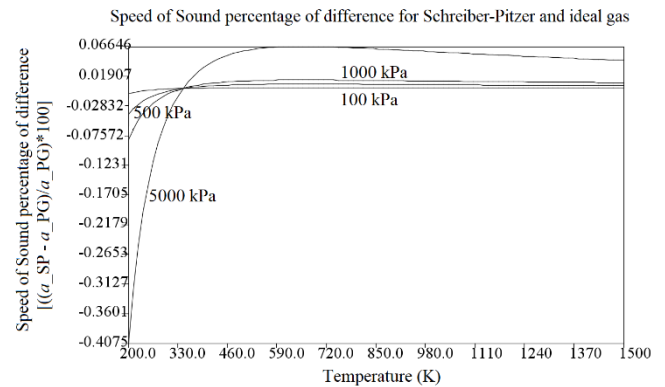

Figure 13. The speed of sound percentage of difference for Schreiber-Pitzer EoS and ideal gas EoS.

Comparisons of additional properties derived from EoS for air are investigated and the differences occurred in the speed of sound are given in Figure 10 to Figure 13. The speed of sound percentages of differences are increasing with increasing pressure and decreasing temperature.

The speed of sound values obtained from Schreiber-Pitzer EoS have maximum difference percentages of %13.76 from Peng-Robinson EoS values, %6.739 from Redlich-Kwong EoS values, %4.506 from Van der Waals EoS values and %-0.4075 from ideal gas EoS.

3. Conclusions

The ideal gas EoS is usually used in gas thermodynamic property calculations, but in applications with higher pressure zones, the error levels are increasing, so better accuracy of thermodynamic properties will be required for extreme cases. In this study, Schreiber-Pitzer EoS is considered for better accuracy of the thermodynamic properties of air mixtures.

The Java language is used to calculate the thermodynamic and thermophysical properties of air as a mixture of Nitrogen, Oxygen, and Argon. The Schreiber-Pitzer EoS results are compared with Peng-Robinson EoS, Redlich-Kwong EoS, Van der Waals EoS, and ideal gas EoS utilizing cubic spline curve fitting for c_p values. The percentages of differences for thermodynamic and thermophysical properties are calculated, and the percentages are increasing with increasing pressure and decreasing temperature. When the pressures decrease, the percentages of differences decrease rapidly. On the other hand, the percentages of differences decrease and have very small values when the temperatures increase.

The Schreiber-Pitzer EoS is the most accurate one compared to the other EoS. It should be noted that all these

equations are general models. For better accuracy, equations of state are developed by using actual laboratory measurements. In the literature, there are not many studies that have been examined in this context. Coban in 2021, considered Schreiber-Pitzer EoS to calculate the thermodynamic properties of Nitrogen utilizing polynomial curve fitting for c_p values. The Schreiber-Pitzer EoS results are compared with Peng-Robinson EoS, Lee-Kesler EoS and ideal gas EoS [20]. Coban developed the stoichiometric chemical equilibrium algorithm by using Schreiber-Pitzer EoS. Equilibrium calculations are based on atomic mass balances and the minimization of Gibbs energy [21].

The Schreiber-Pitzer EoS is not known like other EoS, so it is not widely used. Even though main idea of Pitzer (Pitzer acentric factor) are heavily used in other well-known equation of states such as Peng-Robinson, Redlich-Kwong, Lee-Kesler EoS etc. The main reason for this is the simplicity of the other EoS. For example, Lee-Kesler EoS utilizes linear interpolation between two reference fluids based on Pitzer acentric factor, but Schreiber-Pitzer EoS utilizes higher degree curve fitting values utilizing 22 gases. Schreiber-Pitzer EoS can be used for compressibility factor calculations, real gas mixtures including moist gas mixtures and combustion processes due to its better accuracy compare to other known equation of states.

Nomenclature

A	Helmholtz energy (kJ/kg)
a	Speed of sound (m/s)
B,C,D,E,F,G,H,I	Schreiber-Pitzer EoS constants
c_p	Specific heat at constant pressure (kJ/kgK)
c_v	Specific heat at constant volume (kJ/kgK)
G	Gibbs energy (kJ/kg)
h	Enthalpy (kJ/kg)
k	Thermal conductivity (W/mK)
M	Molar mass (kg/kmol)
N	Mole
P	Pressure (kPa)
Pr	Prandtl number
R	Universal gas constant
s	Entropy (kJ/kgK)
T	Temperature (K)
T_c	Critical temperature (K)
T_r	Reduced pressure
u	Internal energy (kJ/kg)
v	Specific volume (m³/kg)
w	Pitzer's acentric factor
Z	Compressibility factor
ρ	Density (kg/m³)
β	Thermal expansion coefficient (1/K)
η	Viscosity (Pa.s)
β_T	Isothermal compressibility (1/Pa)

References:

[1] J. D. Van der Waals, "The Equation of State for Gases and Liquids", *Nobel Lecture*, December 12, 1910.

[2] J. D. Van der Waals, "Over de Continuiteit van den Gas- en Vloeistoftoestand", University of Leiden, 1873.

[3] O. Redlich, J. N. S. Kwong, "On the Thermodynamics of Solutions", *Chem. Rev.*, 44 (1): 233–244, 1949.

[4] D. Peng, D. B. Robinson, "A New Two-Constant Equation of State", *Ind. Eng. Chem. Fundam.*, Vol. 15, No. 1, 1976.

[5] Z. Nasri, B. Housam, "Applications of the Peng Robinson Equation of State Using MATLAB", *Chemical Engineering Education*, 43, 2009.

[6] J. S. Lopez-Echeverry, S. Reif-Acherman, E. Araujo-Lopez, "Peng-Robinson Equation of State: 40 Years Through Cubics", *Fluid Phase Equilibria*, 447, 39-71, 2017.

[7] M. Ghanbari, M. Ahmadi, A. Lashanizadegan, "A Comparison Between Peng-Robinson and Soave-Redlich-Kwong Cubic Equations of State from Modification Perspective", *Cryogenics*, 84: 13-19, 2017.

[8] P. Ghosh, "Prediction of Vapor-Liquid Equilibria Using Peng-Robinson and Soave-Redlich-Kwong Equations of State", *Chem. Eng. Technol.*, 22: 379-399, 1999.

[9] M.S. Zabaloy, J. H. Vera, "The Peng-Robinson Sequel. An Analysis of the Particulars of the Second and Third Generations", *Indus. Eng. Chem. Res.*, 37: 1591-1597, 1998.

[10] J. O. Valderrama, "The State of the Cubic Equations of State", *Indus. Eng. Chem. Res.*, 42: 1603-1618, 2003.

[11] D. R. Schreiber, K. S. Pitzer, "Selected Equation of State in the Acentric Factor System", *International Journal of Thermophysics*, Vol 9, No. 6, 1988.

[12] NIST-JANAF Thermochemical Tables [Online]. Available: https://janaf.nist.gov/, (accessed Jan. 1, 2022).

[13] R. C. Reid, J. M. Prausnitz, B. E. Poling, *The Properties of Gases & Liquids*, Fourth Edition, McGraw-Hill, 1987.

[14] T. W. Leland, P. S. Chappelear, "The Corresponding States Principle", *Industrial and Engineering Chemistry*, Vol. 60 No. 7, 1968.

[15] V. Ramaiah, L. I. Stiel, "Effective Parameters for Nonpolar Mixtures from Properties of Components", *Ind. Eng. Chem. Process Des. Develop.*, Vol. 11, No. 4, 1972.

[16] C. Tsonopoulos, "Second Virial Cross-Coefficients: Correlation and Prediction of k_{ij}", *Advances in Chemistry*, Vol. 182, 1979.

[17] R. R. Tarakad, R. P. Danner, "An Improved Corresponding States Method for Polar Fluids: Correlation of Second Virial Coefficients", *AIChE Journal, Vol.* 23, No. 5, 685, 1977.

[18] K. Kadoya, N. Matsunaga, A. Nagashima, "Viscosity and Thermal Conductivity of Dry Air in the Gaseous Phase", *Journal of Physical and Chemical Reference Data 14*, 947, 1985.

[19] M. Turhan ÇOBAN Web Site [Online]. Available: www.turhancoban.com, (accessed Jan. 1, 2022).

[20] M. T. Coban, "Thermodynamic and Thermophysical Properties of Pure Gases By Using Schreiber-Pitzer EoS", *ULIBTK'21 23. Isı Bilimi ve Tekniği Kongresi*, 08-10 Eylül 2021.

[21] M. T. Coban, "Stoichiometric Chemical Equilibrium Algorithm by Using Schreiber and Pitzer Real Gas EoS and Homotophy (Continuation) Method for Solving Non-Linear System of Equations", *ULIBTK'21 23. Isı Bilimi ve Tekniği Kongresi*, 08-10 Eylül 2021.

Research Article

Thermodynamic Assessment of the Impact of Pregnancy and Lactation on the Longevity of Women

[1]G. Ulu 🆔, [2]M.E. Öngel 🆔, [3]B. Yilmaz 🆔, [4*]M. Özilgen 🆔

[1] Yeditepe University, Department of Nutrition and Dietetics, 34755 Atasehir, Istanbul, Turkey
[2,3] Yeditepe University, Faculty of Medicine, Department of Medical Physiology, 34755 Atasehir, Istanbul, Turkey
[4] Department of Food Engineering, 34755 Atasehir, Istanbul, Turkey
E-mails: [1]gizemmulu@hotmail.com, [2]meceongel@gmail.com, [3]byilmaz@yeditepe.edu.tr, [4*]mozilgen@yeditepe.edu.tr

Abstract

Effects of the pregnancy and the following lactation periods on the lifespan entropy of the women has been evaluated. In the case of singleton pregnancy, a wealthy woman may generate 1.5% and in the case of twin pregnancy 2.1% of the total lifespan entropy of a non-pregnant wealthy women. In the case of a poor woman the singleton pregnancy, may generate 1.8% and in case of the twin pregnancy 2.1% of the total lifespan entropy generated by the non-pregnant wealthy woman. Results of the diet-based thermodynamic calculations for the poor women are compared with the demographic data collected across pre-industrial Europe and a good agreement was found.

Keywords: *Thermodynamic assessment; entropy generation; diet-based entropic age; telomere length-based energy efficiency; pregnancy; lactation; historic demographic data.*

1. Introduction

The ageing research is carried in different paths: morphological cellular changes are traced with highly advanced observation techniques [1,2]. Joseph et al, [3] argued that the chemical reactions of cellular energy metabolism produce reactive oxygen species as byproducts; the oxidative damage accelerates aging via damaging the DNA, proteins and lipids. Mechanisms of occurrence of the ageing related distortion of the DNA strands and the struggle of the cells to counter this constitute another major ageing research path [4-10]. Although the organisms have a defense mechanism against the oxidative damage, it can still occur, especially if the organisms are not taking in adequate antioxidants from their diets. Accumulation of oxidative damage in the tissues accelerates aging [11, 12]. Living organisms are far from equilibrium structures, and they have a great tendency for approaching the equilibrium, which implies aging and increased entropy [13]. To survive at far from equilibrium, a living being should develop an entropy gradient with their surroundings. Such gradients are maintained only by utilizing energy imported from outside, so an open system may move away from near towards far from equilibrium. One of the major paths of the ageing research employs the fundamental principles of the thermodynamics and refers to the "*entropic age*" concept to study the ageing associated overwhelming of the maintenance systems of the body and the loss of molecular functions [14-16]. Silva and Annamalai [17, 18] and Annamalai, and Silva [19] quantified the entropy generation related ageing stress on individual organs. Living organisms maintain a highly organized structure by exporting entropy [20]. A fraction of the generated entropy accumulates in the

body increases disorder and structural impairment [13]. All the living beings die after reaching the lifespan entropy generation limit, since their bodies cannot stand accumulating more damage. Genetically induced repair and replacement processes are capable of maintaining the balance in favor of the functioning molecules when the organisms are young, but with ageing the balance between these processes tends toward inactivation and malfunctioning [14-16]. Following exactly the same behavior as the other dissipative systems, energy is needed to prevent entropy accumulation and heal the collected damage [21]. As explained by Yalcinkaya et al. [22] with the decline of the mitochondrial energy conversion, organisms start experiencing structural impairment. The concept of "entropic age" helps to quantify the damage accumulation by an organism in a systematic manner. The rate of living slowly wears out the cellular machinery, so a faster metabolism will "wear out" it more quickly. In their studies on thyroid function, Jumpertz et al [23], after following their subjects for 11 to 15 years, and deaths from natural causes concluded that for each 100-calorie (418 J) of additional nutrient uptake, corresponding to approximately 100*100/1500= 6% additional intake, the risk of natural mortality increased by 25 to 29 percent. Caloric restriction and negative energy balance have been shown to reduce resting metabolic rate, and in contrast overeating increases resting metabolic rate [24,25]. Furthermore, caloric restriction has been consistently shown to extend maximal lifespan by up to 60 % in animals [26].

Kuddusi (2015) after noting that the people living in different regions of Turkey have different food habits calculated the lifetime entropy generation per unit mass of a

person and found substantial difference among their life expectancy. Kuddusi [27] determined that the metabolic entropy generation rate was 0.46×10^{-5} kW/kg K in the Marmara district of Turkey with the expected lifespan of 78.61 years, whereas in Eastern Turkey, metabolic entropy generation rate was 0.52×10^{-5} kW/kg K with the expected lifespan of 69.54 years. Patel and Rajput [28] performed similar calculations for different climate zones of India and Öngel et al [29] improved these analyses by incorporating the telomere effects. Entropic age concept suggests that a fast metabolism by generating more entropy could make people age more quickly.

1.1. Telomere Length as the Measure of the Thermodynamic Efficiency

Telomere length is birth-inherited and becomes about 50–100 base pair shorter every time the cell replicates [30]. At birth, there is no significant difference in telomere length between men and women. Telomere length remains higher in women than that of men as they age, probably because of their higher estrogen levels [31]. Estrogen has antioxidant properties that play a massive role in human reproduction and the menstrual cycle [32]. The disposable soma theory states that the organisms have limited resources to spend for their cellular processes; therefore, an investment for growth and reproduction will reduce the investment for DNA repair and open the way for cellular damage, shortened telomeres and accumulating mutations [33]. During energy deficiency, telomeres may interfere with signaling and re-direct critical resources to immediately important processes [34]; the longer telomeres may increase energy utilization efficiency [35]. An inappropriate pregnancy diet may lead to telomere shortening and chronic diseases [35]. Caloric restriction may change the energy allocation preference of the organisms. Roberts et al [36, 37] reported a significant effect of the food restriction to energy efficiency of milk production in baboon and rats. In the first trimester of pregnancy, estrogen and progesterone are secreted from the ovaries with stimulation of human chorionic-gonadotrophin originating from the placenta [38]. The circulating estrogen levels are elevated by approximately 100-folds in pregnancy and increase with gestational age [39]. The levels of sub-types of estrogen, i.e., estradiol, estrone, estriol, and estetrol, also increase [39]. During pregnancy, the estradiol levels are associated with consecutive pregnancies of the same woman [40]. Increased estradiol levels cause the plasma volume to increase and the up and downregulation of metabolizing enzymes and hepatic production of certain proteins. It improves binding of corticosteroids, sex steroids, thyroid hormones, and vitamin D to proteins [41, 42].

1.2. Effect of the Pregnancy and Lactation on the Longevity of Women

The effect of giving birth to babies and lactation on the longevity of women is ambiguous; there are conflicting observations in the literature, a negative relationship was reported by [43]. Smith et al [44], after employing the data available in the Utah Population Database regarding 13,987 couples married between 1860-1899 concluded that the women with fewer children as well as those bearing children late in life live had longer post-reproductive lives. Lycett et al [45] reported that the married women who did not give birth to babies did not live longer than the women who had babies and the women who had a few children did not live longer than the women who had many children, but reported

a trade-off between reproduction and longevity in the poorest social groups. Hsu et al [46] studied the fertility-longevity relationship by employing the data set of 81,924 women and 103,642 men born between 1601 and 1910 in Europe and concluded that higher fertility had a significantly negative effect on longevity and pointed the need for further research due to the multiple mechanisms of human ageing. Present study aims to contribute a thermodynamic opinion to this discussion.

2. Methods
2.1 Calculation of the Calories and the Macronutrients of Pregnancy and Breastfeeding Diets

Dietary Guidelines for Americans 2020-2025 [47] recommend the daily calorie intake range for healthy women aged 19 through 30 to be between 1,800 to 2,400 kcal/day. Trumbo et al [48] state that energy requirements in the first trimester would be the same as for non-pregnant women. During the second and third trimesters, energy needs increase by 340 cal/day (1,421 J/day) and 452 cal/day (1.889 J/day), respectively [49]. Kominiarek and Rajan [42] recommend carbohydrate intake should be 45-64% of the daily calories during pregnancy, and it should consist of 6-9 servings of whole-grain daily, and 20 to 35 % of the daily calories should be obtained from the healthy fats. The amount of protein intake should be increased by 25 g/day during the second and the third trimesters [48] and the breastfeeding period. Elango and Ball (2016) recommended the average daily protein intake for early and late pregnancy as 79 and 108 g/day, representing between 14-18% of the daily calories. Energy requirement (ER) during pregnancy and the lactation period for the 19–50 years old women were estimated by following the recommendations of Trumbo et al [48] and presented in Table 1.

Table 1. ER (daily energy requirement) of the pregnant or the lactating women, when calculated as the (ER of the non-pregnant woman) + (additional energy expended during pregnancy) + (energy deposition).

1st trimester: Adult ER + 0 + 0
2nd trimester: Adult ER + 160 kcal (8 kcal/week, approximately for 20 weeks) + 180 kcal = 673 kJ (33 kJ/week, approximately for 20 weeks) + 752 kJ
3rd trimester: Adult ER + 272 kcal (8 kcal/ approximately for 34 weeks) + 180 kcal= 1,137 kJ (33 kJ/week for 34 weeks) + 752 kJ
lactation period: Adult ER of pre-pregnancy + milk energy output
Weight loss calories during the 1st 6 months after pregnancy: ER + 500 kcal– 170 kcal =ER+2090 kJ – 710 kJ

Table 1 implies that in the second trimesters 160 kcal/day (669 kJ/day) plus 180 kcal/day (752 kJ) of calories and in the third trimester, 272 kcal (1,137 kJ) and 180 kcal/day (752 kJ) of calories should be allocated to the pregnant women. One g of fat corresponds to 9 kcal (38 kJ); therefore, in the formulations 180 corresponds to 20 g of daily fat storage by the pregnant women. The diet therapy used in twin and triplet pregnancies is based on diabetic diet treatment, including three main meals and three snacks per day [48]. During twin breastfeeding, an extra maternal calorie intake of 1,200-1,500 kcal/day (5,016-6,270 kJ/day) is required depending on the production of 1.2-2 L of milk/day. The diet should contain 20% protein, 40% fat and 40% carbohydrate, similar

to the twin pregnancy period [51]. It is also recommended that women with twins consume an additional 50 g/day protein at the beginning of the second trimester [49].

For normal-weight women, the diet list was prepared to comply with the recommendations that the twin-pregnancy weight gain will be between 17-25 kg. This recommended weight gain may be slightly lower for overweight women with 14-23 kg and for obese women with 11-19 kg [52]. The weight gains during pregnancy include the approximate weights of the placenta (1 kg), babies (2.5 kg each), amniotic fluid that surrounds the baby in the womb (1 kg), enlargement of the uterine (1 kg), enlargement of the breast tissue (2 kg), increase in the blood (2 kg), maternal tissue fluids (2 kg) and the rest may be maternal tissue fat stores. Their diet may consist of 20% proteins, 40% carbohydrates, and 40 % fats [48]. The lower carbohydrate percentage provides better glycemic control, and the higher the fat rate provides more calories with less bulk. Low glycemic index carbohydrates in the diet content prevent wide fluctuations in blood glucose concentrations [53]. It was argued that the adequate daily intake of 3,500 kcal (14,630 kJ) composed of 350 g of carbohydrate, 175 g of protein, and 156 g of fat per day for normal-weight women with twins [53].

Low-calorie healthy foods generally cost more than energy dense foods [49,53]; therefore, poor pregnant women are more likely to choose high carbohydrate-containing, energy-dense foods due to their lower price [54]. Low socioeconomic pregnant women's diet may be 300 kcal (1,254 kJ) lower than the healthy pregnant women's diet. The diet of the poor women may consist of 55-60 % carbohydrates, 15-20 % proteins, and 30 % lipids (Rajikan, et al (2017). In poverty, singleton and twin pregnancy diets are 300 kcal (1,254 kJ) less than the diets of a normal healthy pregnant woman. The percentage of macronutrients in the diet; is set to be 55-60% carbohydrate, 15-20% protein, and 30% fat [54]. Nutritional values of the foods used in the menus are taken from USDA Food Composition Data [55].

2.2 Thermodynamic Considerations

Calculations presented in this study consider a 30 years old pregnant woman having her first pregnancy; four different types of diets are designed for each trimester and lactation. A thermodynamic system describing a pregnant or a lactating woman is described in Figure 1.
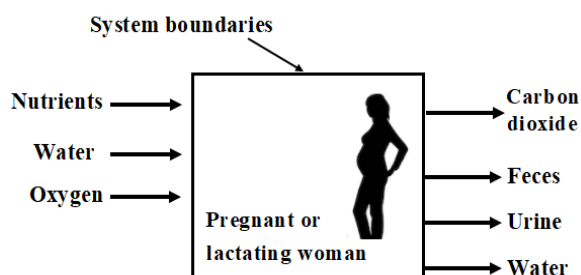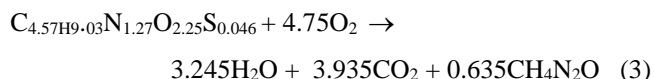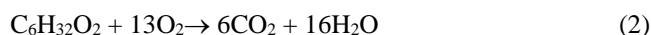

Figure 1. Schematic description of the thermodynamic system boundaries of pregnant woman. Nutrients, water and O_2 are the inputs of the system and products of the metabolism, i.e., water, carbon dioxide and urine and feces are exiting the system.

Equations (1)-(5) are related only with what is happening within the system boundaries, e, g., the woman and the baby. The rest of the universe is outside of the system boundaries and are not the subject of our analyses. For the calculations of total input and output in the body:

$$C_6H_{12}O_6 + 6O_2 \rightarrow 6H_2O + 6CO_2 \tag{1}$$

$$C_6H_{32}O_2 + 13O_2 \rightarrow 6CO_2 + 16H_2O \tag{2}$$

$$C_{4.57}H_{9\cdot03}N_{1.27}O_{2.25}S_{0.046} + 4.75O_2 \rightarrow$$
$$3.245H_2O + 3.935CO_2 + 0.635CH_4N_2O \tag{3}$$

Glucose represents carbohydrates, palmitic acid represents lipids, and a mixture of 20 amino acids represents proteins. They are metabolized in the body via O_2, and they leave as H_2O, CO_2, and urea (CH_4N_2O). Equations (4) and (5) describe the enthalpy and entropy change of the metabolic reactions and neglect the heat released from the body. Enthalpy change upon the metabolism of glucose, $\Delta h_{metabolism}$, was actually enthalpy change of reaction (1) and calculated as

$$\Delta h_{metabolism} = 6\Delta h_{f,CO2} + 6\Delta h_{f,H2O} - \Delta h^o_{f,C6H12O6} -$$
$$6\Delta h^o_{f,O2} \tag{4}$$

where, $\Delta h_{f,CO2}$ and $\Delta h_{f,H2O}$ are the enthalpies of formation of the metabolic products at the body temperature (37 °C), and $\Delta h^o_{f,C6H12O6}$ and $\Delta h^o_{f,O2}$ are the enthalpy of formation of the reactants at room temperature (25°C). Thermodynamic data are presented in Table 2.

Specific entropy generation rate from the metabolism of glucose was:

$$\Delta \dot{s}^o_{rxn} = 6\dot{s}^o_{CO2} + 6\dot{s}_{H2O} - \dot{s}^o_{C6H12O6} - 6\dot{s}^o_{O2} \tag{5}$$

where, $\dot{s}_{CO2}$ and $\dot{s}_{H2O}$ are the absolute entropy exit rates of the products at body temperature from the metabolism, and $\dot{s}^o_{C6H12O6}$ and $\dot{s}^o_{O2}$ are the absolute entropy entrance rates of the reactants at room temperature to metabolism. Equation (5) refers to entropy of the reaction for carbohydrate as described in Eq (1). Similar calculations as those of equations (4) and (5) were also done for the lipid and amino acid utilization in the energy metabolism by replacing the thermodynamic properties of glucose with those of palmitic acid and average amino acid, respectively. We have carried out the calculations for 30 years old healthy and moderately active women. As seen in Table 3, the first, second, third trimester and breastfeeding diet calories employed in this study are 2,000 kcal/day (8,360 kJ/day); 2,350 kcal/day (9,823 kJ/day); 2,450 kcal/day (10,617 kJ/day), and 2,330 kcal/day (9,739 kJ/day), respectively. Diet lists were prepared according to the dietary guidelines presented in the references [48, 49, 51]; then the nutrients provided by these diets are presented in Table 3 to establish the basis for further calculations. In Table 3, if one adds the uptakes and subtracts the amount of products of the metabolism, there would be no mass conservation, since the difference is employed to synthesize the babies and the changes occurring in the body of the mother. The term calculated with equation 5 is actually the rate of entropy change of the chemical reactions representing the human metabolism. Considering the standard definitions of classical thermodynamics, this term would equal the rate of entropy generation only in stationary processes, also neglecting any heat flows. In Table 3, all the women were assumed consuming 2.L of water, every day

and wealthy and the poor women may not be from the same country.

3. Results and Discussion

In the present study, recommendations of the nutritionists are considered while formulating the diets; therefore, all the cases (with the exception of the nutrition of the poor women in case of twin pregnancy) discussed in this study actually lead to optimal entropy generation rates as described in Table 4. Entropy generation reported in this study is actually those of the metabolic reactions. Increase in the weight of the fetus would be the result of larger amounts of nutrients entering in these reactions; therefore, cause an increase in entropy generated by the pregnant women. The fetus gains weight as we go from the first trimester to the second and then to the third trimester Table 4 shows the associated increase in the entropy generation.

Poor women consume more carbohydrate than the recommended level; therefore, their entropy generation rate is not optimal. By following the same procedure as Öngel et al. [29], a telomere length-based energy efficiency factor η is employed while calculating the entropy generation in each stage of the pregnancy and lactation as:

$$\text{Entropy generation rate in each group} = \dot{\Delta s}_{rxn}/\eta \qquad (6)$$

and then the total pregnancy and the lactation period entropy generation is calculated as:

total pregnancy and lactation period entropy $=$

$$\sum(\dot{\Delta s}_{rxn}/\eta)_i(time\ length\ of\ the\ increment) \ (7)$$

where, $\dot{\Delta s}_{rxn}$ is the nutrition-related entropy generation calculated based on equation (5) for carbohydrates or its equivalents for lipids or proteins. Equations (6) and (7), in agreement with the disposable soma theory which states that when the organisms have limited resources the entropy-accumulated, e.g., the damage collected, building blocks, are recycled, by doing so the cells may both get rid of the defective building elements and reuse the energy stored there. According to the Merriam Webster dictionary, "soma" means a part of the body. Although telomere lengths may not have direct correlation with energy efficiency, the shortening of the telomeres goes parallel with the decrease in the energy efficiency.

Telomere length data were adapted from Huang et al [56], as presented in Table 4. The percentage of the entropy generated in the pregnancy and lactation period, when compared to the non-pregnant woman's lifespan entropy is presented in Table 5. In the case of singleton pregnancy, eating less, e.g., in reasonable amounts, leads to smaller amounts of entropy generation; therefore, may be cherished, but in the case of twin pregnancy, eating non-nutritious food in insufficient amounts is something to be avoided. Placenta plays a major role in hormone production during pregnancy [57]. In multiple pregnancies, placental lactogen and progesterone hormone secretion increase more than that of a singleton pregnancy. An increase in these hormones affects glucose metabolism, thus increases the risk of gestational diabetes mellitus and insulin resistance [40].

Multiple pregnancies involve significant maternal physiological changes, including increased plasma volume, increased resistance to carbohydrate metabolism, and increased basal metabolic rate [58]. Only 3% of all births are multiple pregnancies but they account for 20% of low birth-weight (less than 2,500 g) and 19–24% of very-low-birth-weight (less than 1,500 g) and for 15% of preterm births in the United States [58]. In twin pregnancy, especially in the second half of pregnancy glycogen stores are depleted faster [52].

Maternal resting energy expenditure increases by 10% in twin pregnancies than singleton pregnancies [58]. The diet lists of this study were prepared to address this information. The results of this study should be interpreted with caution, in case of sarcopenia or famine human body may consume its own building blocks in its energy metabolism and such an experience do not extend the lifespan. On the other hand, Ulu et al [59] showed that intermittent caloric restriction via skipping a meal for 30 days in a year without increasing the caloric content of other meals might extend the life span approximately 3%. A high-entropy generation process shortens the expected longevity more than a low-entropy generation process, as evidenced in Table 5. In twin pregnancy, entropy generated in the first trimester is 235 kJ/(kg K) corresponding to 2.1% of the lifespan entropy limit of the non-pregnant woman, whereas entropy generation by non-pregnant women in the same period is 135 kJ/(kg K), corresponding to 1.2% of her lifespan entropy limit. Metabolic entropy generation is not necessarily based on the externally provided nutrients. In case of famine or sarcopenia, human body consumes its own building blocks in its energy metabolism and generate entropy [60]. Such an experience does not contribute to entropy generation only, but also damages the muscles and decreases the muscle work efficiency η_{II} defined in equation 11. Helle and Lummaa [61] after analyzing the data collected in pre-industrial Finland, where conditions were similar to pregnancy and lactation in poverty, reported that the decrease in longevity of the women was related with the number of the pregnancies they had. Since the baby boys had higher body weight at birth than the baby girls, more energy is needed to synthesize them than what is needed for the baby girls; therefore, more entropy is generated in the pregnancies for the baby boys. The decrease in the longevity of the mothers was more striking in the mothers of the baby boys, when compared to those of the baby girls.

The oxidation reaction involves "shuffling" of electrons of the nutrient atoms with those of the oxidizing agent, oxygen, which serve as electron acceptor. Recently the relation between numbers of electron moles transferred to oxygen per mole of fuel is shown to be 4 times of the stoichiometric moles for C-H-O-S fuels [62]. Thus, for carbohydrates, it is 24 electrons/mole; for fat, it is 92 electrons/mole. Each electron mole transfers results in release of 111 kJ/electrons mole [63]. Thus, protein has low metabolic efficiency (η=10 %) compared to carbohydrates (almost η=40 %) and fat; therefore, causes higher entropy generation. Protein is used mainly for bodybuilding or replacing cells. Longevity may be assed according to the Rubner's hypothesis [64] based on the first law limit or according or according to the Silva's hypothesis, which is based on the second law of thermodynamics. In the present study, the second law analyses are performed. This study was formulated with the same principles as those of Öngel et al [29], Yildiz et al [65,66] and Semerciöz et al [67] and offers thermodynamic assessment to the issue of whether pregnancy affects longevity of the women or not. Todhunter et al [68] achieved documenting the consequences of entropy accumulation in the tissues visually.

Heat released from the body was neglected while establishing equations (4) and (5), based on our discussion of exergy balance in reference [67]. Exergy balance is the of the other way of making second law analysis is as:

$$\sum_{in}[\dot{N}\,ex]_{in} - \sum_{out}[\dot{N}\,ex]_{out} - \sum_{i}[1 - (T_s/T_{b,i})]\,\dot{Q}_i -$$

$$\dot{W} - \dot{Ex}_{dest} = d[N\,ex]_{system}/dt \quad (8)$$

when exergy accumulates in the system slowly the right hand side of the equation may be neglected and assumed zero. Traditionally, the *"useful work potential"* of the metabolic heat discarded from the body is assessed in terms of its work potential in a Carnot engine operating between the system and the environment temperatures as "$\dot{W} = \dot{Q}[1 - (T_r/T_b)]$" where, T_b is 310.15 K, i.e., the body temperature on its surface and T_s is the room temperature in the immediate surrounding and taken as the average of the body surface (310.15 K) and the room (298.15 K) temperatures. In the assessments with pregnant mice, the calculated magnitude of $\dot{W}$ was very small; therefore, considered *"not useful for performing work"* [67], implying that neglecting the heat released from the body, do not actually cause a considerable error in the present study. In the present study, entropy generation does not result in increase in the entropy of the body since the body is at steady state. It is like hot water kettle where electric input overcomes heat loss and maintain water at steady temperature. Entropy generated is flushed out. Entropy of water remains constant since water is at steady temperature. However, entropy generated within the body is due to electron transfer and hence the reactive oxidative species damage keeps occurring in proportion to entropy generated [62]. In the present study the telomere shortening was considered within the context of the disposable soma theory and not elaborated further. But, in the literature estrogen levels are reported to be increasing during the pregnancy [39] and their levels are related with the telomere lengths [69].

4. Conclusion

Our assessment recommends strongly that the women should choose their diets carefully during pregnancy and the lactation stages of their lives to minimize their metabolic entropy generation rates to avoid filling up their lifespan entropy generation limit. Based on the diets designed exclusively for each of them, our assessments showed that a wealthy woman in a singleton pregnancy may generate 1.5% and in the case of twin pregnancy 2.1% of the total lifespan entropy generation by a non-pregnant wealthy woman. A poor woman may generate in the case of the singleton pregnancy 1.8% and in case of the twin pregnancy 2.1% of the total lifespan entropy generated by a wealthy woman. It should be remembered here that; in the multiple pregnancies the babies are usually smaller when compared to those of the singleton pregnancies. If the lifespan of the women should be determined exclusively by the entropic age concept; longevity may exceed 100 years. Under these circumstances the percentages, which are presented here to quantify the effect of the pregnancy and lactation on the lifespan of the women does not appear to be significantly different from each other. Therefore, we may conclude that if the pregnant and the lactating women should have diets designed by knowledgeable nutritionists according to the scientific nutritional recommendations and guidelines. In such a case, the number of the pregnancies they have may not decrease their expected lifespan. In real life, women may not stick to such diet lists; therefore, there may be fluctuations in the observed longevities. The small differences, which are calculated in the present study, may actually explain the reason for conflicting longevity and fertility relations reported in the previous studies.

Table 2. Thermodynamic properties of the nutrients and the products of the metabolism at 1 atm (adapted from Kuddusi, [27]). Where h_i^o describes the specific enthalpy of formation of the reactants of the metabolism at 273 K, $h_{i,298 K}$ describes the specific enthalpy of formation of the reactants of the metabolism at body temperature; s_i^o and $s_{i,310 K}$ are the absolute entropies of the reactants of the metabolism under the standard conditions and those of the products of the metabolism at the body temperature.

Nutrient	h_i^o (kJ/kmol) at 273 K	$h_{i,298 K}$ (kJ/kmol)	$h_{i,310 K}$ (kJ/kmol)	s_i^o (kJ/kmol K) at 273 K	$s_{i,310 K}$ (kJ/kmol K) at 310 K
Glucose ($C_6H_{12}O_6$)	-1260×10^3	-	-	212	
Palmitic acid ($C_{16}H_{32}O_2$)	-835×10^3	-	-	452.4	
Average amino acid ($C_{4.57}H_{9.03}N_{1.27}O_{2.25}S_{0.046}$)	-385×10^3	-	-	1.401×119	
O_2		8,682	-	218.0	
H_2O		9,904	-	215.5	219
CO_2			9,807	240.4	243.6
N_2			9,014		193.7

Table 3. Calories, the composition of the uptake of the nutrients of and the excreted feces and the urine with each diet in the cases of the pregnancy and lactation of wealthy and poor women for singleton and twin pregnancies.

	1st trimester diet		2nd trimester diet		3rd trimester diet		lactation diet	
	Singleton baby	Twin babies	Singleton baby	Twin babies	Singleton baby	Twin babies	Singleton baby	Twin babies
	WEALTHY WOMEN							
Nutrients uptake	2,000 kcal/day (8,360 kJ/day)	2,000 kcal/day (8,360 kJ/day)	2,350 kcal/day (9,838 kJ/day)	3,300 kcal/day (13,794 kJ/day)	2,450 kcal/day (25,090 kJ/day)	3,450 kcal/day (14,421 kJ/day)	2,330 kcal/day (9,838 kJ/day)	3,500 kcal/day (14630 kJ/day)
Carbohydrate (g/day)	317	200	331	324	329	348	339	362
Fat (g/day)	52	84	75	138	83	154	66	169
Protein (g/day)	73.6	105	96.6	128	100	175	103	149
O_2 (g/day)	581.5	596	692	904	717.5	1,037	683	1,060
H_2O (g/day)	285	270	330	412	340	468	328	480
CO_2 (g/day)	715	687	832	1,039	857	1,188	828.6	1,210
Feces (g/day)	1,347	840	980	480	921	1,438	877	142
Urine (g/day)	1,201	1,719	1,576	2,086	1,636	2,852	1,681	2,432
	POOR WOMEN							
Nutrients uptake	1,700 kcal/day (7,106 kJ/day)	1,700 kcal/day (7,106 kJ/day)	2,050 kcal/day (8,569 kJ/day)	2,800 kcal/day (11,704 kJ/day)	2,150 kcal/day (8,569 kJ/day)	3,000 kcal/day (12,500 kJ/day)	2,050 kcal/day (8,569 kJ/day)	3,200 kcal/day (13,376 kJ/day)
Carbohydrate (g/day)	271	271	260	397	292	398	267	460
Fat (g/day)	47	47	73	85	66	96	75	105
Protein (g/day)	50	50	109	129	83	119	72	98
O_2 (g/day)	488	488	627	832	607	852	592	917
H_2O (g/day)	240	240	292	397	290	405	280	442
CO_2 (g/day)	599	599	741	1,003	730	1,020	702	1,105
Feces (g/day)	1,787	1,787	774	465	1,200	627	1,377	965
Urine (g/day)	810	810	1,786	2,101	1,350	1,936	1,171	1,591

Table 4. Telomere length (relative units) and entropy generation rate (kJ/K kg) in each trimester and the lactation period.

	1st trimester	2nd trimester	3rd trimester	Lactation period
	Normal pregnancy for a singleton baby			
Telomere length	1.40	1.57	1.57	1.41
Entropy generation rate	2.70×10^{-6}	2.88×10^{-6}	2.98×10^{-6}	3.20×10^{-6}
Entropy generated in pregnancy and lactation	171			

	Tubal pregnancy for a singleton baby			
Telomere length	1.54	1.43	1.43	1.47
Entropy generation rate	2.46×10^{-6}	3.16×10^{-6}	3.27×10^{-6}	3.07×10^{-6}
Entropy generated in pregnancy and lactation	171			
	Normal pregnancy for twin babies			
Telomere length	1.40	1.57	1.57	1.41
Entropy generation rate	2.83×10^{-6}	3.71×10^{-6}	4.35×10^{-6}	4.84×10^{-6}
Entropy generated in pregnancy and lactation	235			
	Tubal pregnancy for twin babies			
Telomere length	1.54	1.43	1.43	1.47
Entropy generation rate	2.57×10^{-6}	4.08×10^{-6}	4.77×10^{-6}	4.64×10^{-6}
Entropy generated in pregnancy and lactation	235			
	Normal pregnancy in poverty for a singleton baby			
Telomere length	1.4	1.57	1.57	1.41
Entropy generation rate	2.22×10^{-6}	$2{,}67\times10^{-6}$	2.52×10^{-6}	$2{,}69\times10^{-6}$
Entropy generated in pregnancy and lactation	146			
	Normal pregnancy in poverty for twin babies			
Telomere length	1.4	1.57	1.57	1.41
Entropy generation rate	2.22×10^{-6}	3.50×10^{-6}	3.53×10^{-6}	4.13×10^{-6}
Entropy generated in pregnancy and lactation	201			
	Tubal pregnancy in poverty for a singleton baby			
Telomere length	1.54	1.43	1.43	1.47
Entropy generation rate	2.02×10^{-6}	$2{,}92\times10^{-6}$	$2{,}76\times10^{-6}$	$2{,}58\times10^{-6}$
Entropy generated in pregnancy and lactation	146			
	Tubal pregnancy in poverty for twin babies			
Telomere length	1.54	1.43	1.43	1.47
Entropy generation rate	2.02×10^{-6}	3.84×10^{-6}	3.88×10^{-6}	3.97×10^{-6}
Entropy generated in pregnancy and lactation	201			
	A non-pregnant woman, generating entropy in a similar period		A man generating entropy in a similar period	
Telomere length	1.41	1.47	1.42	1.49
Entropy generation rate	2.46×10^{-6}	2.36×10^{-6}	3.52×10^{-6}	3.35×10^{-6}
Entropy generated in pregnancy and lactation	135		1.94	

Table 5. Total and percentage of the entropy generated in the pregnancy and lactation period when compared to the non-pregnant woman's lifespan entropy. We performed the calculations according to the dietary guidelines [48], which do not require a specific weight; the results are applicable to 60 kg, 170 cm tall women.

	Total entropy generation during pregnancy and lactation period [kJ/(K kg woman)]	Percentage of the non-pregnant woman's lifespan entropy (%)	Total entropy generation during pregnancy and lactation period [kJ/(K kg woman, kg)]	Percentage of the non-pregnant woman's lifespan entropy (%)
	NP		TP	
Singleton pregnancy	171	1.5	171	1.5
Twin pregnancy	235	2.1	235	2.1
Singleton pregnancy in poverty	146	1.3	146	1.3
Twin pregnancy in poverty	201	1.8	201	1.8
Non-pregnant women	135	1.2		
Men	194	1.7		

Nomenclature

h_i^o *specific enthalpy of formation at 273 K,* (kJ/kmol)

$h_{i,298\,K}$ *specific enthalpy of formation at body temperature* (kJ/kmol)

s_i^o *absolute entropy the standard conditions* (kJ/kmol K)

$s_{i,310\,K}$ *absolute entropy at the body temperature* (kJ/kmol K)

References

[1] O. Toussaint, C. Michels, M. Raes and J. Meracle. "Cellular aging and the importance of energetic factors". *Exp. Gerontol..* 30(1), 1-22, 1995; *doi:10.1016/0531-5565(94)00038-5.*

[2] T. Nyström., "A bacterial kind of aging". *PloS Genet..*3(12), 2355-2357, 2007; *doi:10.1371/journal.pgen.0030224.*

[3] J.A. Joseph, N. Denisova, D. Fisher, B. Shukitt-Hale, B. Bickford, R. Prior, and G. Cao. "Age-related neurodegeneration and oxidative stress: putative nutritional intervention." *Neurol Clin* 16(3):747-755, 1998; *doi:10.1016/S0733-8619(05)70092-X.*

[4] H. Giese, W.K. Snyder, C. van Oostrom, H. van Steeg, M.E.T. Dolle and J. Vijg. "Age related mutation accumulation at lacZ reporter locus in normal and tumor tissues of Trp53-deficient mice". *Mutat. Res.* 514, (1-2), 153-163, 2002; *doi:10.1016/s1383-5718(01)00329-1.*

[5] M.G. Kosmadaki and B.A. Gilhrest. "The role of telomeres in skin aging/photoaging". *Micron*, 35(3), 155-159, 2004; *doi:10.1016/j.micron.2003.11.002.*

[6] S. Sandal, B. Yilmaz, and D.O. Carpenter. "Genotoxic effects of PCB 52 and PCB 77 on cultured human peripheral lymphocytes". *Mutat. Res.,* 654, 88-92, 2008; *doi:10.1016/j.mrgentox.2008.05.005.*

[7] A. Salminen, and K. Kaarniranta, K. "Genetics vs. entropy: longevity factors suppress the NF-κB-driven entropic aging process". *Ageing Res. Rev.* 9(3),298-314,2010; *doi:10.1016/j.arr.2009.11.001.*

[8] F. Mete, E. Kilic, A. Somay, A. and Yilmaz, B. (2012). "Effects of heat stress on endocrine functions and behaviour in the pre-pubertal rats". *Indian J. Med. Res.,* Feb., 135, 233-239.

[9] P.C.W. Davies, E. Rieper and J.A. Tuszynski, J.A. "Self-organization and entropy reduction in a living cell". *BioSystems,* 111(1), 1-10, 2013; *doi:10.1016/j.biosystems.2012.10.005.*

[10] P. Lenart and J. Bienertova-Vasku (2016). Double strand breaks may be a missing link between entropy and aging. *Mech. Ageing Dev.* 157, 1-6, 2016; *doi:10.1016/j.mad.2016.06.002.*

[11] A.J. Hulbert, R. Pamplona, R. Buffenstein, et al. "Life and death: Metabolic rate, membrane composition, and life span of animals." *Physiol Rev*, 87(4):1175-1213, 2007; *doi:org/10.1152/physrev.00047.2006.*

[12] T. Farooqui and AA. Farooqui AA. "Aging: an important factor for the pathogenesis of neurodegenerative diseases." *Mech Ageing Dev,* 130(4):203-215, 2009; *doi:org/10.1016/j.mad.2008.11.006.*

[13] C. Yildiz V.A. Bilgin, B. Yilmaz and Özilgen M. "Organisms live at far-from-equilibrium with their surroundings while maintaining homeostasis, importing exergy and exporting entropy." *Int J Exergy*, 31(3): 287-300, 2020; *doi:10.1504/IJEX.2020.106457.*

[14] L Hayflick. "Aging: The reality: "Anti-aging" is an oxymoron." *J. Gerontol. A Biol. Sci. Med. Sci.* 59(6): B573–B578, 2004; *doi:org/10.1093/gerona/59.6.B573.*

[15] L. Hayflick. "Biological aging is no longer an unsolved problem." *Ann. NY Acad. Sci.* 1100 (1): 1–13,2007; *doi:10.1196/annals.1395.001.*

[16] L. Hayflick. "Entropy explains aging, genetic determinism explains longevity, and undefined terminology explains misunderstanding both." *PloS Genet.* 3(2): 2351-2354, 2007; *doi:10.1371/journal.pgen.0030220.*

[17] C.A. Silva and K. Annamalai. "Entropy generation and human aging: Lifespan entropy and effect of physical activity level." *Entropy*, 10: 100-123, 2008; *doi:org/10.3390/entropy-e10020100.*

[18] C.A. Silva and K. Annamalai. "Entropy generation and human aging: lifespan entropy and effect of diet composition and caloric restriction diets," *J. Thermodyn.* 2009(186723), 1-10, 2009; *doi:10.1155/2009/186723.*

[19] K. Annamalai and C.A. Silva. "Entropy stress and scaling of vital organs over life span based on allometric laws." *Entropy* 14(12): 2550e77, *2012; https://doi.org/10.3390/e14122550.*

[20] E. Schrödinger. "What is life? The physical aspects of a living cell". Cambridge University Press, Cambridge, 1944.

[21] I. Prigogine, J. Wiame. "Biologie et thermodynamique des phénomènes irréversibles." *Experientia*, 2(11): 451-453, 1946*; doi:10.1007/BF02153597.*

[22] B.H. Yalçınkaya, **S.** Genc, J. Çatak, M. Özilgen and B. Yilmaz. "*Mitochondrial Energy Conversion*" in "*Comprehensive Energy Systems*" I. Dincer, (Editor), Elsevier, February 21, 2018.

[23] R. Jumpertz, R.L. Hanson, M.L. Sievers, P.H. Bennet, R.G. Nelson and J. Krakoff." Higher energy expenditure in humans predicts natural mortality." *J. Clin. Endocrinol. Metab.,* 96(6): E972-976, 2011; *doi:10.1210/jc.2010-2944.*

[24] C.K. Martin, L.K. Heilbronn, L. de Jonge, J.P. DeLany, J. Volaufova, S.D. Anton, L.M. Redman, S.R. Smith and E. Ravussin. "Effect of calorie restriction on resting metabolic rate and spontaneous physical activity." *Obesity (Silver Spring)*; 15(12):2964-2973, 2007; *doi: 10.1038/oby.2007.354.*

[25] S.B. Roberts, P. Fuss, W.J. Evans, M.B. Heyman and V.R. Young. "Energy expenditure, aging and body composition." *J. Nutr.*123(2 suppl):474-480, 1993; *doi:10.1093/jn/123.suppl_2.474.*

[26] L. Fontana. "The scientific basis of caloric restriction leading to longer life." *Curr. Opin. Gastroenterol.,* 25:144-150, 2009; *doi:10.1097/MOG.0b013e32831ef1ba.*

[27] L. Kuddusi. "Thermodynamics and life span estimation." *Energy;* 80:227-238, *2015; doi:org/10.1016/j.energy.2014.11.065.*

[28] A.K. Patel and S.P.S. Rajput. "Thermodynamic life cycle assessment of humans with considering food habits and energy intake." *Saudi J. Biol. Sci.* 28:531-540, 2021; *doi:org/10.1016/j.sjbs.2020.10.038.*

[29] M.E. Öngel, C. Yildız, C. Akpınaroğlu, B. Yilmaz, M. Özilgen. "Why women may live longer than men do? A telomere-length regulated and diet-based entropic assessment." *Clin. Nut.* 40(3): 1186-1191, 2020; *doi:10.1016/j.clnu.2020.07.030.*

[30] R.J. Hodes. "Telomere length, aging and somatic cell turnover." *J. Exp. Med.,* 190(2): 153–156, 1999; *doi:10.1084/jem.190.2.153.*

[31] A. Müezzinler, A.K. Zaineddin and H.A. Brenner "Systematic review of leukocyte telomere length and age in adults." *Ageing. Res. Rev.,* 12(2): 509-519, 2013; *doi:10.1016/j.arr.2013.01.003.*

[32] C. Massafra, D. Gioia, C. De Felice, E. Picciolini, V. De Leo, M. Bonifazi and A. Bernabei. "Effects of estrogens and androgens on erythrocyte antioxidantsuperoxide dismutase, catalase and glutathione peroxidase activities during the menstrual cycle." *J. Endocrinol.,* 167, 447–4522000; *doi:10.1677/joe.0.1670447.*

[33] T.L.B. Kirkwood. "Evolution of ageing, *Mechanisms of ageing and development."* 123 (7): 737-745, 2002; *doi:org/10.1016/S0047-6374(01)00419-5.*

[34] S. Casagrande and M. Hau. "Telomere attrition: Metabolic regulation and signalling function?" *Biol. Lett.,* 15(3): 20180885, 2019; *doi:10.1098/rsbl.2018.0885.*

[35] D.T.A. Eisenberg. *"*An evolutionary review of human telomere biology: The thrifty telomere hypothesis and notes on potential adaptive paternal effects.*" Am. J. Hum. Biol*., 23(2): 149–167, 2011; *doi:org/10.1002/ajhb.21127.*

[36] S.B. Roberts and W.A. Coward. "Lactation increases the efficiency of energy utilization in rats." *J. Nutr.*, 114(12):2193-200, 1984; doi:10.1093/jn/114.12.2193.

[37] S.B. Roberts, T.J. Cole and W.A. Coward. "Lactational performance in relation to energy intake in baboon." *Am. J. Clin. Nutr.*, 41(6):1270-1276, 1985; *doi:10.1093/ajcn/41.6.1270.*

[38] Knopp HR. Hormone-mediated changes in nutrient metabolism in pregnancy: A physiological basis for normal fetal development, *Ann NY Acad Sci,* 1997;817, 251-271; *doi:10.1111/j.1749-6632.1997.tb48212.x.*

[39] L. Bernstein, L. Lipworth, R.K. Ross and D. Trichopoulos. "Correlation of estrogen levels between successive pregnancies." *Am. J. Epidemiol.,* 142(6), 625-628, 1995; *doi:10.1093/oxfordjournals.aje.a117685.*

[40] M.E. Rosello-Soberon, L. Fuentes-Chaparro and E. Casanueva. "Twin pregnancies: Eating for three? Maternal nutrition update." *Nutr. Rev.* 63(9), 295–302, 2005; *doi:10.1111/j.1753-4887.2005.tb00144.x.*

[41] F.J. Darne, H.H. McGarrigle and G.C. Lachelin. "Diurnal variation of plasma and saliva oestrogen, progesterone, cortisol and plasma dehydroepiandrosterone sulphate in late pregnancy." *Eur. J. Obstet. Gynecol. Reprod. Biol.,* 32(2): 57-66, 1989; *doi:10.1016/0028-2243(89)90184-6.*

[42] M.A. Kominiarek and P. Rajan. "Nutrition recommendations in pregnancy and lactation." *Med. Clin. North Am.*, 100 (6): 1199–1215, 2016; *doi:10.1016/j.mcna.2016.06.004.*

[43] R.G.J. Westendorp and T.B.L. Kirkwood "Human longevity at the cost of reproductive success." *Nature*, 396, 743-746, 1998; *doi:10.1038/25519.*

[44] K.R. Smith, G.P. Mineau and L.L. Bean "Fertility and post-reproductive longevity." *Soc. Biol.* 49(3-4):185–205, 2010; *doi:10.1080/19485565.2002.9989058*

[45] J.E. Lycett, R.I.M. Dunbar and E. Voland. "Longevity and the costs of reproduction in a historical human population." *Proc. R. Soc. Lond. B Biol Sci*, 267(1438):31-35, 2000; *doi:10.1098/rspb.2000.0962.*

[46] C-H. Hsu, O. Posegga, K. Fischbach and H. Engelhardt. "Examining the trade-offs between human fertility and longevity over three centuries using crowdsourced genealogy data." *PLoS One,* 16(8): e0255528, 2021; *doi:10.1371/journal.pone.0255528*

[47] DGA. "2020-2025 dietary guidelines for Americans," US Department of Health and Human Services and US Department of Agriculture, December 2020.

[48] P. Trumbo, S. Schlicker and Yates AA, et al. "Food and Nutrition Board, Institute of Medicine: Dietary reference intakes for energy, carbohydrate, fiber, fat, fatty acids, cholesterol, protein, and amino acids." National Academies Press Washington, DC, 2002.

[49] P. Monsivais and A. Drewnowski. "The rising cost of low-energy-density foods." *J. Am. Diet. Assoc.* 107(12), 2071-2076, 2007; *doi:10.1016/j.jada.2007.09.009.*

[50] R. Elango and R.O Ball. "Protein and amino acid requirements during pregnancy." *Adv. Nut.* **7**(4), 839S-844S, 2016; *doi:org/10.3945/an.115.011817).*

[51] IOM and NRC. Institute of Medicine (US) and National Research Council (US) Committee to reexamine IOM pregnancy weight guidelines. "Weight gain during pregnancy: Reexamining the guidelines." K.M. Rasmussen and A.L. Yaktine. (editors). National Academies Press, Washington DC, 2009.

[52] B. Luke. "Nutrition and multiple gestation." *Semin. Perinatol,* 29, 349-354; 2005; *doi:10.1053/j.semperi.2005.08.004.*

[53] S. Kish. "Healthy, low calorie foods cost more on average," available at *https://naldc.nal.usda.gov/download/15381/PDF*; accessed February 6, 2021.

[54] R. Rajikan, N.S.A. Zaidi, S.M. Elias. "Construction of healthy and palatable diet for low socioeconomic female adults using linear programming." *Int J Adv Sci. Eng. Inf. Techno.* **7**(1), 125-131, 2017; *doi:10.18517/ijaseit.7.1.1191.*

[55] USDA (2021). "Food composition database." Available at *https://fdc.nal.usda.gov*; accessed: 03.02.2021.

[56] Z. Huang, X, Zhao, H. Zhang, G. Liang, H. Qi, X. He C, Zhu, S. Ge and J. Zhang. "The association between mitochondrial DNA copy number, telomere length, and tubal pregnancy." *Placenta,* 97: 108–114, 2020; *doi:10.1016/j.placenta.2020.06.017.*

[57] T. Napso, H.E.J. Yong, J. Lopez-Tello, and A.N. Sferruzzi-Perri AN. "The role of placental hormones in mediating maternal adaptations to support pregnancy and lactation." *Front. Physiol.* 9(1091), 1-39, 2018; *doi:10.3389/fphys.2018.01091.*

[58] W. Goodnight and R. Newman. "Optimal nutrition for improved twin pregnancy outcome." *Obstet Gynecol*, 114 (5), 1121-1134, 2009; *doi:10.1097/AOG.0b013e3181bb14c8.*

[59] G. Ulu, A.S. Semerciöz, and M. Özilgen. ˝Energy storage and reuse in biological systems: Case studies.˝ *Energy Storage*, e253, 2021; *doi:org/10.1002/est2.253.*

[60] A.J. Cruz-Jentoft, G. Bahat, J. Bauer J. et al. "Sarcopenia: Revised European consensus on definition and diagnosis." *Age Ageing,* 48(1), 16–312, 2019; *doi:10.1093/ageing/afy169.*

[61] S. Helle and V. Lummaa. "A trade-off between having many sons and shorter maternal post-reproductive survival in pre-industrial Finland." *Biol. Lett*, 9, 20130034, 2013; *http://dx.doi.org/10.1098/rsbl.2013.0034.*

[62] K. Annamalai. "Oxygen deficient (OD) combustion and metabolism: Allometric laws of organs and Kleiber's law from OD metabolism?" *Systems* 9, 54, 2021; *doi:org/10.3390/systems 9030054.*

[63] M. Popovic. "Thermodynamic properties of microorganisms: Determination and analysis of enthalpy, entropy, and Gibbs free energy of biomass, cells and colonies of 32 microorganism species." Heliyon 5, e0195, 2019; *doi:10.1016/j.heliyon.2019.e01950*

[64] M. Rubner. Machinery of metabolism, *J. Am. Med. Assoc.* 66(24):1879, 1916.

[65] C. Yildiz C, M.E. Öngel, B. Yilmaz, and M. Özilgen. "Diet-dependent entropic assessment of athletes' lifespan." *J. Nutr. Sci.10, E-83, 2021; doi:10.1017/jns.2021.78.*

[66] C. Yildiz, S.A. Semerciöz, B.H. Yalçinkaya, T.D. Ipek TD, E. Ozturk- Isik, and M. Özilgen. "Entropy generation and accumulation in biological systems." *Int J Exergy* 33(4), 444-468, 2020; *doi:10.1504/IJEX.2020.111691.*

[67] A.S. Semerciöz, B. Yilmaz and M. Özilgen. "Thermodynamic assessment of the allocation of the energy and exergy of the nutrients for the life processes during pregnancy. *Br J Nutr* 2020;124(7), 742-753; *doi:org/10.1017/S0007114520001646.*

[68] M.E. Todhunter R.W. Sayaman, M. Miyano and M.A. LaBarge. "Tissue aging: The integration of collective and variant responses of cells to entropic forces over time." *Curr Opin Cell Biol*; 54, 121–129, 2018; *doi:org/10.1016/j.ceb.2018.05.016.*

[69] Y-A. Shin and K-Y Lee. "Low estrogen levels and obesity are associated with shorter telomere lengths in pre-and postmenopausal women" *J Exerc. Rehabil.,* 12(3): 238 – 246, 2016; *doi:org/10.12965/jer.1632584.292.*

Research Article

Thermodynamic Modeling of Liquid-Liquid Equilibrium in Ternary Systems with Biodiesel and Isolated Ester (Methyl Palmitate)

J.K.A. Bezerra[1*] ID, M.R.A Andrade[2] ID, E.R. Silva[2] ID, L.J.N. Duarte [3] ID, G.G. Medeiros[4] ID,
E.L. Barros Neto[2] ID

[1,2] Graduate Chemical Engineering Program, Federal University of Rio Grande do Norte (UFRN), RN, Brazil.
[3] Department of Petroleum Engineering, Federal University of Rio Grande do Norte (UFRN), RN, Brazil.
[4] Departament of Chemical Engineering, Federal University of Rio Grande do Norte (UFRN), RN, Brazil.
Email: [1*] jessycakn@hotmail.com

Abstract

Liquid-liquid equilibrium data were measured and analyzed for two ternary systems (biodiesel + methanol + glycerol and methyl palmitate + methanol + glycerol). Biodiesel, produced by the conventional chemical route at 60 °C for 60 min, using methanol and soybean oil at a molar rate of 10:1 and potassium hydroxide concentration (KOH) of 1 wt% exhibited thermal decomposition at temperatures between 100 and 250 ºC, reaching mass loss of approximately 98.8%, confirming soybean oil conversion into biodiesel by gas chromatography and thermogravimetry. Tie line composition quality was verified using Othmer-Tobias and Hand correlation equations. The distribution and selectivity coefficients were calculated for the immiscibility regions. The experimental tie line data exhibited good correlation in the UNIQUAC and NRTL thermodynamic models. The biodiesel system displayed deviations of 0.66 and 0.53% for the UNIQUAC and NRTL models, respectively. In addition, the methyl palmitate system showed a 1.23 and 0.48% deviation for the UNIQUAC and NRTL model, respectively. The individual behavior of the main biodiesel esters , based on the UNIQUAC model parameters, demonstrated that the type of fatty acid does not interfere in model correlation, likely due to the similarity between their composition and properties.

Keywords: *Liquid-liquid equilibrium; methyl palmitate; biodiesel; UNIQUAC; NRTL; othmer-tobias correlation.*

1. Introduction

The production and indiscriminate use of fossil fuels should decline in the coming decades due to global warming caused by greenhouse gas emissions, which lead to serious climatic disorder. Diversification of the global energy matrix has broadened and strengthened renewable energies and biofuels aimed at combining energy safety with sustainable development [1,2]. Responding to the technical, economic and environmental challenges to diversify the biodiesel-producing processes, the scientific community has conducted extensive research on adding new raw materials and catalysts to the biodiesel production chain aimed at improving its performance and reducing greenhouse gas emissions by transforming an environmental liability into an energy asset [3,4].

Biodiesel is a feasible alternative to diesel owing to its similar properties and applications, without requiring changes to internal combustion engines [5]. It is superior to fossil fuels because of its biodegradable, sustainable and environmentally friendly nature. In addition, its cetane number is higher, it contains practically no sulfur or aromatics and 10-11% oxygen by weight, characteristics that help reduce hydrocarbon emissions, carbon compounds and gases such as sulfur dioxide (SO_2) and nitrogen oxide (NO_X) [6–9].

The conventional biodiesel production route is based on the transesterification reaction of vegetable oils/animal fats, in the presence of an alcohol and catalyst. Biodiesel composition is directly related to the raw material used, conversion rate of the transesterification reaction and separation process efficiency of the resulting products. The compounds commonly found in soybean-based biodiesel include the following fatty acid methyl esters (FAMEs): methyl palmitate, methyl stearate, methyl oleate and methyl linoleate [10]. On an industrial scale, biodiesel production generates multiple impurities, including large amounts of glycerol that may reach 10% of the total, far higher than the market demand for the reuse of this by-product in other processes [11]. In this respect, a number of studies seek ways to optimize the transesterification reaction and reinsert glycerol into new production chains, making the process more economically and environmentally efficient [12,13].

Biodiesel requires a high purity grade and must undergo rigorous purification to prevent traces of glycerol, water, catalyst or alcohol. These products are easily separated by forming two immiscible liquid phases: the heavy (glycerol) and light (biodiesel) phase. Alcohol is also divided into the two phases [14]. In this regard, understanding liquid-liquid equilibrium (LLE) is an indispensable tool to raise the conversion rate of the transesterification reaction with an increase in biodiesel selectivity [15]. On the other hand,

thermodynamic modeling with the excessive use of Gibbs free energy levels, governed by the contribution of functional groups (UNIFAC) or the local composition theory (UNIQUAC, NRTL, among others), is important in predicting phase separation behavior [16–19].

In recent years, a number of studies on experimental data and and thermodynamic modeling involving systems containing biodiesel + glycerol + alcohols were reported in the literature. Nunes et al. [20] assessed experimental data to define miscibility regions and determine parameters for the UNIQUAC model, applying the liquid-liquid equilibrium of sunflower oil biodiesel – methanol – glycerol ternary systems. Bazooyar et al. [21] provided an accurate intelligent model for the behavior of biodiesel – alcohol – glycerol system phases, comparing it with activity models (UNIQUAC). Noriega and Narváez [22] correlated the UNIFAC model from experimental data in order to accurately describe and predict the liquid-liquid equlibrium of the systems involved in the biodiesel process. However, there are few studies on liquid-liquid equilibrium for ternary systems containing pure esters, including ethyl palmitate + ethanol + glycerol [23], methyl oleate + methanol + water [24]. Thus, experimental liquid–liquid equilibrium data of systems involving pure fatty acid esters (such as methyl palmitate) are scarce in the literature, requiring more robust and conclusive studies [25]. In this context, the present study aimed at promoting methylic biodiesel using commercial soybean oil in a homogeneous route with potassium hydroxide (KOH). In addition, the LLE data of the two ternary systems were obtained as follows: system 1 (biodiesel + glycerol + methanol) and system 2 (methyl palmitate + glycerol + methanol). Finally, the experimental data were validated by Othmer-Tobias [26] and Hand [27] correlations and fit to the NRTL and UNIQUAC thermodynamic models.

2. Materials and Methods
2.1 Raw Material
Soybean oil (Soya®), methyl alcohol (Dinâmica Química Contemporânea, 99.8%) and potassium hydroxide (KOH) (Ciavicco®, 88%) were used in the transesterification reaction to produce biodiesel. Methyl palmitate (Sigma-Aldrich, 97.0%) and glycerol (Dinâmica Química Contemporânea, 99.5%) were used only in the liquid-liquid equilibrium study.
.

2.2 Biodiesel Synthesis
The biodiesel was produced by the methyl transesterification reaction of soybean oil, using potassium hydroxide as catalyst. The reaction was performed at 60 °C for 60 min, using a methanol to oil molar ratio of 10:1 and KOH concentration of 1 wt.%. The biodiesel was then separated from glycerol, added with hydrochloric acid to neutralize the catalyst and then washed with distilled water. Next, the biodiesel was distilled to remove any trace of methanol and unreacted oil residue (diglycerides and monoglycerides) [28]. Product composition and the amount of methyl ester were determined using a gas chromatograph (GC) (GCMS-QP2020 - Shimadzu) under the following conditions: SH-Rtx-5MS column (length, 30 m; diameter, 0.25 mm); injector temperature 230 °C; column temperature: 90-160 °C (10 °C.min-1), 160-180 °C (2 °C.min-1) and 180-230 °C (4 °C.min-1); carrier gas: 1.0 mL.min-1 of helium and thermogravimetric analysis (TGA) using a Shimadzu DTG-60 analyzer, with a heating rate of 10 °C/min, ambient

temperature up to 1000 °C and flow rate of 50 mL/min in a nitrogen atmosphere.

2.3 Isothermal Phase Diagrams
Ternary phase diagrams were constructed based on the mass titration method using visual observation via the cloud point, in line with the methodology developed by Evangelista Neto et al. [29]. The experimental points representing the miscibility curves were prepared using a base calculation of 10 g and placed in an equilibrium cell with magnetic agitation (Matoli, model 100M028). The operating temperature was controlled by circulating water in a thermostatized water bath (Solab, model SL-155), that is, 300.15 K for biodiesel and 308.15 K for methyl palmitate (MP), the latter selected based on the melting point of ester (303.15 K). The equilibrium lines were determined from the mass weight of the constituents, assuming a base calculation of 30 g, following a previously established ternary composition. Next, the samples were placed in an equilibrium cell under agitation for 3 h and then maintained at rest for 18 h for complete phase separation by decantation, similar to the study by Sena and Pereira [30]. Aliquots from each phase were collected to determine their mass fractions by measuring density in a digital densimeter (Anton Paar DMA 4500M). All measurements were performed in duplicate. Tie lines were used to determine the distribution (β) and selectivity (S) coefficients in order to quantify the extraction power of the solvent. The calcium of these parameters was determined by Equations (1), (2) and (3), where β_2 represents the distribution coefficient of methanol; β_3, the distribution coefficient of glycerol; S, the selectivity coefficient; w_{21}, the mass fraction of methanol in the biodiesel or MP-rich phase of glycerol; w_{23}, the mass fraction of methanol in the glycerol-rich phase; w_{33}, the mass fraction of glycerol in the glycerol-rich phase and w_{31}, the mass fraction of glycerol in the biodiesel or MP-rich phase.

$$\beta_2 = \frac{w_{21}}{w_{23}} \tag{1}$$

$$\beta_3 = \frac{w_{31}}{w_{33}} \tag{2}$$

$$S = \frac{\beta_2}{\beta_3} \tag{3}$$

2.4 Thermodynamic Models
The Othmer-Tobias [26] and Hand [27] correlations were applied to assess the thermodynamic consistency of the experimental LLE data observed by the tie lines. Model filling considered the mass fractions of the components in the glycerol and biodiesel or MP-rich phases, according to Equations (4) and (5), respectively, where w_{11} is the mass fraction of the biodiesel or MP in the biodiesel or MP-rich phase, a, the linear coefficient and b, the slope.

$$ln\left(\frac{1-w_{33}}{w_{33}}\right) = a + b\left(\frac{1-w_{11}}{w_{11}}\right) \tag{4}$$

$$ln\left(\frac{w_{23}}{w_{33}}\right) = a + b\left(\frac{w_{21}}{w_{11}}\right) \tag{5}$$

In addition, thermodynamic modeling is assessed by using excess Gibbs energy models, in order to establish the reliability of the experimental data. In this sense, Non-

Random Two Liquids (NRTL) and Universal Quasi-Chemical (UNIQUAC) thermodynamic models were assessed based on the behavior of the binary interaction parameters of the ternary systems (biodiesel + glycerol + methanol and methyl palmitate + glycerol + methanol)]. The regression parameters of the UNIQUAC and NRTL models were obtained by the objective function (OF) shown in Equation (6), where j, I, and k indicate the phase, component and tile line, respectively; M represents the number of tie lines; w^{exp}, experimental mass composition and w^{cal}, the mass composition. The binary interaction of parameters was determined using the TML computational tool [31].

$$OF = \sum_{k=1}^{M} \sum_{j=1}^{2} \sum_{i=1}^{3} \left[\left(w_{ijk}^{exp} - w_{ijk}^{cal} \right)^2 \right] \tag{6}$$

To evaluate the accuracy of the two models, the root-mean-square deviation (RMSD) was calculated by Equation (7), where k, j, i, w^{exp} and w^{cal} are the same as expressed in Equation (6).

$$RMSD(\%) = 100x \left[\sum_{k=1}^{M} \sum_{j=1}^{2} \sum_{i=1}^{3} \frac{\left(w_{ijk}^{exp} - w_{ijk}^{cal} \right)^2}{6M} \right]^{\frac{1}{2}} \tag{7}$$

The van der Waals molecular volume (r) and molecular surface area (q), parameters of the UNIQUAC model, were determined by the sum of the individual terms of each subgroup in the molecule of each component, as established by Equations (8) and (9) [32], where i is the system component; k, group identification; $v_k^{(i)}$, the number of k subgroups of component i; R_k, the value of the UNIFAC group volume parameter and Q_k, the value of the UNIFAC surface parameter. In the case of biodiesel, the parameters were determined using the weighted average that considered the composition of the principal esters.

$$r_i = \sum_k v_k^{(i)} R_k \tag{8}$$

$$q_i = \sum_k v_k^{(i)} Q_k \tag{9}$$

3. Results and Discussion
3.1 Biodiesel Synthesis

Figure 1 presents the TGA curve obtained from the biodiesel produced in the transesterification reaction. The biodiesel TGA curve showed only one mass loss event, reaching 98.8%, between 150 and 250 ºC, which corresponds to the volatilization and/or decomposition of fatty acid methyl ester, according to the results obtained by Andrade et al. [28]. Freire et al. [33] evaluated the thermal decomposition of biodiesel obtained between 243 and 266 ºC, which indicated the volatilization and/or combustion of the esters, mainly ethyl oleate and ethyl linoleate, and total mass decomposition above 266 °C.

Table 1 shows the composition of distilled biodiesel, according to GC-MS analysis. The main compounds in the biodiesel are methyl linoleate, methyl oleate and methyl palmitate, as observed by [34]. According to [35], the main fatty acids present in soybean oil are linoleic (52.83%), oleic

(25.85%), and palmitic (11.05%), and the biodiesel produced from soybean oil contains a larger amount of their esters.
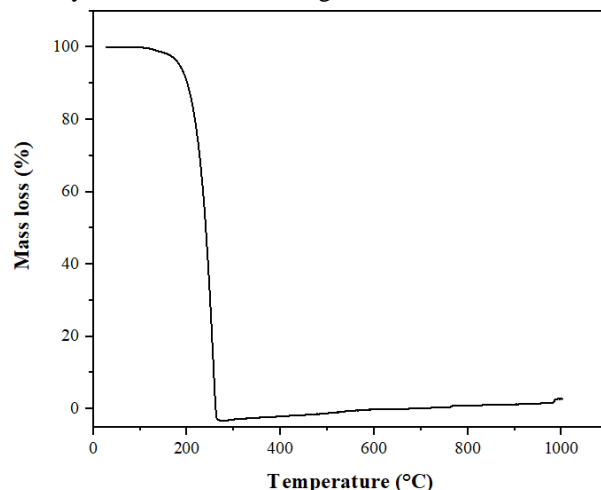

Figure 1. TGA curve of the distilled biodiesel.

Table 1. Biodiesel Composition.

Compound	Content %
Methyl caprate	2.93
Methyl laurate	4.74
Methyl palmitate	16.97
Methyl linoleate	42.69
Methyl oleate	27.36
Methyl stearate	5.02

3.2 Liquid-liquid Equilibrium
3.2.1 Ternary Diagrams

Knowledge of the biphasic region on a ternary diagram depends on the mutual solubility of the constituents present in the mixture, which must precede the implementation of the extraction or purification processes [18,36]. The miscibility curve (binodal) and tie line data of system 1 [biodiesel (1) + methanol (2) + glycerol (3)] and 2 [methyl palmitate (1) + methanol (2) + glycerol (3)] are presented in Tables 2 and 3 and plotted on the ternary diagrams of Figure 2.

Table 2. Experimental binodal curve data of the systems: [biodiesel (1) or MP (1)] + methanol (2) + glycerol (3).

Biodiesel (300.15 K)			Methyl Palmitate (308.15 K)		
w_1	w_2	w_3	w_1	w_2	w_3
0.07488	0.73697	0.18815	0.10046	0.71866	0.18087
0.03956	0.67011	0.29033	0.05238	0.66333	0.28429
0.02704	0.58028	0.39268	0.03195	0.57846	0.38958
0.01503	0.49122	0.49375	0.03169	0.48607	0.48224
0.01047	0.39438	0.59515	0.02506	0.38919	0.58574
0.00594	0.29722	0.69684	0.03541	0.28836	0.67623
0.00527	0.19831	0.79642	0.03543	0.19294	0.77163
0.00398	0.10069	0.89533	0.03995	0.09587	0.86418
0.18028	0.72000	0.09971	0.17475	0.69444	0.13081
0.28011	0.65186	0.06804	0.27364	0.63767	0.08870
0.38136	0.57215	0.04649	0.37461	0.56322	0.06216
0.48162	0.48210	0.03628	0.47958	0.48006	0.04036
0.58474	0.38936	0.02589	0.58063	0.38935	0.03002
0.69095	0.29595	0.01310	0.68456	0.29376	0.02168
0.79084	0.19822	0.01094	0.78582	0.19678	0.01740
0.88824	0.09974	0.01202	0.88237	0.09810	0.01954

Table 3. Phase equilibrium composition of the constituents.

Biodiesel-rich phase			Glycerol-rich phase		
w_1	w_2	w_3	w_1	w_2	w_3
Biodiesel (1) + methanol (2) + glycerol (3) at 300.15 K					
0.95030	0.03499	0.01471	0.00746	0.30918	0.68336
0.96835	0.01573	0.01592	0.00968	0.35745	0.63287
0.88841	0.09995	0.01163	0.02024	0.58708	0.39268
0.89162	0.09663	0.01175	0.05620	0.68287	0.26093
MP (1) + methanol (2) + glycerol (3) at 308.15 K					
0.89414	0.08829	0.01756	0.05783	0.65770	0.28446
0.90542	0.07465	0.01993	0.03473	0.57018	0.39509
0.92375	0.05071	0.02554	0.02026	0.34881	0.63094
0.93157	0.03941	0.02902	0.02977	0.22871	0.74152

The binodal curves (Figure 2) obtained with system 1 (containing biodiesel) and 2 (with MP) show similar behavior, consisting of an external biphasic zone due to the low miscibility of the constituents, indicating a large region favorable to the extraction process. This low miscibility is attributed to the fact that the polar molecules methanol and glycerol show no affinity for biodiesel because it is a mixture of nonpolar substances. This behavior was also observed in the *Sterculia striata* biodiesel + glycerol + ethanol [37] and soybean FAME + water + glycerol systems [17]. Analogously, the tie lines obtained here are similar in both systems, and their slopes demonstrate that methyl alcohol solubility in the biodiesel-rich (Figure 2a) and MP-rich phase (Figure 2b) is lower than in the glycerol-rich phase, indicating that a small amount of methanol and glycerol needs to be removed in the FAME-rich phase during biodiesel production via fatty acid esterification with methanol. The volume of the soluble component in the alcohol generally depends on its intermolecular strength [38]. With respect to the experimental points representing the two equilibrium phases of the tie lines, good agreement was observed with the respective binodal curves, ensuring the reliability of the equilibrium data obtained. These results corroborate the studies reported by Esipovich *et al.* [39], who assessed FAMEs + vegetable oil + methyl alcohol + FAMEs + glycerol + methyl alcohol ternary systems, and Asoodeh *et al.* [7] who evaluated linseed oil biodiesel + methanol + glycerol.
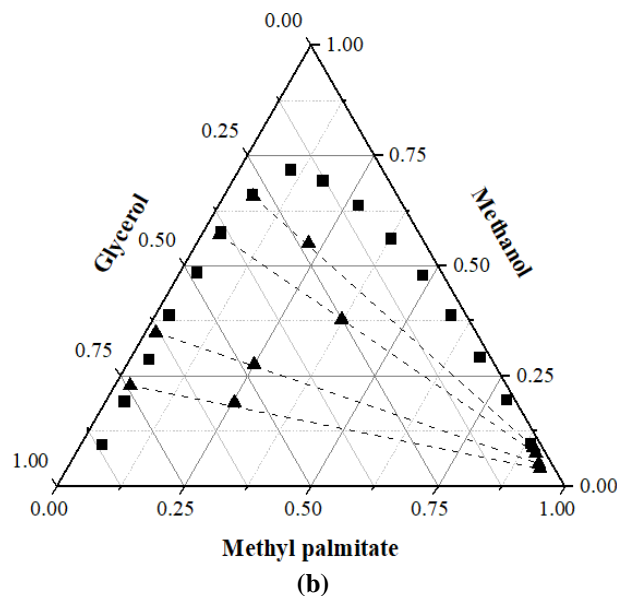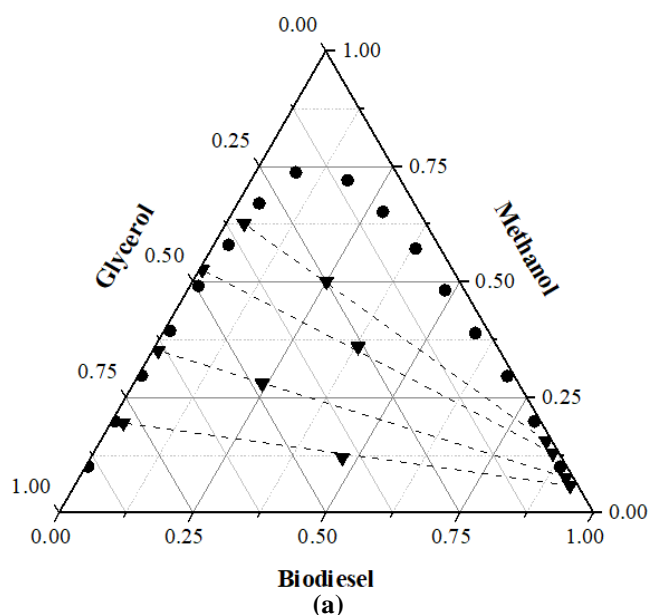
(b)

Figure 2. Ternary diagram for LLE of (a) system 1, with Biodiesel (1) + Methanol (2) + Glycerol (3) at 300.15 K (●) and (b) system 2, with Methyl palmitate (1) + Methanol (2) + Glycerol (3) at 308.15 K (■).

3.2.2 Distribution and Selectivity Coefficients

Liquid-liquid extraction, the selective transfer of a solute or impurity from a medium to a solvent, can be used in biodiesel purification to remove the glycerol obtained with the by-product in the transesterification reaction. The efficiency of biodiesel and MP extraction was assessed by the selectivity (*S*) and distribution coefficient (β). While selectivity indicates the capacity of the solvent to extract the solute without the need to extract other primary components from the solute, the distribution coefficient estimates the ability of the solvent to dissolve the solute, and can determine whether the number of extraction stages declines [40–42].

The distribution coefficients for systems 1 and 2, biodiesel and MP exhibited low values ($\beta_2 < 1$), indicating the preferential distribution of methanol in the glycerol-rich phase (Figure 3). The effect of the number of carbons in the FAME chain on the distribution coefficients of methanol remains unclear [43]. On the other hand, the distribution coefficients of methanol are smaller for MP than for biodiesel. A more marked decline was observed for system 1, given that it contains a mixture of methyl esters from longer and more saturated carbon chains than those of system 2. This behavior has a significant influence on the separation and purification stages involved in the optimization of methylic biodiesel, since higher distribution coefficients indicate a greater trend for biodiesel to absorb the solute (alcohol). Cavalcanti et al. [25] observed the same behavior in an LLE study for systems containing fatty acid, ethanol and glycerol ethyl esters. Analysis of the standard error of all experimental data showed that the value did not exceed 0.01, demonstrating dataset uniformity, indicating that the values obtained are concentrated around the mean.

Figure 4 shows that the selectivity values decline with an increase in the amount of methanol and are greater than one in all cases. This behavior demonstrates that most of the methanol is concentrated in the glycerol-rich phase, as confirmed by the tie lines in the LLE diagrams in Figure 2. However, selectivity values indicate a biodiesel-rich contamination phase and an increase in methyl ester

Biodiesel

(a)

concentration in the glycerol-rich phase due to excess methanol [44,45]. This means that the cost of biodiesel purification rises owing to the higher amount of excess methanol and its effect on glycerol and biodiesel or MP distribution between the two phases. The results corroborate those reported by Melo et al. [46], who reported that the selectivity coefficients obtained were higher than 1, indicating that methanol is an excellent solvent for glycerin extraction in the biodiesel-rich phase.
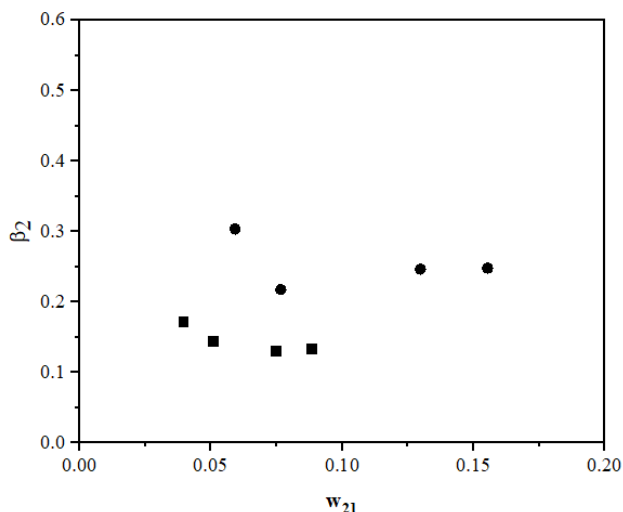

Figure 3. Experimental solute distribution coefficient (β_2) as a function of methanol mass fraction for system 1, with biodiesel (●) at 300.15 K, and system 2, with methyl palmitate (■) at 308.15 K.

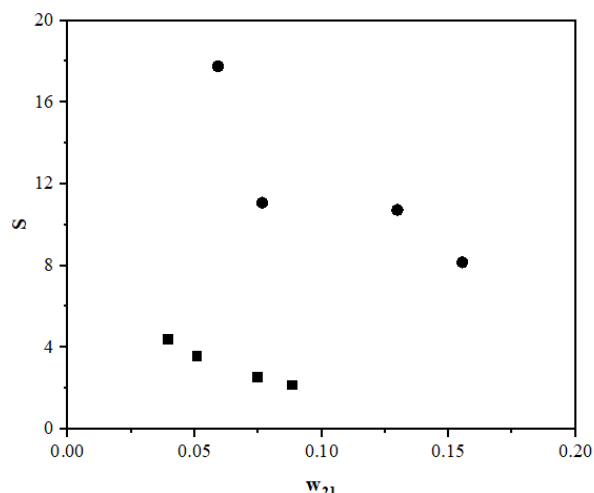*Figure 4. Experimental selectivity value (S) as a function of methanol mass fraction for system 1 (●) at 300.15 K, and system 2 (■) at 308.15 K.*

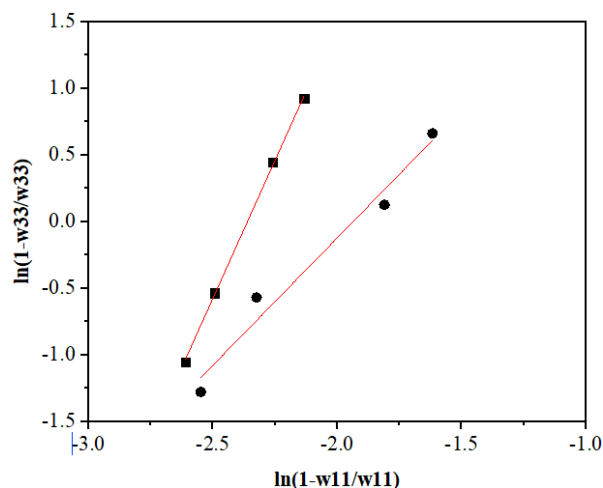### 3.3 Thermodynamic Models
3.3.1 Othmer-Tobias and Hand Correlations

The reliability of LLE experimental data, represented by the tie lines, was assessed by Othmer-Tobias and Hand correlations (Figure 5). These correlations can reproduce the tie lines using a straight line as a function of molar fractions [36,38]. Applying the Othmer-Tobias and Hand thermodynamic models to the experimental data obtained for the systems analyzed proved to be reliable and consistent, since they exhibited correlation coefficients above 0.97 (Table 4). Mousavi et al. [47] reported that the Othmer-Tobias and Hand correlations consistently represented the

experimental equilibrium data of the systems containing glycerol + methanol + organic solvents.

Table 4. Othmer-Tobias and Hand and linear coefficient (R^2) for the systems studied.

Correlation	a	b	R^2
Biodiesel (1) + Methanol (2) + Glycerol (3)			
Othmer-Tobias	1.91225	3.70232	0.97314
Hand	1.72081	3.46989	0.97169
Methyl palmitate (1) + Methanol (2) + Glycerol (3)			
Othmer-Tobias	4.14445	9.78547	0.99941
Hand	2.37475	6.3189	0.99955

(a) Othmer-Tobias correlation
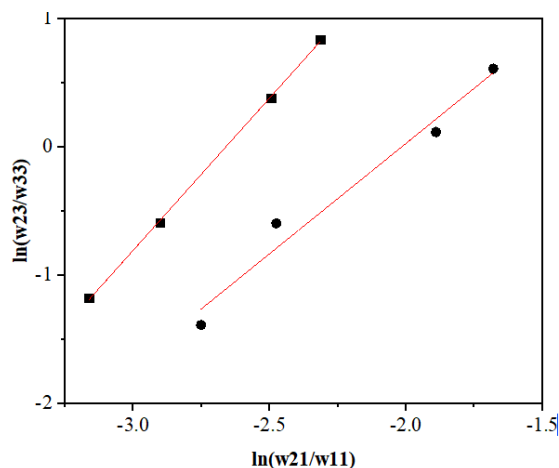
(b) Hand correlation

Figure 5. Thermodynamic consistency of the experimental data for system 1, with biodiesel (●) and system 2, with methyl palmitate (■).

3.3.2 NRTL and UNIQUAC Models

The structural q (van der Waals molecular surface area) and r parameters (van der Waals molecular volume) (Table 5) used for the UNIQUAC model were calculated from the contributions of the groups contained in the molecules of each component, in line with Prausnitz [32]. The binary interaction parameters of the UNIQUAC and NRTL models and parameter and non-randomness in a mixture (α_{ij}) were treated as adjustable parameters (Table 6). The root mean square deviation (RMSD) used to measure the accuracy of

the correlations was calculated from the difference between the experimental and calculated experimental mass (Table 6).

Table 5. The UNIQUAC structural parameters (r and q) for pure components.

Component	r	q
Biodiesel (Mix)	13.0726	10.7601
Methyl Oleate	13.3625	11.003
Methyl linoleate	13.1304	10.79
Methyl palmitate	12.2458	10.136
Methanol	1.4311	1.432
Glycerol	4.7957	4.908

Table 6. The binary parameters and the root mean square deviation (RMSD) of the Solvents (1) + Methanol (2) + Glycerol (3) ternary systems

Model	i-j	Aij	Aji	αij	RMSD (%)
Biodiesel (1) + Methanol (2) + Glycerol (3)					
UNIQUAC	1-2	2996.4	-311.8		
	1-3	-93.41	388.9		0.65952
	2-3	-85.932	654.33		
NRTL	1-2	2571.6	623.14	0.33632	
	1-3	824.9	946.37	0.20003	0.52932
	2-3	794.92	640.74	0.4472	
MP (1) + Methanol (2) + Glycerol (3)					
UNIQUAC	1-2	-1196.8	2532.8		
	1-3	-123.83	373.31		1.2319
	2-3	91.692	-148.54		
NRTL	1-2	747.88	-73.203	0.20206	
	1-3	781.03	920.07	0.27373	0.47579
	2-3	5736.7	995.66	0.26746	

Table 6 shows that both thermodynamic models correlated accurately with the experimental data for system 1, obtaining RMSD values below 0.66%. The NRTL model correlated the experimental data of system 2 more accurately than its UNIQUAC counterpart, obtaining an average RMSD of approximately 0.48% (NRTL) compared to 1.23% (UNIQUAC), similar to the studies conducted by [16,48]. The results presented in Table 6 can be visualized in Figures 6 (a) and (b), which show the fitting of the two models to the experimental data. In both systems (with biodiesel and MP), the NRTL model obtained smaller deviations, akin to the results presented by Rocha et al. [49], who obtained a good fit of this model to the experimental data of ternary systems with ethylic biodiesel from palm oil, obtaining an RMSD of 0.180% at 298.15 K for NRTL model. Do Carmo et al. [50] assessed four different thermodynamic models of activity coefficients that can be used for biodiesel in 34 different systems. The best results for NRTL and UNIQUAC models exhibited an RMSD of 9.1 and 8.2%, respectively, obtaining higher deviations than those presented here
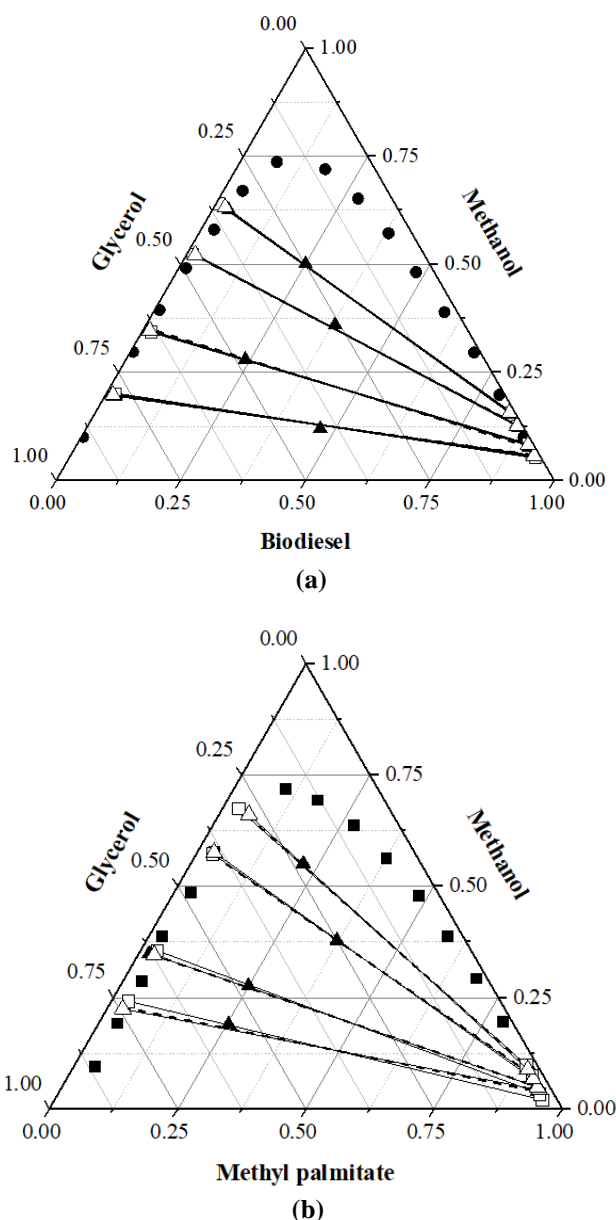

Figure 6. Ternary phase diagram for LLE of a) Biodiesel (1) + Methanol (2) + Glycerol (3) at 300.15 K (system 1) (●) and (b) Methyl palmitate (1) + Methanol (2) + Glycerol (3) at 308.15 K (system 2) (■). Experimental tie-line points (▲), NRTL model (Δ) and UNIQUAC model (□).

The UNIQUAC tie line parameters of system 1 were assessed in order to determine the best fit when applying the model and justify the difference in residual error. Figure 7 shows that any of the components can be selected to calculate the parameters and apply the model to the biodiesel. The components with the highest concentrations in biodiesel and a weighted average of the mixture were considered. All of these exhibited good fit to the experimental data. Lee et al. [51] found that methyl esters, methyl linoleate and methyl oleate in the presence of glycerol and methanol showed optimal results in terms of the experimental data fit to the UNIQUAC model. Mohadesi [52] reported that the UNIQUAC model is highly accurate considering the biodiesel (methyl ester), glycerol and methanol ternary system. Both studies demonstrate that the contributions of the subgroups contained in the molecules do not interfere in correlating the UNIQUAC model to the experimental data. Thus, the UNIQUAC model with optimized parameters

provides a reliable base to simulate separation of the FAME and glycerol-rich phases in biodiesel production processes.
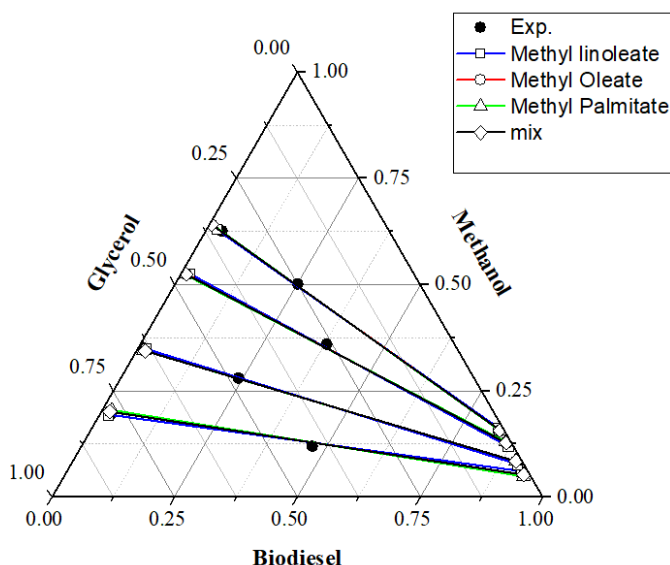

Figure 7. Experimental tie-line points for system 1: Biodiesel (1) + Methanol (2) + Glycerol (3) at 300.15 K and FAME parameters for the UNIQUAC model.

4. Conclusion

In the study of LLE, the solubility curves for system 1 (biodiesel + methanol + glycerol at 300.15K) and 2 (methyl palmitate + methanol + glycerol at 308.15 K) showed a curve with a large region of two phases. The tie lines constructed exhibited a marked decline, indicating good separation between biodiesel and the other components of system 1. Methanol content was higher in the glycerol-rich phase, resulting in important savings in the biodiesel purification stage. The study of equilibrium data consistency conducted using the Othmer-Tobias and Hand correlations show model fit, with R^2 values above 0.97. The Hand correlation exhibited better fit for both systems, confirming the good thermodynamic consistency of the experimental data. The UNIQUAC and NRTL thermodynamic models provided a good representation of experimental data, displaying an average square deviation of 0.66 and 0.53%, respectively for system 1. For system 2, the deviations were 1.23 and 0.48%, indicating better fit of the NRTL thermodynamic model. Assessment of UNIQUAC parameters, considering individual principal esters present in the biodiesel and a mixture of the respective esters, was conducted, showing that any of the components can be selected to calculate the parameters and apply the model to the biodiesel. The experimental data measured and presented in this study on pure biodiesel components and biodiesel system may be useful in building a database for researchers involved in biodiesel process development and optimization. The increasing diversification of the world energy matrix aims to combine energy security and sustainable development. For future research, the goal is to completely replace fossil fuel (diesel) with biodiesel and evaluate the effect of fuel on compression ignition engines in order to reduce carbon dioxide emissions and global warming.

Nomenclature

Symbol	Variable
β	distribution coefficient
S	selectivity coefficient
w^{exp}	experimental mass composition
w^{cal}	mass composition
r	van der Waals molecular volume
q	molecular surface area
v_k,	the number of k subgroups
R_k,	UNIFAC group volume parameter
Q_k,	UNIFAC surface parameter.

Subscripts

1	Biodiesel or MP
2	Methanol
3	Glycerol
j	phase
i	component
k	tie lines
M	number of tie lines

Abbrevations

LLE	Liquid-Liquid Equilibrium
MP	Methyl palmitate
GC	Gas Chromatography
OF	Objective Function
TGA	Thermogravimetric analysis
RMSD	Root-mean-square deviation
R^2	Regression coefficient

References

[1] T. Güney, "Renewable energy, non-renewable energy and sustainable development," *Int. J. Sustain. Dev. World Ecol.,* 26, 389–397, 2019, https://doi.org/10.1080/13504509.2019.1595214.

[2] P. Mukhopadhyay, R. Chakraborty, "LCA of sustainable biodiesel production from fried Borassus flabellifer oil in energy-proficient reactors: Impact assessment of multi fuel-additives on pour point, NOx and engine performance," *Sustain. Energy Technol. Assessments.,* 44, 100994, 2021, https://doi.org/10.1016/j.seta.2021.100994.

[3] J.A. Okolie, A. Mukherjee, S. Nanda, A.K. Dalai, J.A. Kozinski, "Next-generation biofuels and platform biochemicals from lignocellulosic biomass," *Int. J. Energy Res.,* 45, 14145–14169, 2021, https://doi.org/10.1002/er.6697.

[4] M. Viccaro, D. Caniani, S. Masi, S. Romano, M. Cozzi, "Biofuels or not biofuels? The "Nexus Thinking" in land suitability analysis for energy crops," *Renew. Energy.,* 187, 1050–1064, 2022, https://doi.org/10.1016/j.renene.2022.02.008.

[5] F. Fangfang, A. Alagumalai, O. Mahian, "Sustainable biodiesel production from waste cooking oil: ANN modeling and environmental factor assessment," *Sustain. Energy Technol. Assessments.,* 46, 101265, 2021, https://doi.org/10.1016/j.seta.2021.101265.

[6] M.M. Hasan, M.M. Rahman, "Performance and emission characteristics of biodiesel–diesel blend and environmental and economic impacts of biodiesel production: A review," *Renew. Sustain. Energy Rev.,* 74, 938–948, 2017,

https://doi.org/10.1016/j.rser.2017.03.045.

[7] A. Asoodeh, F. Eslami, S.M. Sadrameli, "Liquid–liquid equilibria of systems containing linseed oil biodiesel + methanol + glycerol: Experimental data and thermodynamic modeling," *Fuel.*, 253, 460–473, 2019, https://doi.org/10.1016/j.fuel.2019.04.170.

[8] M. Hashemzadeh Gargari, S.M. Sadrameli, "Investigating continuous biodiesel production from linseed oil in the presence of a Co-solvent and a heterogeneous based catalyst in a packed bed reactor," *Energy.*, 148, 888–895, 2018, https://doi.org/10.1016/j.energy.2018.01.105.

[9] J.C. Ge, S.K. Yoon, "Combustion and Emission Characteristics of a Diesel Engine Fueled with Crude Palm Oil Blends at Various Idling Speeds," *Applied Sciences*, 12(13), 6294, 2022.

[10] S.M. Rasulov, I.M. Abdulagatov, "PVT, saturated liquid density and vapor-pressure measurements of main components of the biofuels at high temperatures and high pressures: Methyl palmitate," *Fuel.*, 218, 282–294, 2018, https://doi.org/10.1016/j.fuel.2018.01.039.

[11] F. Yang, M.A. Hanna, R. Sun, "Value-added uses for crude glycerol - A byproduct of biodiesel production," *Biotechnol. Biofuels.*, 5, 1–10, 2012, https://doi.org/10.1186/1754-6834-5-1322413907.

[12] T. Zhang, C. Liu, Y. Gu, F. Jérôme, "Glycerol in energy transportation: A state-of-the-art review," *Green Chem.*, 23, 7865–7889, 2021, https://doi.org/10.1039/d1gc02597j.

[13] Y. Wang, Y. Muhammad, S. Yu, T. Fu, K. Liu, Z. Tong, X. Hu, H. Zhang, "Preparation of Ca-and Na-Modified Activated Clay as a Promising Heterogeneous Catalyst for Biodiesel Production via Transesterification," *Appl. Sci.*, 12, 2022, https://doi.org/10.3390/app12094667.

[14] C.S. Osorio-González, N. Gómez-Falcon, F. Sandoval-Salas, R. Saini, S.K. Brar, A.A. Ramírez, "Production of biodiesel from castor oil: A review," *Energies.*, 13, 1–22, 2020, https://doi.org/10.3390/en13102467.

[15] D.S. Negi, F. Sobotka, T. Kimmel, R. Schoma, "Liquid - Liquid Phase Equilibrium in Glycerol - Methanol - Methyl Oleate and Glycerol - Monoolein - Methyl Oleate Ternary Systems," *Ind. Eng. Chem. Res.*, 3693–3696, 2006.

[16] I.E.P. Toledo, L. Ferreira-Pinto, F.A.P. Voll, L. Cardozo-Filho, L. Meili, D.D.G. Coêlho, S.H.V. De Carvalho, J.I. Soletti, "Liquid-Liquid Equilibrium of the System {Peanut Biodiesel + Glycerol + Ethanol} at Atmospheric Pressure," *J. Chem. Eng. Data.*, 64, 2207–2212, 2019, https://doi.org/10.1021/acs.jced.8b01185.

[17] J.R.F. Silva, M.A. Mazutti, F.A.P. Voll, L. Cardozo-Filho, M.L. Corazza, M. Lanza, W.L. Priamo, J. Vladimir Oliveira, "Thermophysical properties of biodiesel and related systems: (Liquid + liquid) equilibrium data for Jatropha curcas biodiesel," *J. Chem. Thermodyn.*, 58, 467–475, 2013, https://doi.org/10.1016/j.jct.2012.10.006.

[18] T. Wannachod, M. Hronec, T. Soták, K. Fulajtárová, U. Pancharoen, A. Arpornwichanop, "Effects of salt on the LLE and tie-line data for furfuryl alcohol - N-butanol-water at T = 298.15 K," *J. Mol. Liq.*, 218, 50–58, 2016, https://doi.org/10.1016/j.molliq.2016.02.027.

[19] M. Maghami, J. Yousefi Seyf, S.M. Sadrameli, A. Haghtalab, "Liquid-liquid phase equilibrium in ternary mixture of waste fish oil biodiesel-methanol-glycerol: Experimental data and thermodynamic modeling," *Fluid Phase Equilib.*, 409, 124–130, 2016, https://doi.org/10.1016/j.fluid.2015.09.046.

[20] J.C. Nunes, J.J.P. Nascimento, A.S. Peiter, L. Ferreira-Pinto, J.I. Soletti, S.H.V. De Carvalho, J.J.N. Alves, A.C.B. De Araujo, "Experimental Data and Phase Equilibrium Modeling in Ternary and Pseudoquaternary Systems of Sunflower Oil for Biodiesel Production," *J. Chem. Eng. Data.*, 64, 412–420, 2019, https://doi.org/10.1021/acs.jced.8b00276.

[21] B. Bazooyar, F. Shaahmadi, M.A. Anbaz, A. Jomekian, "Intelligent modelling and analysis of biodiesel/alcohol/glycerol liquid-liquid equilibria," *J. Mol. Liq.*, 322, 114972, 2021, https://doi.org/10.1016/j.molliq.2020.114972.

[22] M.A. Noriega, P.C. Narváez, "UNIFAC correlated parameters for liquid-liquid equilibrium prediction of ternary systems related to biodiesel production process," *Fuel.*, 249, 365–378, 2019, https://doi.org/10.1016/j.fuel.2019.03.124.

[23] L.A. Follegatti-Romero, M.B. Oliveira, F.R.M. Batista, E.A.C. Batista, J.A.P. Coutinho, A.J.A. Meirelles, "Liquid-liquid equilibria for ternary systems containing ethyl esters, ethanol and glycerol at 323.15 and 353.15 K," *Fuel.*, 94, 386–394, 2012, https://doi.org/10.1016/j.fuel.2011.09.020.

[24] M. Toikka, P. Kuzmenko, A. Samarov, M. Trofimova, "Phase behavior of the oleic acid – methanol – methyl oleate – water mixture as a promising model system for biodiesel production: Brief data review and new results at 303.15 K and atmospheric pressure," *Fuel.*, 319, 2022, https://doi.org/10.1016/j.fuel.2022.123730.

[25] R.N. Cavalcanti, M.B. Oliveira, A.J.A. Meirelles, "Liquid-liquid equilibria for systems containing fatty acid ethyl esters, ethanol and glycerol at 333.15 and 343.15 K: Experimental data, thermodynamic and artificial neural network modeling," *Brazilian J. Chem. Eng.*, 35, 819–834, 2018, https://doi.org/10.1590/0104-6632.20180352s20160267.

[26] D.F. Othmer, E. Tobias, "Tie Line Correlation," *Industrial and Engineering Chemistry,* 34, 6, 1942, https://doi.org/https://doi-org.ez18.periodicos.capes.gov.br/10.1021/ie50390a600.

[27] D.B. Hand, *Dineric distribution*, 1930, https://doi.org/https://doi.org/10.1021/j150315a009.

[28] M.R. de Almeida Andrade, C.B. Silva, T.K.O. Costa, E.L. de Barros Neto, J.M. Lavoie, "An experimental investigation on the effect of surfactant for the transesterification of soybean oil over eggshell-derived CaO catalysts", *Energy Convers. Manag. X.*, 11, 2021, https://doi.org/10.1016/j.ecmx.2021.100094.

[29] A.A. Evangelista Neto, J.C.C. Sobrinho, H.N.M. Oliveira, H.F.S. Freitas, F.F.M. Silva, E.L. Barros Neto, "Liquid-Liquid Equilibrium Data for the Pseudo-Ternary Biodiesel of Chicken Fat + Methanol + Glycerol," *Brazilian J. Pet. Gas.*, 12, 123–133, 2018, https://doi.org/10.5419/bjpg2018-0012.

[30] C.. Sena, S.R.C; Pereira, "Melon Seed Oil Utilization for Biodiesel Production and Analysis of Liquid-Liquid Equilibrium for the System Biodiesel+Methanol+Glycerin," *Environ. Prog. Sustain. Energy.*, 33, 676–680, 2014, https://doi.org/10.1002/ep.

[31] L. Stragevitch, *Equilíbrio Líquido-Líquido de Misturas de Não Eletrólitos*, 1997.

[32] B.E. Reid, Robert C.; Prausnitz, John M.; Poling, *The Properties of Gases and Liquids*, 4th ed., New York, 1987.

[33] L.M.S. Freire, T.C. Bicudo, R. Rosenhaim, F.S.M. Sinfrônio, J.R. Botelho, J.R. Carvalho Filho, I.M.G. Santos, V.J. Fernandes, N.R. Antoniosi Filho, A.G. Souza, "Thermal investigation of oil and biodiesel from jatropha curcas L.," *J. Therm. Anal. Calorim.*, 96, 1029–1033, 2009, https://doi.org/10.1007/s10973-009-0055-y.

[34] V. Kumbhar, A. Pandey, C.R. Sonawane, A.S. El-Shafay, H. Panchal, A.J. Chamkha, "Statistical analysis on prediction of biodiesel properties from its fatty acid composition," *Case Stud. Therm. Eng.*, 30, 2022, https://doi.org/10.1016/j.csite.2022.101775.

[35] A. Alcántara-Carmona, F.J. López-Giménez, M.P. Dorado, "Compatibility studies between an indirect injection diesel injector and biodiesel with different composition: Stationary tests," *Fuel.*, 307, 2022, https://doi.org/10.1016/j.fuel.2021.121788.

[36] A. Ghanadzadeh Gilani, A. Najafgholizadeh, B. Mohammadi khanghah, M. Nasouri Gazani, "Experimental and correlational study of phase equilibria in aqueous solutions of phosphoric acid with alcohols at different temperatures," *J. Mol. Liq.,* 268, 553–560, 2018, https://doi.org/10.1016/j.molliq.2018.06.115.

[37] J.C.G. Filho, F.B. Bispo, M.L. Corazza, P.F. Arce, F.A.P. Voll, D. De Gusmão Coêlho, L. Ferreira-Pinto, S.H.V. De Carvalho, J.I. Soletti, "Liquid-Liquid Equilibrium Measurement and Thermodynamic Modeling of the { Sterculia striata Biodiesel + Glycerol + Ethanol} System," *J. Chem. Eng. Data.*, 66, 3293–3299, 2021, https://doi.org/10.1021/acs.jced.1c00341.

[38] Y. Jiang, S. Lin, H. Yan, H. Guo, Q. Li, "Liquid-liquid equilibrium data measurement and thermodynamic modelling for ternary mixtures composed of water, diethylene glycol dimethyl ether and different solvents at 298.2 K," *J. Chem. Thermodyn.*, 165, 0–7, 2020, https://doi.org/10.1016/j.jct.2021.106669.

[39] A.L. Esipovich, A.E. Rogozhin, A.S. Belousov, E.A. Kanakov, K. V. Otopkova, S.M. Danov, "Liquid–liquid equilibrium in the systems FAMEs + vegetable oil + methyl alcohol and FAMEs + glycerol + methyl alcohol," *Fuel.,* 217, 31–37, 2018, https://doi.org/10.1016/j.fuel.2017.12.083.

[40] A. Ghanadzadeh Gilani, J. Jahanbin sardroodi, F. Verpoort, S. Rahmdel, "Experimental study and thermodynamic modeling of phase equilibria of systems containing cyclohexane, alcohols (C4 and C5), and deep eutectic solvents," *J. Mol. Liq.*, 340, 2021, https://doi.org/10.1016/j.molliq.2021.117196.

[41] X. Meng, X. Liu, J. Gao, D. Xu, L. Zhang, Y. Wang, "Liquid-Liquid Equilibrium of Isobutyl Acetate + Isobutyl Alcohol + Imidazolium-Based Ionic Liquids at 298.15 and 308.15 K," *J. Chem. Eng. Data.* 64, 778–783, 2019, https://doi.org/10.1021/acs.jced.8b01045.

[42] M.P. Cumplido, A. Cháfer, J.I. Guayazan-Jaimes, J. de la Torre, J.D. Badia, "Potential of phosphonium-based ionic liquids to purify 1-propanol from water by liquid–liquid extraction at mild conditions," *J. Chem. Thermodyn.*, 165, 2022, https://doi.org/10.1016/j.jct.2021.106588.

[43] S. Shiozawa, D. Gonçalves, M.C. Ferreira, A.J.A. Meirelles, E.A.C. Batista, "Liquid-liquid equilibrium data and thermodynamic modeling of systems involved in the biodiesel production in terms of acylglycerols, free fatty acids, ethyl esters, and ethanol at 303.2 and 318.2 K and local pressure," *Fluid Phase Equilib.,* 507 112431, 2020, https://doi.org/10.1016/j.fluid.2019.112431.

[44] H. Liu, B. Jia, W. Sun, S. Dong, "Measurement and Thermodynamic Modeling of Ternary (Liquid + Liquid) Equilibrium for Extraction of 2-Methyl-3-buten-2-ol from Aqueous Solution with Different Solvents," *J. Chem. Eng. Data.*, 65, 5030–5036, 2020, https://doi.org/10.1021/acs.jced.0c00667.

[45] H. Shekaari, M.T. Zafarani-Moattar, B. Mohammadi, "Effective extraction of benzene and thiophene by novel deep eutectic solvents from hexane / aromatic mixture at different temperatures," *Fluid Phase Equilib.*, 484, 38–52, 2019, https://doi.org/10.1016/j.fluid.2018.11.025.

[46] K.R.B. De Melo, G.C. Lopes, D.D.G. Coêlho, J.I. Soletti, "Liquid-liquid equilibrium for systems composed by biodiesel from catolé oil (Syagrus cearensis), methanol and glycerol," *Chem. Ind. Chem. Eng. Q.,* 26, 21–29, 2020, https://doi.org/10.2298/CICEQ190508021B.

[47] H.S. Mousavi, M. Rahimi, M. Mohadesi, "Experimental Investigation and Thermodynamic Modeling of Glycerin/Methanol/Organic Solvent Systems," *Chem. Eng. Technol.,* 42, 628–636, 2019, https://doi.org/10.1002/ceat.201800356.

[48] L.R. Kanda, F.A.P. Voll, M.L. Corazza, "LLE for the systems ethyl palmitate (palmitic acid)(1)+ethanol(2)+glycerol (water)(3)," Fluid Phase Equilib. 354, 147–155, 2013, https://doi.org/10.1016/j.fluid.2013.06.027.

[49] E.G.D.A. Rocha, L.A. Follegatti-Romero, S. Duvoisin, M. Aznar, "Liquid-liquid equilibria for ternary systems containing ethylic palm oil biodiesel + ethanol + glycerol/water: Experimental data at 298.15 and 323.15 K and thermodynamic modeling," *Fuel.*, 128, 356–365, 2014,

https://doi.org/10.1016/j.fuel.2014.01.074.

[50] F.R. Do Carmo, N.S. Evangelista, R.S. De Santiago-Aguiar, F.A.N. Fernandes, H.B. De Sant'Ana, "Evaluation of optimal activity coefficient models for modeling and simulation of liquid-liquid equilibrium of biodiesel + glycerol + alcohol systems," *Fuel.* 125, 57–65, 2014, https://doi.org/10.1016/j.fuel.2014.01.108.

[51] M.J. Lee, Y.C. Lo, H.M. Lin, "Liquid-liquid equilibria for mixtures containing water, methanol, fatty acid methyl esters, and glycerol," *Fluid Phase Equilib.,* 20.299983.1309.

299 180–190, 2010, https://doi.org/10.1016/j.fluid.2010.10.010.

[52] M. Mohadesi, "Liquid-Liquid Equilibrium for Ternary Systems Containing Biodiesel + Glycerol + Alcohol (Ethanol or Methanol): Thermodynamic Modeling," *Journal of Chemical and Petroleum Engineering*, 54, 285–295, 2020, https://doi.org/10.22059/jchpe.20